REPORT DOCUMENTATION PAGE

1. AGENCY USE ONLY (Leave blank)	2. REPORT DATE January 4, 1996	3. REPORT TYPE AND DATES COVERED Final Report 5/1/93-12/31/95	

4. TITLE AND SUBTITLE
Performance Improvements in Plasma Thrusters (w)

5. FUNDING NUMBERS
FQ 8671-9300908
G-AFOSR-91-0256

6. AUTHOR(S)
Manuel Martinez-Sanchez, PI

7. PERFORMING ORGANIZATION NAME(S) AND ADDRESS(ES)
Space Systems Laboratory
MIT, Dept. of Aero/Astro
77 Massachusetts Avenue
Cambridge, MA 02139

AFOSR-TR-96
0082

9. SPONSORING/MONITORING AGENCY NAME(S) AND ADDRESS(ES)
Mitat Birkan
AFOSR/NA
110 Duncan Ave, Suite B115
Bolling AFB, D.C. 20332-0001

10. SPONSORING/MONITORING AGENCY REPORT NUMBER

11. SUPPLEMENTARY NOTES

12a. DISTRIBUTION/AVAILABILITY STATEMENT
Approved for public release; distribution is unlimited.

12b. DISTRIBUTION CODE

13. ABSTRACT (Maximum 200 words)

This Report documents our research in two areas of Electric Propulsion:
(a) A preliminary study of the performance of cesium-seeded hydrogen arcjets, which showed a feasible design range in which frozen losses can be nearly eliminated, and (b) A particle simulation numerical model of Hall thrusters, which can give both, fairly accurate overall performance predictions, and also detailed information about internal parameter distributions.

19960320 056

14. SUBJECT TERMS
Electric Propulsion, Arcjets, Hall Thrusters

15. NUMBER OF PAGES
87

16. PRICE CODE

17. SECURITY CLASSIFICATION OF REPORT	18. SECURITY CLASSIFICATION OF THIS PAGE	19. SECURITY CLASSIFICATION OF ABSTRACT	20. LIMITATION OF ABSTRACT
Unclassified	Unclassified	Unclassified	UL

GENERAL INSTRUCTIONS FOR COMPLETING SF 298

The Report Documentation Page (RDP) is used in announcing and cataloging reports. It is important that this information be consistent with the rest of the report, particularly the cover and title page. Instructions for filling in each block of the form follow. It is important to *stay within the lines* to meet *optical scanning requirements*.

Block 1. Agency Use Only *(Leave blank)*.

Block 2. Report Date. Full publication date including day, month, and year, if available (e.g. 1 Jan 88). Must cite at least the year.

Block 3. Type of Report and Dates Covered. State whether report is interim, final, etc. If applicable, enter inclusive report dates (e.g. 10 Jun 87 - 30 Jun 88).

Block 4. Title and Subtitle. A title is taken from the part of the report that provides the most meaningful and complete information. When a report is prepared in more than one volume, repeat the primary title, add volume number, and include subtitle for the specific volume. On classified documents enter the title classification in parentheses.

Block 5. Funding Numbers. To include contract and grant numbers; may include program element number(s), project number(s), task number(s), and work unit number(s). Use the following labels:

C	- Contract	PR	- Project
G	- Grant	TA	- Task
PE	- Program Element	WU	- Work Unit Accession No.

Block 6. Author(s). Name(s) of person(s) responsible for writing the report, performing the research, or credited with the content of the report. If editor or compiler, this should follow the name(s).

Block 7. Performing Organization Name(s) and Address(es). Self-explanatory.

Block 8. Performing Organization Report Number. Enter the unique alphanumeric report number(s) assigned by the organization performing the report.

Block 9. Sponsoring/Monitoring Agency Name(s) and Address(es). Self-explanatory.

Block 10. Sponsoring/Monitoring Agency Report Number. *(If known)*

Block 11. Supplementary Notes. Enter information not included elsewhere such as: Prepared in cooperation with...; Trans. of...; To be published in.... When a report is revised, include a statement whether the new report supersedes or supplements the older report.

Block 12a. Distribution/Availability Statement. Denotes public availability or limitations. Cite any availability to the public. Enter additional limitations or special markings in all capitals (e.g. NOFORN, REL, ITAR).

DOD - See DoDD 5230.24, "Distribution Statements on Technical Documents."
DOE - See authorities.
NASA - See Handbook NHB 2200.2.
NTIS - Leave blank.

Block 12b. Distribution Code.

DOD - Leave blank.
DOE - Enter DOE distribution categories from the Standard Distribution for Unclassified Scientific and Technical Reports.
NASA - Leave blank.
NTIS - Leave blank.

Block 13. Abstract. Include a brief *(Maximum 200 words)* factual summary of the most significant information contained in the report.

**Block 14.** Subject Terms. Keywords or phrases identifying major subjects in the report.

Block 15. Number of Pages. Enter the total number of pages.

Block 16. Price Code. Enter appropriate price code *(NTIS only)*.

Blocks 17. - 19. Security Classifications. Self-explanatory. Enter U.S. Security Classification in accordance with U.S. Security Regulations (i.e., UNCLASSIFIED). If form contains classified information, stamp classification on the top and bottom of the page.

Block 20. Limitation of Abstract. This block must be completed to assign a limitation to the abstract. Enter either UL (unlimited) or SAR (same as report). An entry in this block is necessary if the abstract is to be limited. If blank, the abstract is assumed to be unlimited.

DISCLAIMER NOTICE

UNCLASSIFIED

Technical Report
distributed by

**DEFENSE
TECHNICAL
INFORMATION
CENTER**

DTIC| Acquiring Information-
Imparting Knowledge

Cameron Station
Alexandria, Virginia 22304-6145

UNCLASSIFIED

THIS DOCUMENT IS BEST QUALITY AVAILABLE. THE COPY FURNISHED TO DTIC CONTAINED A SIGNIFICANT NUMBER OF PAGES WHICH DO NOT REPRODUCE LEGIBLY.

PERFORMANCE IMPROVEMENTS IN PLASMA THRUSTERS

Final Technical Report on Grant 91-0256

Covering the Period: 5/1/93-12/31/95

by

Manuel Martinez-Sanchez
Professor of Aeronautics/Astronautics
MIT, 37-401
77 Massachusetts Ave
Cambridge, MA 02139-4307

Attn: Mitat Birkan AFOSR/NA
110 Duncan Ave,
Suite B115
Bolling AFB
Washington, D.C. 20332-0001

Jan. 2, 1996

Introduction

This Report covers the results of modeling work performed at the MIT Space Power and Propulsion Laboratory for the past 2 1/2 years on two Electric Propulsion technologies: Arcjets and Hall Thrusters.

The Proposal for this Grant listed two Tasks:
1. Seeding and Multi-Species Effects in Arcjets
2. Development of Two-Dimensional Models of Hall Thrusters

This was supplemented for an 8-month extension with proposed work on Arcjet Anode Attachment and on Cross-Field Transport in Hall Thrusters.

The work on Task 1 (Seeding and Multispecies Effects) was further subdivided into studies of H_2 segregation in N_2-H_2 arcjets and feasibility studies of Cesium-seeded hydrogen arcjets. It was acknowledged that the scope of proposed work exceeded resources, but it was hoped that additional student support could be obtained through AASERT program. In the event, we were unable to secure this support, and the subtask on H_2 segregation has not been performed.

We have, on the other hand, performed significant work on Cesium-seeded arcjets and on Hall Thruster two-dimensional modeling. This work will be briefly described here, and further documented by enclosed Conference papers. The work on the Extension areas is still incomplete, and will be separately reported at the end of a planned no-cost extension.

2. Alkali-Seeded Hydrogen Arcjets

The motivation for this work is the existence of large "frozen losses" in conventional arcjets using molecular gases. These losses appear to be unavoidable: ionization of the gas is needed for conduction, and is fairly costly in terms of energy (≈ 15 eV per ion for usual fuels); also, at the temperatures where ionization occurs, molecular dissociation is complete, further adding a few eV per eventual ion. Because of the very short expansion time and the moderate pressures in use, nozzle recombination is very limited, and most of this energy is lost in the exhaust.

Seeding the working gas with small amounts of an alkali (Cs or K) has been standard practice in MHD power generation, where gas temperatures are limited below ionizing

levels by either fuel energy (combustion MHD) or wall endurance (non-equilibrium MHD). Cesium, in particular, has an ionization potential of only 3.9 volts, and is fully ionized at electron temperatures as low as 4000K. This could be directly of use under equilibrium conditions, keeping the molecular working gas neutral; however, significant dissociation could still be incurred at this temperature. A second physical effect can be exploited at this point: since the Cs fraction will be kept as low as possible to avoid overly increasing the gas molecular weight, we can expect a relatively low conductivity level, and hence, for a given volumetric heating rate, high E fields. The electron temperature is known to increase with E/P (p=gas pressure), and hence we can expect thermal non-equilibrium to develop, with Te significantly exceeding the gas temperature Tg. Since ionization depends on Te, while dissociation is mainly a function of Tg, we can strive for conditions where Tg is no higher than perhaps 3000K (sufficient for Isp to exceed 900 sec in hydrogen), and dissociation can be kept to a minimum. At the same time, Te could be high enough to fully ionize the Cs seed, although still below some level of the order of 7000K which would be required to ionize the working gas.

A secondary benefit of the increased electric field level is higher voltage operation. Within limits (say below the KV level) this is beneficial in that it minimizes the fractional loss due to near-electrode voltage drops. These drops are themselves likely to be reduced by the presence of the alkali, perhaps in proportion to the ionization potential.

One final effect which could contribute to higher efficiency is the more uniform radial distribution of heating in a seeded gas. The strong constriction of the discharge into an arc is due to the steep increase in conductivity associated with partial ionization on the arc edges; in a situation where the Cesium can be fully ionized everywhere, constriction is less likely. This has two consequences: (a) It reduces the possibility of highly localized regions where hydrogen could become itself ionized, and (b) It directly improves the efficiency, because in any propulsive device heat is most efficiently used to produce momentum flux if distributed uniformly across the gas stream.

All of these potential benefits must be eventually weighed against (a) Operational complexity in the dispensing of Cs, which must be kept liquid and its vapor must homogeneously mix with the hydrogen, and (b) Concerns about plume contamination. These are issues for later study, but we may note at this point that experience with Cs dispensers already exists (ion engines), that Cs will solely be used in about 1-3%

proportion by mass, and that Cs has a high enough vapor pressure to ensure vacuum self-cleaning of surfaces at temperatures above $\approx$270K.

As a tool to assess the physical parameters and the performance potential of a Cs-seeded H_2 arcjet, we formulated a simple constrictor flow model, which is fully described in paper IEPC 95-236 (Ref. 1 appended). The model contains enough 2-D information to allow computation of the radial profiles of Tg, Te, velocity, etc., as they evolve down the constrictor. It, however, cannot account for near-electrode effects, and it also ignores viscous losses (except that, to keep these losses reasonable, the constrictor L/D ratio is kept below 10). The discharge is assumed to attach at the end of the constrictor, and an isentropic nozzle expansion is then assumed to occur through a given pressure ratio. This allows a simple calculation of thrust and other performance parameters.

The paper (Ref. 1) shows results of a parametric exploration using this model. The parameters varied were the seed fraction, chamber pressure, current and constrictor inlet Mach number (this last parameter controls the total enthalpy addition). The range of variation of these parameters (one at a time) was bounded roughly as follows:

—For seed fraction below $\approx$1.5% by mass, the electron temperature exceeded 7500K, because of the high fields, as noted before. This was taken as a limit beyond which there is a risk of ionization of the hydrogen itself, potentially triggering a rapid transition to a conventional, lower voltage arc burning in hydrogen.

—For seed fraction above $\approx$2.5% by mass the length-to-diameter ratio of the constrictor exceeded 10, probably leading to high viscous losses.

—For chamber pressures below 2.8 atm., again the high E/P levels led to Te being over 7500 K.

—For pressure above 4 atm, L/D exceeded 10.

—For currents lower than 16A, L/D also exceeded 10

—For currents higher than 19A, Te exceeded 7500K

—For inlet Mach number below 0.22, Te exceeded 7500K, and, simultaneously, the dissociation losses increased rapidly, due to the exit gas temperature rise

(This was manifest in the corresponding rise of Isp).

—For inlet Mach number above 0.25, Isp became lower than 750 sec.

All these results apply to a particular choice of constrictor radius (1.4 mm). The central (nominal) case operated at 10.1 KW power, V=595 Volt, $\dot{m} = 0.37 g/s$, had a constrictor L/D of 8.7, and delivered a specific impulse Isp=835 sec, with only 1% frozen losses. A complete calculation of efficiency was not possible, due to the limitations of the model, but frozen losses generally account for about 50% of the input power, so that, even allowing a 10% viscous loss and taking no credit for reduction of the voltage drops, one can expect overall efficiencies approaching 80%.

The paper also presents a simplified discussion of the major trends, based on a simple heat addition model, made possible by the relatively uniform radial distribution of power deposition.

In sum, this preliminary exploration has yielded very encouraging results, and we plan to pursue the idea further. Areas where obvious advances are needed are:

(a) Inclusion of viscous effects

(b) True 2-D modeling, including nozzle

(c) Simultaneous modeling of hydrogen ionization

(d) Stability analysis, particularly against ignition of a second (classical arc) mode

Other areas to be looked into are

—Possible segregation of Cs away from center of discharge

—Radiative losses (preliminary estimates show small losses, due to the full Cs ionization)

—Thruster thermal design

—Design of Cs dispenser

—Plume contamination

3. Two-Dimensional Modeling of Hall Thrusters

Hall thrusters have achieved some degree of technical maturity, and, given their simplicity and good performance in the middle Isp range, are currently the technology of choice for many missions. At the same time, significant improvements are still possible in this area: efficiency could be significantly raised, fluctuations need to be reduced, plume divergence remains an issue, and lifetime extensions would be welcome.

In contrast with the extensive empirical basis accumulated in Russia over the past 20 years, there is still a lack of detailed understanding of the various mechanisms at work in a Hall thruster, and, especially, a lack of reliable overall models which incorporate the proper physics and use it to project performance or life. This has been our motivation.

An earlier effort (Ref. 2), using a 1-D model, has yielded useful performance predictions capabilities, although it lacked any ability to suggest shape improvements or to predict erosion. This earlier model featured particularly the assumption that the electron flow to the anode was throttled by the radial magnetic field following Bohm's simple cross-field diffusivity formula. Adequately modeling cross-field diffusion is an extremely difficult task in plasma physics, and the success of the 1-D model using the simple empirical Bohm diffusivity encouraged us to develop a more ambitious 2-D version still using this diffusivity.

Collisionality plays a very minor role in the plasma flow in Hall thrusters (in fact, the onset of significant collisionality limits the maximum thrust density in these devices). Thus, the proper theoretical description should be kinematic rather than fluid. On the other hand, full kinematic modeling of the very fast electron dynamics was deemed beyond our numerical capabilities, except possibly for very simplified geometries (this may still be a useful research avenue, as shown by the recent work of Hirakawa and Yoshikawa, Ref. 3). It is also known (and this was early called Langmuir's paradox) that the electron population in plasmas is far closer to a Maxwellian distribution that would seem warranted by classical collision considerations; this appears to be due to the randomizing action of electrostatic fluctuations. Because of this, a compromise was struck in our model by adopting a fluid model for the electrons only, while using a Particle in Cell (PIC) description for ions and neutrals.

Whenever fluid descriptions are used, the price to pay is a difficulty in defining suitable models for transport effects. In our case, in particular, cross-field transport, as noted, is

the main issue, and it is fortunate that at least a plausible empirical model (Bohm's) is available. As will be shown, this ad-hoc procedure succeeds remarkably well in our case; this, however, leaves many questions still unanswered, such as the role of wall scattering, the transition to classical diffusivity, etc. These will be commented upon later, but they remain future research topics.

The model and its capabilities are described in paper IEPC 95-240 (Ref. 4, appended). It treats an arbitrary axisymmetric thruster, using a precomputed magnetic field from prescribed polepiece geometry. Electrons are placed in Boltzmann equilibrium and constant temperature along each magnetic line, with diffusion, mobility and heat conduction across lines of force which are derived from the diffusivity D_{Bohm}=kTe/16eB. Ions and neutrals are lumped into 50,000-100,000 macro-particles, which are moved at each time step in response to the prevailing electric field distribution. This field is updated, together with the electron properties, between ion-advance steps. Ionization is accounted for by generating new ion-electron pairs at each step in proportion to computed ionization rates. Quasi-neutrality is assumed everywhere, so that electron density follows directly from ion density after ion advancement.

The model was exercised for the conditions of the only existing detailed map of internal Hall thruster parameters, taken by Bishaev and Kim in 1978 (Ref. 5). The performance of the thruster was very well predicted (Isp=1475 sec vs. 1530 measured, $\eta = 0.50$ vs. 0.54 measured, I_{anode}=3.10A vs. 3.15 measured, I_{beam}=2.20A vs. 2.10 measured). Significantly, this agreement degraded rapidly when the Bohm diffusivity was either increased or decreased by 25%. In the case of a 25% decrease, the discharge was found to essentially quench. It is to be noted that this reduction is equivalent to a similar increase in the magnetic field B; the quenching appears to be the result of a reduced ionization rate due to too few neutralizer electrons penetrating the B field, and of the subsequent reduction in current, which further reinforces the trend.

It is also significant that the model was able to calculate accurately the ion current impinging on the insulating walls (1.1 Amp vs. 1.0 measured). Using the detailed ion impingement speeds and angles, combined with experimental sputtering yields, an erosion rate of $4 \times 10^{-9} m/sec$ was calculated, which compares reasonably with a measured $7 \times 10^{-9} m/sec$. Finally, the "twist" torque due to side magnetic force on the ions was also

computed and found to be 3.1% of the thrust times the mean radius. No data exists on this quantity for the Bishaev-Kim conditions, but a range of 2% to 8% was indicated in Ref. 6.

The detailed comparison of internal parameter distributions was less favorable, although the computed results were qualitatively correct. In particular, the peak ion density was predicted to occur closer to the anode than observed, and to reach values about twice too high. This may be associated with difficulties in modeling correctly the neutral injection pattern form the complex annular anode-injector used. The peak electron temperature (about 26 eV) was well predicted, but the data showed some unmodelled variation along magnetic lines, which may be due to magnetic mirroring. The calculated region of steep voltage drop (acceleration region) lies mostly outside the annular enclosure, while the data indicate most of the fall to occur just ahead of the exit. Perhaps this is related to inaccurate representation of the magnetic field shape, for which insufficient information was available.

A very interesting feature of the computation is its apparent ability to mimic the observed unsteady nature of the flow. In fact, all of the properties just discussed are time averages over a 0.5 millisecond window. In detail, the calculations contain fluctuations of current, temperature, etc, with amplitudes of ±15% and with a variety of characteristic frequencies. Of these, the two lowest ones (≈6 Khz and 28 Khz) appear to be related to neutral transit time through the channel and through the ionization region, respectively. There is also an 80 Khz component, possibly related to ion transit time, and components above 100 Khz, which may be contaminated by numerical effects, as this is the range of grid-crossing frequencies for the particles. Fluctuations of this same general type have been documented experimentally in many SPT-100 tests. Our computations appear to support their interpretation, advanced by V.M. Gavryushin (Ref. 7), as ionization relaxation effects.

The detailed fluctuation spectrum was found to be sensitive to details of gas injection and gas-wall interaction modeling, which is reminiscent of reported variability with operating conditions and with thruster aging.

Following these computations, efforts have been made to better characterize the critical cross-field diffusivity. Using the Bishaev-Kim data set, the electron flux was backed out, and from it the apparent cross-field diffusivity, averaged over the cross-section. This appears as a continuous line in Fig. 1. For comparison, the Bohm diffusivity, using our computed B field, is also shown, and is seen to be too high over the downstream half of

the channel, and too low near the anode. While the very indirect nature of the data make them unreliable, this appears to indicate approximately the correct average and trend, but a defective axial distribution. The "$1/B^5$" diffusivity curve is simply a curve fit used for evaluation; its incorporation into the model did yield an improved position of the peak ionization, but since the fit lacks any physical basis, it should not be generally adopted. Work is continuing on this point; there are indications that a combination of Bohm and classical diffusivity may explain the rapid rise towards the anode (where electron-neutral scattering is strong).

In summary, then, our Hall thruster hybrid PIC model offers exciting insights into the physics of the thruster, as well as a clear path towards applications for design. Some such applications are planned for the near future, in connection with microthruster design work under different sponsorship.

At the same time, our discussion has indicated several areas of model deficiency which need to be addressed. These include:

—Inclusion of electron-wall scattering as a cross-field transport mechanism

—Inclusion, similarly, of electron-neutral scattering

—Accounting for magnetic mirror effects

—Improvement of the magnetic model

—Improvement of the gas-wall model, including secondary emission details

—Adaptation to the TAL geometry, in particular the very short ionization length and the metallic walls.

Our work has also highlighted the need for additional detailed internal data in Hall thrusters. This will be addressed by the doctoral student responsible for this work (Michael J. Fife) under a separate grant from NASA, which will provide access to its Lewis R.C. facility and to an operational SPT-100 thruster.

4. Other Work Completed during the Reporting Period

Although initiated under an earlier Grant, our work on inlet ionization in MPD thrusters was completed during this reporting period, and was documented in Dr. Eric Sheppard's Thesis (Ref. 8) as well as in papers IEPC 93-218 and AIAA 94-3342 (Refs 9,10 appended). This work showed that ionization within a few mm. of the point where fresh gas enters the MPD channel can be explained on the basis of back-diffusion of charge pairs from the dense downstream plasma. It also established conditions under which convection will overpower diffusion and lead to discharge "blow off".

Also completed during this period was the arcjet model development by Dr. Scott A. Miller. This was documented in Dr. Millers' Thesis (Ref. 10) and (partially) in paper IEPC 93-219 (Ref. 12, appended). The bulk of the work had been reported earlier, in our 1993 Progress Report, as well as in Miller's paper AIAA 93-2101. This work advanced in a fundamental way the state of the art in arcjet modeling, by accounting for electron thermal non-equilibrium, viscous losses and a variety of other significant effects. Particularly important was the finding that electron temperature elevation explains the anodic attachment of the arc through a layer of cold outer gas, with no need for artificial conductivity floors. In Ref. 11, Miller also coupled the gas model to a thermal computation of the arcjet model, which showed only moderate feedback on performance, but allowed rational design and life estimations.

Another outcome of our work on arcjet modeling was a review by this author of this whole field, published as paper AIAA 94-2653 (Ref. 13, appended).

References

1. Folusho Oyerokun and M. Martinez-Sanchez, "A Study of Alkali-Seeded Hydrogen Arcjet Performance". Paper IEPC 95-236. 24th International Electric Propulsion Conference, Moscow, Sept. 1995.

2. C.A. Lentz, "Transient One Dimensional Numerical Simulation of Hall Thrusters. Paper AIAA 93-2491, 29th Joint Propulsion Conf., Monterey, June 1993.

3. M. Hirakawa and Y. Arakawa, "Particle Simulation of Plasma Phenomena in Hall Thrusters". Paper IEPC 95-164. 24th International E.P. Conf., Moscow, Sept. 1995.

4. J.M. Fife and M. Martinez-Sanchez, "Two-Dimensional Hybrid Particle-In-Cell (PIC) Modeling of Hall Thrusters". Paper IEPC 95-240. 24th International E.P. Conf., Moscow, Sept. 1995.

5. A.M. Bishaev and V. Kim, "Local Plasma Properties in a Hall-Current Accelerator with an Extended Acceleration Zone". Soviet Physics, Technical Physics 23 (9): 1055-1057, 1978.

6. K. Kozubsky "Disturbance Torques Generated by the Stationary Plasma Thruster". Paper AIAA 93-2349. 29th Joint Propulsion Conf., Monterey, June 1993.

7. V.M. Gavryushin, V.P. Kim, V.I. Kozlov, K. Kozubsky, G.A. Popov, A.V. Sorokin, M.L. Day and T. Randolph, "Study of the Effect of Magnetic Field Variation, Channel Geometry Change and Wall Contamination upon the SPT Performance, Paper AIAA 94-2858, 30th Joint Propulsion Conf., Indianapolis, June 1994.

8. Eric J. Sheppard, "Ionizational Non-Equilibrium and Ignition in Self-Field Magnetoplasmadynamic Thrusters. Sc.D. Thesis, MIT 1993.

9. E.J. Sheppard and M. Martinez-Sanchez, "Ionization Rate Models and Inlet Ignition in Self-Field MPD Thrusters". Paper IEPC 93-071, 23rd International E.P. Conference, Seattle, Sept. 1993.

10. E.J. Sheppard and M. Martinez-Sanchez, "Ionizational Ignition in Atomic Self-Field MPD Thruster Flows". Paper AIAA 94-3342, 30th Joint Propulsion Conf., Indianapolis, June 1994.

11. Scott. A. Miller, "Multifluid Nonequilibrium Simulation of Arcjet Thrusters. Sc.D. Thesis, MIT, Feb. 1994.

12. S.A. Miller and M. Martinez-Sanchez, "Non-Equilibrium Numerical Simulation of Radiation Cooled Arcjet Thrusters". Paper IEPC 93-218. 23rd International E.P. Conference, Seattle, Sept. 1993.

13. M. Martinez-Sanchez, "Arjcet Modeling: Status and Prospects". Paper AIAA 94-2653, 25th AIAA Plasmadynamics and Lasers Conf., Colorado Springs, June 1994.
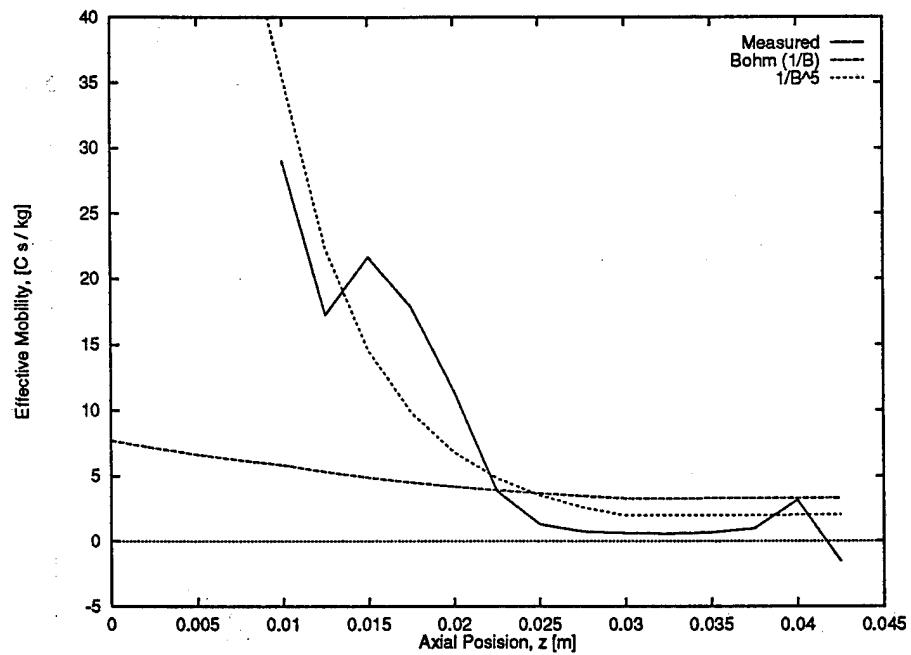
Figure 1: Comparison between effective electron mobility, Bohm (1/B) mobility, and $1/B^5$ mobility in the acceleartion zone of an experimental SPT.

AIAA 94-2653

ARCJET MODELING: STATUS AND PROSPECTS

Manuel Martinez-Sanchez

MIT, Department of Aeronautics and Astronautics
Cambridge, MA 02139

25th AIAA PLASMADYNAMICS AND LASERS CONFERENCE

June 20-23, 1994/Colorado Springs, CO

ARCJET MODELING: STATUS AND PROSPECTS

by

Manuel Martinez-Sanchez*, MIT
Cambridge, MA 02139

Abstract

This paper traces the evolution of arcjet thruster modeling to its current state of development, and discusses the most pressing theoretical uncertainties in the way of further progress. The thrust producing mechanism is well understood, and so is the general energy balance, leading to voltage prediction, provided anodic attachment is separately known. This particular problem is discussed in some detail. It is argued that 3-D arc root constriction is a very likely cause of at least some of the observed anode behavior, and should be theoretically investigated. Other issues examined are electron-molecule interactions, species segregation, and numerical efficiency in the face of ever-increasing complexity.

1. Introduction

Like many other practical devices, arcjets for space propulsion have evolved largely on the basis of a series of intuition-guided empirical developments, with theory providing at best a general background, and very little detailed help to the designer. While scientific data and sub-models have existed for a long time regarding the properties of arcs in general (i.e., Ref. 1), the interactions of arcs with

strong flowfields introduces so much additional complexity that until recently, there was little hope of being able to construct comprehensive models of the complete device. The situation is now rapidly changing due to the combination of greatly expanded computational resources, and renewed interest in refining arcjets for a variety of operational space uses. In synergy with these facts, new physical information is also being generated via a new generation of plasma diagnostics. The net result is an exciting rapid increase of our understanding of arcjets. Theory still lags substantially behind practice, but the gap seems now bridgeable for the first time.

In this paper we will review the arcjet modeling literature (Sec. 2), provide a synoptic summary of the controlling physics (Sec. 3), examine in more detail some of the more difficult mechanisms at work (Sec. 4), and discuss the numerical methods available to the modeller (Sec. 5). We conclude (Sec. 6) with a look ahead and a prognosis for the near future in this field.

2. Literature Review

This review will not attempt to be comprehensive, but will rather be used to illustrate the main lines of development of this area in the past.

2.1 Zero-Dimension Models

As discussed by Pfender [1] in his excellent 1978 review on arcs and arc heaters, the idea of using an electric arc for propulsion purposes grew out of the previous experience with arc gas heaters for chemical processing and other industrial uses. In an industrial arc heater the object is a uniformly heated gas exhaust, and devices such as magnetic arc rotators have been used to homogenize the temperature in a gas plenum. Drawing on this analogy, early electrothermal rocket models [2] evaluated frozen losses (mainly dissociation and ionization energy) by postulating uniform conditions in the "heating chamber", from which the gas was assumed to then flow through a nozzle under isentropic (frozen, or, for reference, chemically equilibrated) conditions. When

1

applied to arcjets, this procedure is fundamentally flawed, because of the combination of the strong segregation of hot and cool gas in an arc and the very non-linear variation of dissociation and ionization with temperature. Essentially, the frozen losses are confined to the arc itself, which may occupy a sizeable geometrical fraction of the arcjet throat, but carries only a minor part of the exhaust flow rate. Nevertheless, calculations based on such models did call attention to the large losses associated with frozen chemistry, and provided at least a qualitative explanation for the loss of efficiency at very high specific impulses.

2.2 Quasi-One-Dimensional Models

After the initiation of experimental work with constricted arcjets of the type still in use, the essential non-uniformity of the flow field was recognized and accounted for in models. For example, R.R. John et al [3] subdivided the flow into a core, a transition zone and an outer region, and constructed a simple analytical model as a vehicle for interpreting test results of their 30KW arcjet. This work identified the basic energy addition and loss mechanisms, including friction, chemical reaction, area ratio effects and others. Similar work during the 60's and 70's was reported, for instance by Weber [4] and by Topham [5], and, more recently, by, among others, Glocker et al [6], [7] and Martinez-Sanchez and Sakamoto [8], and Tahara et al [9].

The persistence of this type of quasi-one-dimensional modeling despite the increasing availability of an array of more elaborate methods is due to their recognized ability to mimic the most important aspects of arcjet operation and to provide reasonable performance estimates. In fact, if prediction of thrust and, to some extent, efficiency, were the only criteria by which models were to be chosen, there would be very little incentive for the vast increase in effort required at the next logical modeling level (2-D models).

As a sample of the quasi 1-D type of model, a brief description will be given here of that of Ref. 8. The flow is subdivided into a hot core of radius R_a (the arc, in the constrictor, or its wake in the nozzle) surrounded by isentropically expanding uniform gas, out to the radius $R(x)$ of the constrictor or nozzle. The arc grows at a rate determined by the supply of heat radially conducted from the arc core

$$\left(h_{ae} - h_{out}\right)\frac{d\dot{m}_a}{dx} = 2\pi R_a\, q_c \qquad (1)$$

where h_{ae} is the "arc edge" enthalpy, corresponding to the minimum temperature for electrical conduction (~7000K), and h_{out} is that of the cold outer gas. The arc carries a total flow $\dot{m}_a$, and q_c is the radial heat flux at the arc edge. The static pressure and the dynamic head $q = \rho u^2$ are assumed to be radially uniform (the latter based on its axial growth at the expense of p decay, if friction is ignored). The specific enthalpy h is modeled over broad ranges of temperature by $h = Q\,{}^p\!/_\rho$, where $Q = \gamma / (\gamma - 1)$ if an effective ratio of specific heats, γ, is defined. It can then be shown that the mass and enthalpy fluxes are

$$\rho u = \frac{\sqrt{Qpq}}{\sqrt{h}} \qquad (2)$$

$$\rho u h = \sqrt{Qpq}\,\sqrt{h} \qquad (3)$$

and the total enthalpy flux is as in Eq. (3), with an extra factor $\left(1 + \frac{1}{2Q}\frac{q}{p}\right)$. The important observation from (2) is that most of the mass flow occurs in the cool layer, whereas, from (3), most of the power flow occurs in the hot core. This has implications for overall arcjet behavior, which will be discussed later. From relationships such as (2) and (3) above, it follows that a radial profile of $h(r/R_a)$ is sufficient to specify most of the flow

2

variables. This profile is chosen from a solution to the local Ellenbaas-Heller equation (radial balance of Ohmic heating and heat conduction). The thermal and electrical conductivities are correlated to each other by a sort of Wiedemann-Franz law

$$\int_{T_e}^{T} KdT = B^2 \sigma \qquad (4)$$

where B is a parameter (2.79V for H_2, 1.58V for N_2). After this, the Ellenbaas-Heller equation gives a Bessel-function profile

$$\frac{\sigma}{\sigma_c(x)} = J_o \left(2.403 \frac{r}{R_a} \right) \qquad (5)$$

and, as a further approximation, conductivity and enthalpy are also related linearly to each other:

$$h \cong G \sigma \qquad (6)$$

$$\left(\begin{array}{l} G \cong 2.47 \times 10^5 m^3 \Omega / \sec^2 \text{ for} \\ H_2, \ 2.20 \times 10^4 m^3 \Omega / \sec^2 \text{ for } N_2 \end{array} \right).$$

Given these functional relationships, it is easy to construct expressions for the various integrated fluxes (mass, energy, current), and to derive ordinary differential equations (ODE's) expressing their conservation. The resulting set of ODE's has a singular point (sonic passage) which is forced to be at the constrictor exit by choice of stagnation pressure, given the mass flow rate. The arc attachment point needs to be externally supplied, and is usually placed at the constrictor exit. The stagnation temperature of the outer gas layer, which, as noted, carries most of the flow, is an important parameter, which needs to be separately estimated by knowledge of the thermal configuration of the arcjet; even in a water-cooled case, this estimation is made difficult by the heating effect of the cathode. By contrast, the starting (cathode end) arc enthalpy is an insensitive parameter which seeks its own level in a short distance.

The degree of accuracy obtainable from this level of modeling can be judged from Table 1, where comparison is made to data of Ref. 10 (20Kw, H_2, water cooled).

As noted in the caption in Table 1, the calculated column voltage is increased by an anode drop of 28V., after which agreement is good. In hot-wall cases, the required ΔV_a was, however, nearly zero, which may not be realistic. The thrust and related quantities (stagnation pressure, specific impulse) are well predicted. The "calculated" heat loss is simply the assumed anode drop times the current, and is shown mainly to reinforce the plausibility of the value chosen for ΔV_a.

Similar levels of accuracy are obtained with the model of Refs. 6-7, which also require choice of some adjustable parameters.

2.3 Two-Dimensional Models

The type of models discussed above have serious limitations concerning the details of the gas physics and flow dynamics. While, with some operator skill, such models can come close to providing valid performance predictions, they offer little hope for design improvement based on exploitation of one or other of the many competing effects present. The inflexibility arises from the need to postulate simple gas physics in order to construct manageable integrated fluxes, whose evolution can then be traced with ODE's. Relaxing these constraints requires a detailed 2-D or 3-D description of the problem.

The initial work on 2-D (axisymmetric) arcjet modeling is due to Watson and Pegot [11], whose focus was the constrictor region alone. The gas assumed to be in thermodynamic equilibrium, which is reasonable as long as the anodic attachment region and the nozzle are not examined. Viscous and heat conduction effects were included. The calculation was made by spatial marching, using what would now be called a Parabolized Navier Stokes approach. This work was seminal

3

in clearly illustrating the interplay of Ohmic heating and flow acceleration and in showing in detail the extreme nonuniformity of the flow field. Efforts have been recently made [12] to supplement the Watson-Pegot model with near-electrode and nozzle sections.

Typical of the state of the art about 2-3 years ago are the models of Butler and King, of Rocket Research Co. [13,14] and of Rhodes and Keefer [116] of UTSI. The single-fluid model of Butler-King can handle different gases, and it covers the complete thruster, but it retains the Watson-Pegot equilibrium assumptions. As a consequence, the electron density and the electrical conductivity are essentially zero outside the arc, and no simple mechanism exists for current to reach the anode. This is remedied by introducing a "conductivity floor", σ_o, of the order of 0.1-1 (ohm)$^{-1}$/cm. The precise σ_o is selected to provide a good prediction of total voltage, and its effect on calculated thrust is relatively minor (Fig. 1, from Ref. 14). This is analogous to the procedure used in the 1-D model of Ref. (8), where ΔV_a is externally supplied to match voltage, with minor effects on thrust. Also in common, once the constant conductivity floor σ_o is imposed, one loses the ability to predict the current distribution along the anode wall. More precisely, the model does calculate this distribution, but there is no feedback to the local σ_o value; as we will see, this feedback leads to a certain amount of axial constriction, which is here ignored. These difficulties were recognized by the authors [14], and a two-fluid model is under development. Cappelli et al [15] have compared the exit-plane predictions of this code to data for a 1 KW H_2 arcjet. Velocity is well predicted, but heavy-particle temperature is under-predicted significantly on the jet axis at the higher powers.

A similar situation exists with respect to the model of Rhodes and Keefer [16]. This model incorporates several physics refinements, such as a calculation

of radiative losses, plus a full set of molecular transport effects. However, once again, equilibrium forces a very low conductivity outside the arc, and an artificially elevated value is used for T<10,000K. The current distribution over the anode is specified a-priori, which for a given voltage, results in excessive Ohmic dissipation, requiring a correction factor of 0.75. Of course, the anode is not equipotential in general when current distribution is arbitrarily prescribed.
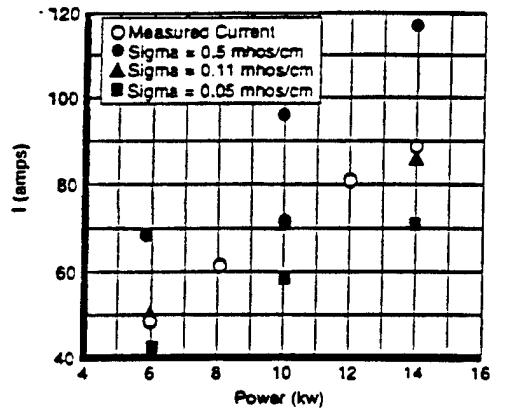
Variation of Predicted Current with Electrical Conductivity Floor.
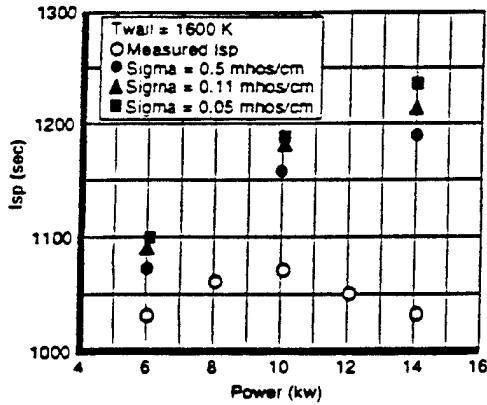
Variation of Predicted Isp with Power for Different Values of Conductivity Floor.

Fig. 1: Effects of conductivity "floor" (from Ref. 14)

A comparable model, with a single temperature and Saha equilibrium, has been presented by Fujita and Arakawa [17]. Once again, an ad-hoc remedy was necessary in order to generate sufficient near-anode conductivity, and it took the form of an ionization fraction minimum of

4

10^{-5}. The single-temperature assumption is probably even less adequate in this case, because Argon was the test gas, and heavy monoatomic species couple very poorly to electrons in terms of energy.

Other single fluid models have been reported, most recently those of Andrennucci et al [18] and Okamoto et al [19]. In Ref. (18), the focus is on the fluid dynamics, and Ohmic heating enters as a prescribed input term in the energy equation only. In Ref (19) the temperature and ionization fraction distributions are peculiar, with maximum values ahead of the arc; in fact, from the reported current vector maps, no arc is evident, only a convergence of current lines towards the conical cathode tip.

These equilibrium 2-D models yield valuable insights on phenomena occurring in various parts of the thruster, but care must be exercised to select those effects which are not badly affected by the artificial correction factors introduced. As far as overall performance prediction ability, they do not markedly improve upon the simpler 1-D models.

The first model to abandon the equilibrium assumption was that of Miller [20]. His model endows the electrons with a separate temperature ($Te \neq Tg$, thermal non-equilibrium) and tracks the rates of ionization and recombination, rather than using Saha equilibrium at T_e. This requires a separate electron energy equation, which, aside from increasing the algebraic complexity, also requires special integration procedures due to its very short characteristic time. Miller also included other refinements, such as ion-electron ambipolar diffusion and finite molecular dissociation rates, plus a very detailed calculation of molecular and electronic transport properties. Flow swirl is accounted for, although its role appears to be minor. Only Hydrogen was modeled, although extension to pure Nitrogen is straightforward, and extension to N_2-H_2 mixtures is possible, but laborious.
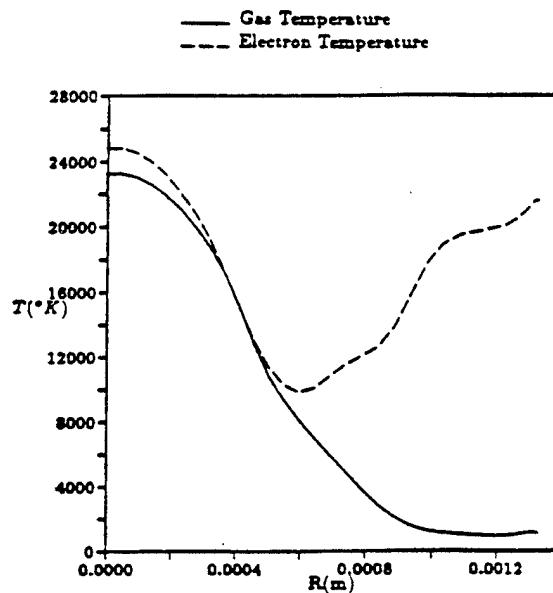

Fig. 2: Radial Profiles of Gas and Electron Temperature 0.25mm Downstream of the Constrictor Exit for the Baseline Case Arcjet Simulation (from Ref. 31)
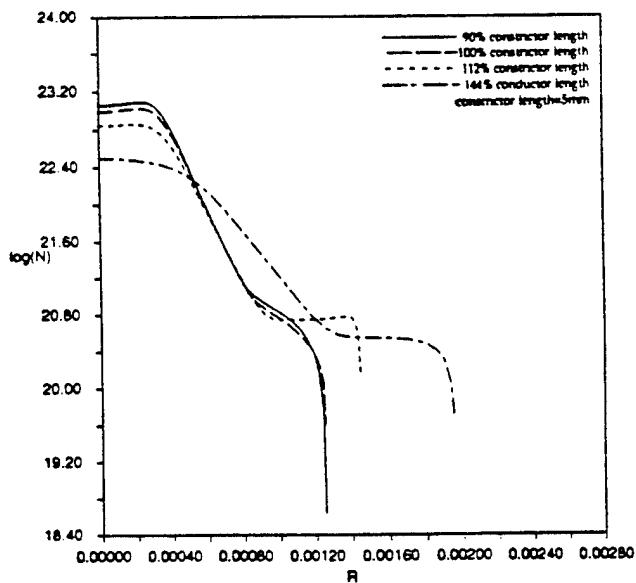

Fig. 3: Radial profiles of electron density for conditions of Ref. 20

$(\dot{m} = 0.1g / s, I = 60A)$, at several axial sections near the constrictor's end.

$(N$ in m^{-3}, R in $m)$

5

The main benefit gathered from these improvements was the ability to calculate the detailed current path outside the arc proper, all the way to the anode wall. The essential point is the strong thermal nonequilibrium existing in what we could call the "anodic bridge" region, namely, the annular region connecting the arc at the constrictor exit to the initial part of the nozzle wall. This is illustrated in Fig. 2, which belongs to a simulation of the radiation cooled 20KW H_2 arcjet of Glocker et al [21]. In the arc core $Te \cong Tg$ despite the very large Ohmic power input to the electrons; this is because of the high degree of ionization, which ensures strong collisional coupling to the heavy particles. But when we move outside the core and n_e falls rapidly, this coupling is weakened to the point that T_e remains in the 10,000-20,000K range, while Tg asymptotes to the outside gas temperature (~1000K). This elevated Te makes it possible for the ionization rate to keep up with recombination and diffusive losses and to maintain an electron density ~$10^{20} m^{-3}$ right up to the wall (Fig. 3). This represents an ionization fraction of only 10^{-4}, but is sufficient to provide the required electrical conductivity in this critical region. The resulting current distribution to the anode is fairly concentrated in the axial direction (Fig. 4). One word of caution needs to be advanced here: Miller's model, despite its success in self-consistently determining the current path downstream of the constrictor, is still forced to model the constrictor itself as an insulator; otherwise, the current attachment is seen to creep further and further forward as the simulated time progresses, in situations where downstream attachment is known experimentally to occur. We will return in Sec. 4 to this problem, and will also use Miller's model to illustrate a number of effects and point to additional unresolved issues. We close this discussion with some performance prediction results (Table 2 and Fig. 5) from Miller's model, again compared to data of Ref. 21. The degree of accuracy is comparable to that obtained using the 1-D models, but, of course, with less empiricism.

Several other models have recently appeared in the literature, or are under current development, which seek to build upon the lessons so far learned, in particular the need for non-equilibrium modeling. This includes the 2-Fluid version of Butler and King's model, as well as work by Krier et al [22] and Rhodes and Keefer [23]. Babu and Subramaniam [24] have initiated work on detailed accounting for vibrational nonequilibrium in molecular arcjet working gases. This effect, on which more will be said in Sec. 4, is potentially important in N_2-containing gases, such as those deriving from ammonia on hydrazine propellants.

A somewhat separate area of modelling is that concerned with plume flows. Here the impetus derives from contamination concerns, as well as from the ready availability of optical and other data on arcjet plumes. From the modeling viewpoint, plume flows strongly emphasize transport and non-equilibrium effects, even, as Liebeskind et al have pointed out [25], calling into serious question the use of continuum models (the mfp at the exit plane of their 1KW arcjet was seen to be several mm, for a 10mm. diameter). However, direct velocity measurements at the exit plane [26] still indicate insignificant slip between species. Boyd, Beattie and Cappelli [27,28] have developed and validated Monte-Carlo based models for these plumes showing a large degree of rotational temperature nonequilibrium. In a related effort, Fasoulas et al [29] have modeled the N_2 plume of a hybrid electrothermal-electromagnetic thruster used at Stuttgart Univ. for reentry simulations. In this case a continuum approach was used, and care was taken to include vibrational, as well as electron thermal nonequilibrium. The N_2 low-density chemistry was also modelled, and good agreement was found to experimental data.
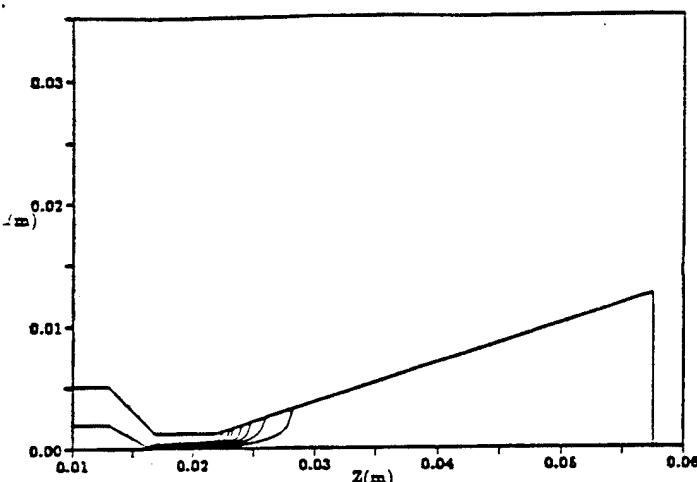
Fig. 4: Current Streamlines for the Baseline Case Arcjet Simulation (from Ref. 31)
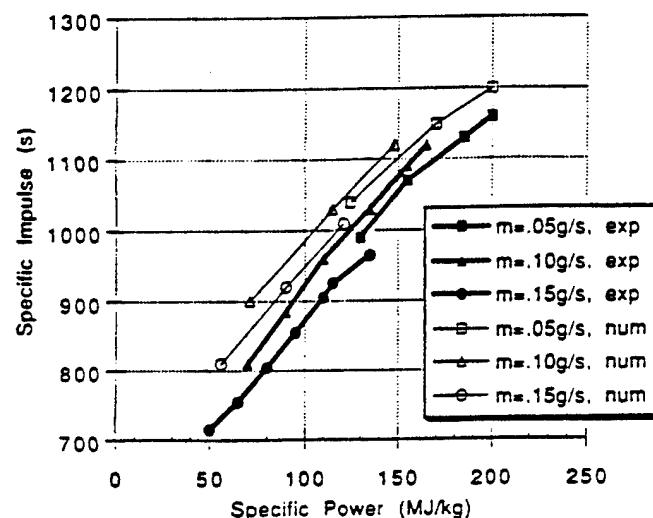
Fig. 5: Comparison of Predicted Specific Impulse to Experimental Data for German TT1 Radiation-Cooled Arcjet (from Ref. 31).

Case		Voltage	
I(A)	$\dot{m}$(g/s)	Numerical	Experiment
70	0.05	89	85
100	0.05	85	78
120	0.05	83	77
60	0.10	118	117
100	0.10	115	112
130	0.10	113	111
60	0.15	140	127
95	0.15	138	120
130	0.15	137	118

Table 2: Comparison of Discharge Voltages for the Cases in Fig. 5

3. The Essential Arcjet Physics

The art of modeling consists of retaining what is fundamental for explaining a particular effect, while discarding or approximating what is not. This Section will attempt to provide some of this perspective for arcjets. Some of the points to be made are well established, others are little more than informed guesses based on as yet incomplete information.

3.1 Prediction of Thrust and Specific Impulse

This is the easiest of the goals of a thruster modeller. In the case of an arcjet, our discussion of 1-D models (Sec. 2.2) can serve as our starting point. It was noted there that very little mass is carried inside the arc; in essence, the arc acts as a fluid-dynamic partial plug on the flow, so that, if A_a is the arc cross section suitably defined and A the constrictor cross section, the flow-carrying area is $A-A_a$. The flow chokes at the constrictor exit, where this

area is least, and, if $P_{o,out}$ and $T_{o,out}$ are the outer flow stagnation pressure and temperature,

$$\dot{m} = \frac{P_{o,out}(A - A_a)}{c^*_{out}} \qquad (7)$$

with c^*_{out} is the familiar "characteristic speed" of a rocket chamber, proportional to $\sqrt{R_g T_{o,out}}$ (R_g being the gas constant). On the other hand, the also familiar "mechanical" interpretation of a rocket's thrust states that this thrust (F) arises from the lack of a reaction surface for $P_{o,out}$ in the area of the throat (times a nozzle coefficient, c_F, of order 1-2, accounting principally for the pressure forces on the diverging nozzle bell):

$$F = c_F P_{o,out} A \qquad (8)$$

Notice that the whole constrictor area A is used, because P is constant across it. Aside from some incidental change in c_F due to peculiarities of the arcjet flow, Eq. (8) is as it would be in the absence of the arc, but Eq. (7) is very different. The specific impulse Isp is given by

$$g I_{sp} = \frac{F}{\dot{m}} = \left(c_F c^*_{out}\right)\frac{A}{A - A_a} \qquad (9)$$

where the factor in parenthesis would obtain with no arc.

Eq. (9) shows the crucial elements for successful specific impulse prediction:

(a) The stagnation temperature of the outer gas needs to be well predicted. In an operational sense, this highlights the importance of regeneration cooling, or of any steps taken to raise the temperature of the outer gas (this may not necessarily imply raising the anode wall temperature, because the thermal boundary layer is quite thin).

(b) The size of the arc at the constrictor exit needs to be accurately predicted. Since the arc growth is a result of radial diffusion of Ohmic heat into the co-flowing outer gas, the implication is that the thermal diffusivity and the electrical conductivity must be modeled accurately. This may not require, however, more than a parametric transport property representation which is faithful "in the large", even if some level of detail needs to be sacrificed. As an example, the arc radius computed by the crude model of Ref. 8 is compared in Fig. 6 with optical measurements of Ref. 10.

Operationally, the factor $A/(A-A_a)$ in Eq. (9) implies that the constrictor length and diameter should be designed such that the arc comes as close as thermally allowable to the constrictor wall. Since different gases and different operating points lead to different arc radii, this fact needs to be also taken into account. For example, the speed of sound in N_2 is about 1/4 that in H_2 at the same temperature, giving the arc 4 times longer growth time in a given constrictor length when running in N_2. There is also some difference in heat diffusivity (as characterized for example by B in Eq. (4), but, to a first order, a satisfactory constrictor for H_2 will lead to premature attachment if run in N_2, as noted in Ref. (21).

Other factors affecting thrust prediction include the actual velocity profile in the arc periphery, and the effects of wall friction. As an example of the latter, consider the constrictor H_2 flow in the 20 KW arcjet of Ref. (21). The Reynolds number based on its 5mm length is ~10^4, giving a total laminar boundary layer thickness of about 0.17mm (corroborated by the computations of Ref. (20)) and a net viscous drag of 0.016N. There is additional drag in the nozzle, but its magnitude per unit length $\left(\pi \rho u^2 R \, c_f\right)$ decreases rapidly, so that the net viscous drag is of the order of 0.05N, compared to thrust levels in the 0.5-1.5 N. The relative effect will be somewhat larger at smaller powers (roughly as (Power)$^{-1/4}$. The

8

message here is that, while important because of the low Reynolds numbers involved, arcjet viscous thrust losses remain secondary.
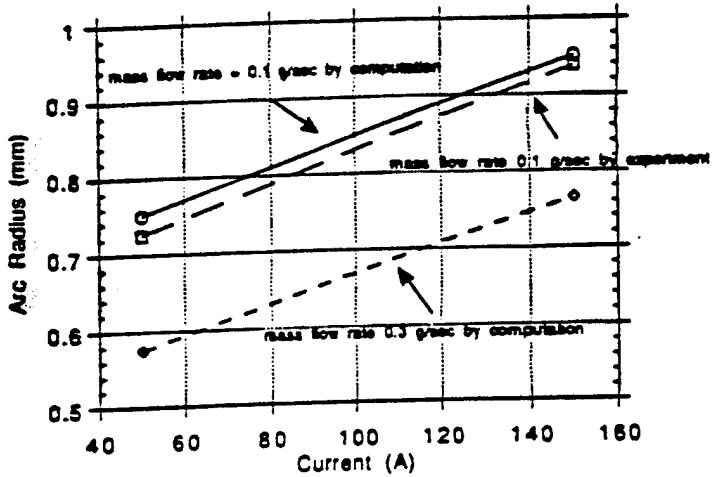

Fig. 6: The experimental radius is that for 1/e. luminosity decay compared to centerline(Ref. 8)

As interesting as what is essential for thrust prediction is what is not. In particular, Eqs. (8) and (9) show that the conditions inside the arc itself (dissociation, ionization, non-equilibrium, etc) are fairly irrelevant in this regards as long as the arc radius can be calculated. This partly accounts for the success of many simple models in thrust and specific impulse predictions.

3.2 Prediction of Voltage

For a fixed current, voltage determines the power absorbed by the arc, and its calculation, involving as it does an accounting of energy losses, is generally more difficult than that of the thrust.

The voltage is naturally divided into the column voltage and the electrode drops. The main difficulty with column voltage is the determination of column length, i.e., the location of the anodic arc attachment. This is one of the main unresolved issues in the field, and we will return to it in Sec. 4. If the length is separately known, the field E=dV/dx is no more difficult to calculate than the arc radius R_a. This follows from the radial energy balance

$$\pi R_a^2 \overline{\sigma} E^2 \cong \frac{\overline{K}(T_c - T_e)}{R_a} 2\pi R_a \qquad (10)$$

or, using $\overline{\sigma} \approx \frac{1}{2}\sigma_c$, with c referring to the arc centerline,

$$E \cong 2\frac{\sqrt{\overline{K}(T_c - T_e)/\sigma_c}}{R_a} \qquad 11)$$

The quantity in the square root can be recognized at the B^2 of Eq. (4), and, in fact, the Ellenbaas-Heller equation, as solved in Ref. (8), yields simply

$$E = \frac{2.4B}{R_a} \qquad (12)$$

The phenomena in the cathode spot area are too complex for the level of modeling likely to be of interest for propulsion, but at the same time, their performance impact is summarized by one insensitive quantity, namely the voltage drop ΔV_c, for which empirical information does exits [1], [30]. A separate issue relates to cathode lifetime, which has so far largely defied modeling, because, in addition to mass loss, one would also need to deal with morphology changes (whisker growth, for example), which tend to be the life-limiting factors in arcjet applications.

Accurate prediction of the anode fall, ΔV_a, is probably bound up with the issue of attachment determination (Sec. 4). On the other hand, the magnitude of ΔV_a is becoming more amenable to first-principles calculations. Two components of

9

ΔV_a can be discerned: (a) A resistive drop occurring in the electron-deficient (but still quasi-neutral and collisional) layer adjacent to the anode. This layer is thin (~0.1mm) and is determined by the balance of ambipolar losses to the wall and excess ionization sustained by the enhanced radial field. The computations of Miller [20,31] have been able to resolve this sublayer in the context of a whole-thruster simulation. Fig. 7, from Ref. (20), shows a profile of voltage from the cathode, along the arc axis and across the anodic bridge to the anode surface. The rapid, but resolved, voltage increase near the anode surface can be noted.
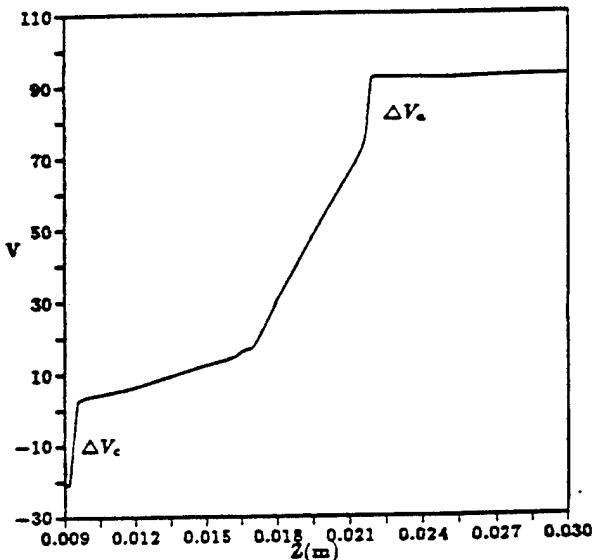
Fig. 7: Electric Potential Axial Profile for the Baseline Case Arcjet Simulation (Ref. 31).

(b) A sheath voltage drop, typically negative (anode below local plasma potential), which is required to turn back the excess thermal flux of electrons beyond those required by the circuit. This contribution is $(\Delta V_{a,s} < 0)$, given by

$$j = en_e \left[\frac{\bar{c}_e}{4} e^{\frac{e\Delta V_{a,s}}{kT_e}} - 0.61 v_B \right] \quad (13)$$

where n_e is the electron density at the sheath edge, $\bar{c}_e$ is the mean thermal velocity of electrons, and $v_B = \sqrt{kT_e / m_i}$ is the Bohm velocity, with which ions enter the ion-attracting sheath. Here j is the local current density at the anode surface, which needs to be self-consistently computed at the same time.

The preceding description of the anode is not incompatible with the possibility of three-dimensional constriction (see Sec. 4), but actual resolution in a 3-D computation is still beyond reach.

In summary, adequate calculations of voltage, and hence efficiency, are becoming possible, although many models are still incapable of direct determination of anode drops. This, plus uncertainties in cathode and column voltages, typically yields scatter of ±20-40V in reported results.

3.3 Prediction of Heat Losses

This is important from the thruster integration point of view, in addition to its direct effect on efficiency. The dominant contributor to wall heat flux is simply the product of anode drop times current, with ordinary conduction/convection playing a secondary role. While this somewhat facilitates the performance modeling task, it also means that an accurate prediction of the heat flux distribution, and hence of the peak wall temperature, depends critically on being able to calculate the current distribution at the anode, which, as we have seen, is still somewhat elusive. Once the wall flux is determined, it is a relatively easy task to calculate the temperatures throughout the anode block, accounting for either radiation or regenerative cooling. One caveat in this respect is that the wall thermal reaction time (a few seconds) is orders of magnitude longer than the flow reaction time (tens of microseconds), so that a fully coupled computation is impractical. Fortunately, as has been shown by Miller [31], the detailed wall temperature distribution has only a minor effect on both,

10

performance, and current distribution in the plasma (as long as the gas temperature is nearly correct). It appears that one or two cycles of iteration on the wall temperature, starting from a reasonable guess, are sufficient for convergence.

As an example, the heat flux distribution for three conditions from Ref. [31] are shown in Fig. 8. Here the wall temperature was pre-assigned, of the order of 1100K. With these fluxes as inputs, a computation of the heat flow in the thruster body, including radiation boundary conditions on the outside, and partial regeneration to the incoming hydrogen, as in the experiments of Ref. (21), yielded the wall temperatures of Fig. 9, with a hot spot in the anode attachment area. Repeating now the flow computation, with account for these wall temperatures, yielded almost the same heat fluxes, and modified the specific impulse to the extent shown in Fig. 10.

Fig. 9: Anode Wall Temperature at $\dot{m} = 0.1g/s$ for Three Applied Currents (Ref. 31)

Fig. 8: Heat Flux to anode at $\dot{m} = 0.1g/s$ for three applied currents (Ref. 31)
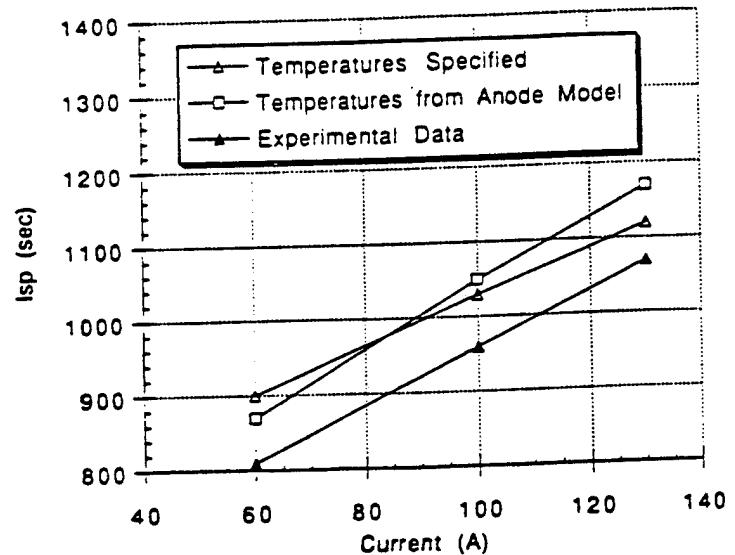
Fig. 10: Effect of Anode Model Coupling on Predicted Performance for $\dot{m} = 0.1g/s$ (Ref. 31)

11

4. Some Modeling Challenges

The preceding section may seem to imply complacency about the current status of arcjet modeling. But, in fact if we did not have the empirical data base we have about the current standard arcjet design, it is doubtful we would be able to "invent it" in software. Similarly, with the current modeling capabilities it is not easy to break away from the beaten path and realistically evaluate new designs (including such apparently minor variations as alkali seeding or subsonic attachment). The reason is that there remain several basic effects which are poorly understood, and others where the basic scientific data exist, but have yet to be incorporated in our models. This Section will briefly review the most salient of these issues.

4.1 Arc Attachment

As implied in the discussion so far, arc attachment at the anode looms large as a problem area. To different degrees, all existing models are forced to incorporate external information about it in order to proceed.

In the physically detailed model of Miller[20],[31] there remains a troublesome tendency for the arc attachment to migrate upstream, which is checked by modelling the constrictor itself as an insulator. It will be useful to examine more closely the assumptions used in that model, as a basic for further discussion. As noted in Sec. 2, ionization is kinetically controlled using the equation (in steady state).

$$\nabla \cdot \left(n_e \bar{v}_i \right) = \dot{n}_e \qquad (14)$$

where $\dot{n}_e$ includes an ionization rate (strongly dependent on T_e) and a recombination rate (depending on n_e). The ion velocity $\bar{v}_i$ is the sum of the mean mass velocity, $\bar{u}$, plus the "diffusion velocity" $\bar{V}_i$, and in this model, $n_e \bar{V}_i$ is written as

$-D_a \nabla n_e$, where D_a is the ambipolar diffusivity. Furthermore, it is assumed that only the radial component of $\bar{V}_i$ is strong enough to warrant consideration. The electron temperature, T_e, which controls ionization, is found from a detailed local energy balance, including Ohmic heating, ionization work, collisional cooling by heavy particles and electron heat conduction. As shown before, the heavy gas temperature (controlled by its own energy equation) and the gas velocity, are found to be nearly undisturbed in the anode region despite the current bridge.

The picture that emerges from this set of assumptions and partial results is that, in the 2-D steady state, neutral gas enters the anodic bridge at about sonic velocity, and is subjected to the ionizing action of the overheated electron population crossing this bridge. The position of the "leading edge" of the resulting ionization region results from the combination of forward electron heat diffusion, and the finite ionization delay time implicit in Eq. (14). This last effect is probably not controlling, because a slight additional T_e elevation can rapidly multiply the ionization rate to the level required. The "trailing edge" of the anodic bridge area results similarly from downstream electron heat diffusion and net recombination once T_e falls below some minimum value. Here the kinetic delay does play a role, because T_e does not control recombination rate and, there is a diffuse recombination trail, in contrast to a fairly abrupt ionization leading edge. The point to be made about this leading edge is that the electron energy equation, which determines the diffusive spread of the high T_e region, does not contain a strong downstream convective term, as the T_g equation does; wherever the dissipative bridge may be located at a given time, a certain region ahead of it receives electronic heat conduction $-K_e \nabla T_e$, and the bridge tends to move forward. Incidentally, the same cannot be stated about the downstream "edge", because the dissipation rate, which feeds T_e, decays

rapidly once the flow divergence spreads the arc.

It appears, therefore, that in an anodic bridge sustained only by hot electrons, with no heavy gas disturbance, there is no obvious effect capable of pushing the bridge downstream. Either a surface effect is required that will anchor the arc foot, or some stronger involvement of the heavy gas must occur. The first of these alternatives is unlikely, because, unlike the cathode, the anode is a fairly passive structure in general. As to the second alternative, if the heavy gas temperature remained fairly well coupled to the gas temperature, convective transport would then imply counterflow heat diffusion in the frontal part of the anodic bridge, with a clear trend to sweep the bridge downstream. Let us examine this point more closely.

The relative strength of the various terms in the electron energy balance in the anode attachment region for the baseline case $(\dot{m} = 0.1g \, / \, sec, \, I = 100A)$ of Refs. (20,31) is illustrated in Fig. 11, from Ref. (31). The input is clearly Ohmic heating, and the energy sinks are ionization, dissociation and collisional loss, with similar contributions (although ionization dominates very near the wall). It would therefore appear that we have a borderline situation, such that an increase in density, which favors collisional transfer, should bring about a significant heavy temperature increase in this region. This was investigated by considering a range of $\dot{m}$ from 0.05 to 0.15 g/sec, at constant (Power/$\dot{m}$), such that the main effect is a density change. What was found (Fig. 12) is that, as density increases, the arc constricts more, in response to a decreased heat diffusivity and the whole attachment region spreads further downstream to lower density regions. The gas temperature remains nearly undisturbed, and the electron temperature continues to reach the 20,000-30,000K level near the anode.
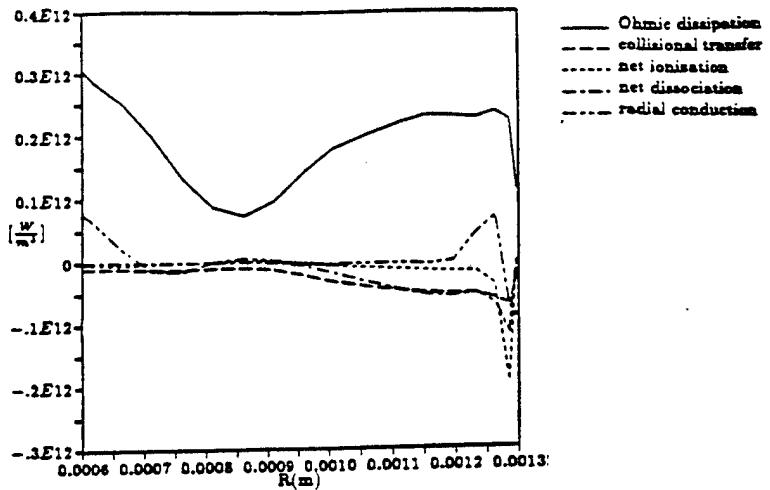

Fig. 11: Radial Profiles of Some Terms in the Electron Energy Equation in the Current Attachment Region Just Beyond the Constrictor Exit (Ref. 31)
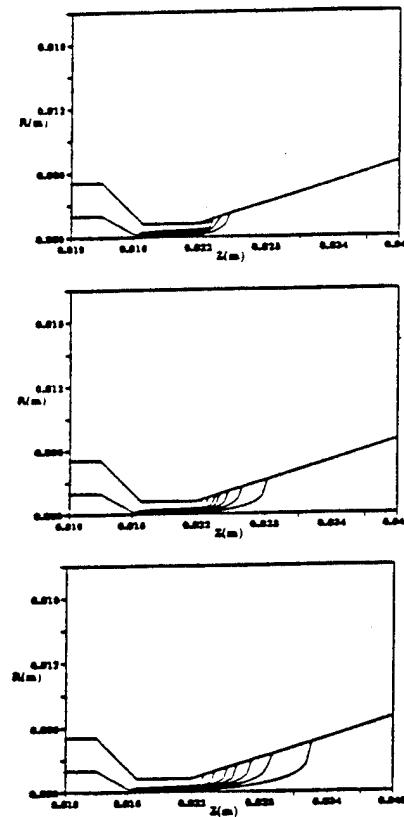

Fig. 12: Enclosed Current Contours for $\dfrac{P}{\dot{m}} \approx 115MJ \, / \, kg$: $I = 60A, \, \dot{m} = 0.05g \, / \, s$ (top);

$I = 100A, \, \dot{m}0.10g \, / \, s$ (middle); and

$I = 130A, \, \dot{m} = 0.15g \, / \, s$ (bottom) (Ref. 31)

13

Perhaps one should also investigate variations in the collisional coupling model (which is based on the δ factors quoted by Sutton and Sherman [32], as a possible route towards higher T_g and more convective effects.

4.2 Azimuthally Non-Diffuse Attachment

Closely allied with this subject is the issue of whether the axial symmetry assumption is valid. It is conceivable that the arc bridge might become three-dimensionally constricted at some point, resulting in attachment via "spokes" (which would rotate due to the flow swirl). In that case, the much higher local plasma density in the spoke would indeed elevate T_g (as in the arc core itself, see Fig. 2) to near T_e, and the attachment physics would radically change. In particular, models such as those of Maecker [33] and its follow-on by Yamada et al [34] now become relevant. Maecker argues that an arc moves by a superposition of mass motion of the heated gas and motion of the high temperature zone with respect to the gas. In a steady arc in cross flow, such as the anodic bridge, these contributions add up to zero velocity. Maecker proceeds to relate the local curvature of the arc to the cross-flow velocity (as in a horizontal arc subject to upwards convective flow), and Yamada et al [34] extend the model to calculate the point of attachment to a cylindrical anode. Aside from the relative crudity of some of the assumptions made (for example, the cross-flow speed in the arc core is set equal to the external normal speed, times the inverse density ratio, as if the flow direction remained undisturbed), one needs to keep in mind that the basic Maecker's model is based on a "bent core", with high gas temperature. Three-dimensional constriction appears necessary for this.

This problem of the stability of the axisymmetric solution remains largely unexplored. Miller [31] performed some linearized electrothermal stability analysis, assuming only planar disturbances with an axial wave vector. Although the axisymmetric stability problem would involve tangential wavevectors, the difference may be small, because, as noted, convective effects play a minor role in the basic solution. The results indicated stability for the conditions of the numerical studies, but they also showed that instability would result at higher current densities and lower ionization fractions; given the inaccuracies in the stability model (uniform background, undisturbed heavy species), the potential for constriction cannot be dismissed. Fig. 13, for example, maps the stability region as a function of
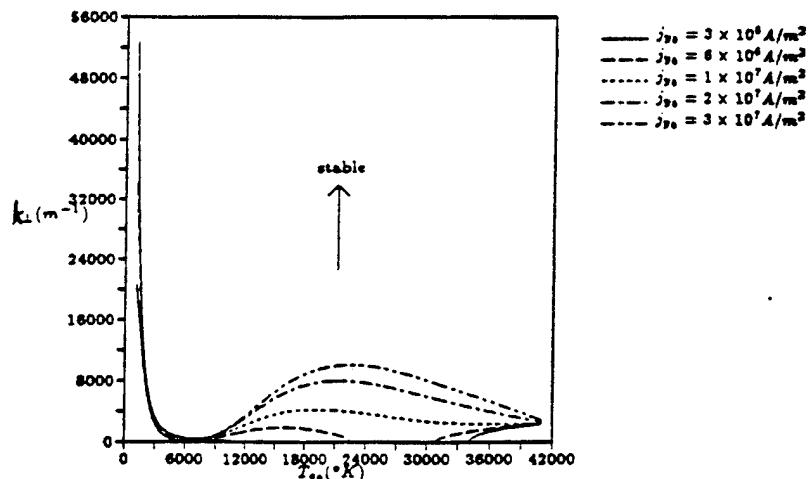

Fig. 13: Neutral Stability Lines as a Function of the Zeroth Order Electron Temperature and Current Density with Nonequilibrium Ionization (Ref. 31)

normal current density. Modes with wave number $k_\perp \leq 5000 m^{-1}$ $(\lambda \geq 1mm)$ can become unstable when $T_e \sim 25,000K$ if the basic currents density exceeds $10^7 A/m^2$; the approximate peak current density in the baseline case (0.1 g/sec, 100A) was 3×10^6 A/m^2.

More refined stability studies of the attachment region are desirable, given the important implications of constriction. These studies are analytically challenging, and, with steady progress in the numerical area, perhaps a direct 3-D numerical attack is a near-term possibility. An

14

interesting intermediate course would involve numerical solution of a <u>linearized</u> 3-D model, starting from a converged 2-D simulation, although any linear analysis will miss the constricted end state, which can only be captured by a full 3-D simulation.

Some experimental evidence of 3-D constriction in the attachment area has been reported by Harris et al [35], who tested a radially segment arcjet and observed generally non-symmetric distribution of current to the segments, with random fluctuations, indicative of a multi-filament structure of the anodic bridge.

Similar experiments, but with axial segmentation of the attachment region, were performed by Berns et al [36]. In this case, the attachment was confined to an extended cylindrical region upstream of the nozzle throat, as in the older Giannini arcjet design [37], with arc stabilization being provided mainly by the flow swirl. Berns et al observed oscillations in the segment currents and overall voltage which indicated downstream convection of the attachment point until a new re-strike occurred near the cathode, presumably when the local arc-to-anode voltage in that region exceeded some threshold. This same re-strike behavior had also been mentioned by Pfender [1] as being common in plasma troches. In Bern s' study, when the arc foot passed through the throat to the supersonic region of the nozzle, the operation tended to be re-strike free, but the incidence or absence of re-strike is not well documented for the usual supersonic attachment designs. In any case, their occurrence in the subsonic attachment case appears to lend support to the view that the anodic bridge may be constricted in a 3-D sense, because, as noted, this should then lead to its convection by the flow.

4.3 Molecular and Molecule-Induced Nonequilibrium

A very different area where modeling needs improvement is that of nonequilibrium molecular effects. These include slow kinetics or freezing of vibrational and rotational modes in the nozzle expansion (certainly in the plume), as well as distortion of the electron energy distribution associated with strong cross-sections for inelastic electron-molecule collisions.

Of these two issues, the first is probably the least significant, although uncertainties remain. Zube and Myers [38] were able to measure electronic excitation temperature, as well as rotational and vibrational temperature, in a 1KW H_2-N_2 arcjet, at several points in the supersonic nozzle. They found that the excitation temperatures remained above 10,000K at the nozzle exit, but the apparent indication of a very high exit-plane T_e was dispelled by a more refined analysis by Zube and Auweter-Kurtz [39], using a method by Park [40] to correct for lack of Boltzmann equilibrium among electronic states. The true exit plane T_e was found to be 3000-4000K, in agreement with model results by Miller [31] and with measurements by Hoskins et al [41]. More important for the present discussion, the vibrational temperature was found in Ref. (38) to track closely the rotational temperature during the nozzle expansion, both of them decaying to 2500-3000K at the exit plane. In contrast, in a 5-10KW N_2 arcjet study, Tahara et al [9] observed that the rotational temperature, after an initial drop from an already high 9000K to 6000K, subsequently <u>rose</u> in the nozzle to an exit plane value of 7000-10,000K. These tests were at fairly low pressure (a 6mm diameter constrictor was used, giving chamber pressures of 0.1 to 0.3 atm), which may explain the anomalous behavior.

In terms of modeling, accounting for vibrational lag is relatively straightforward, as in Ref. (29) for example, although it does involve additional computational burden. A more comprehensive approach, in which the state-specific vibrational populations are tracked separately [24,42], is, by contrast, quite demanding in the context of a 2-D computation, and, in view of the data, would not seem justified for the normal

15

operational regimes. It may, however, be needed in order to understand the effects on the free electron distribution, to which we now turn.

It is well known that molecular gases, particularly N_2, can readily absorb collisional energy from the free electrons into their vibrational modes. For N_2, this occurs mainly for electron energies from 2 to 3 eV. As a result, for values of the field/density (E/N) ratio high enough that significant population of electrons would exist above these energy levels in atomic gases, very few actually exist in a molecular gas. The distribution "dams up" against the effective barrier represented by the vibrationally active region of the energy spectrum, and it greatly departs from the Maxwellian shape. Typical results by Nighan [43] are shown in Fig. 14. For reference, Fig. 15 shows calculated E/N in the anodic bridge region of a H_2 arcjet, using the model of Refs. (20,31).

For N_2, if $E/N \leq 5 \times 10^{16} Vcm^2$, there develops a substantial depletion of high energy electrons. If this persists all the way to the ionizing range (13-16 eV), the ionization rate calculation would be substantially affected. In this connection, it must be noted that for each E/N, the results of Nighan appear to indicate that the distribution actually
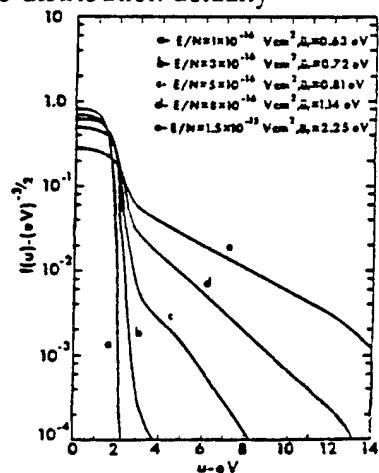
Fig. 14: Electron energy distribution functions in N2 for various E/N values. The distribution function is defined such that

$\int_0^\infty u^{1/2} f(u) du = 1$ and the reduced average energy such that $\bar{u}_r = \frac{2}{3} \int_0^\infty u^{3/2} f(u) du.$ (Ref. 43)
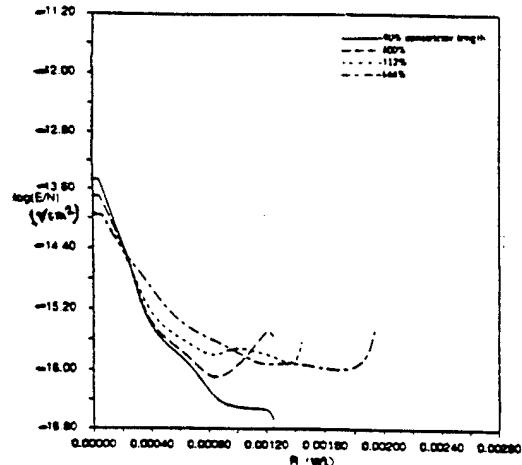
Fig. 15: Radial Profiles of E/N ($V\, cm^2$) for conditions of Ref. 21
(0.1 g/s, 60 A) at several axial sections near the constrictor's end.

becomes super-Maxwellian at high enough electron energy; however, the reported range of f(u) (Fig. 14) is insufficient to verify where this happens for the lower E/N values. Other electron-induced rates, such as vibrational excitation and dissociation, must be also strongly affected by the distortion in f(u).

The traditional way to account for vibrational (more generally, inelastic) losses in molecular gases is to multiply the elastic losses times a factor δ, which is energy-dependent. Data on these factors were collected by Massey and Craggs [44] and are reported in Ref. (32), for example. Eq. (5.74) of Ref. 32 gives the electron temperature elevation as

$$\frac{T_e}{T_s} = 1 + \frac{\pi}{24\delta} \frac{T_s}{T_e} \frac{m_s}{m_e} \frac{e^2}{Q_{es}(T_e)} \left(\frac{E}{P}\right)^2 \quad (15)$$

We can use the Nighan results in Fig. (14) and Eq. (15) (where $P = N\, k\, T_g$) to

16

extract the effective δ value implied. We do this by equating T_e to the mean energy $\bar{u}_r$ in Fig. (14), and using known data for the elastic cross-section Q_{eg} (T_e) (Ref. 45). The value of T_g needs to be assumed, and 0.1 eV has been used here. The resulting δ is shown superimposed on the Massey-Craggs data in Fig. 16, and a very large discrepancy is readily appreciated. With Nighan's results, if $E/N \sim 10^{-16}$ Vcm^2, as in the anodic bridge region, then $T_e \sim 0.6$ eV, and a very non-maxwellian distribution results, while, using, as in Refs. (20-31), the Massey-Craggs data, we found $T_e \sim 1$-2 eV, which, back to Fig. 14, would indicate little departure from Maxwellian.
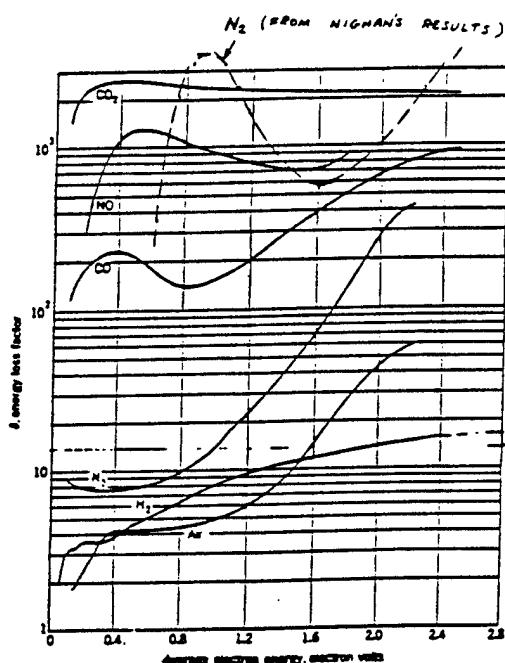

Fig. 16: Energy loss of electrons with maxwellian velocity distribution with various gases. (Data compiled by H. Massey and J.D. Craggs (44) 1959). Superimposed are calculations on δ based on results in Fig. 14 for N_2.

In view of the uncertainties, and of the strong potential implications, there is clearly a need for more detailed research in this particular area. As noted, Babu and Subramaniam [24] have initiated work in that direction.

4.4 Thermo-Mechanical Effects

The materials comprising the anode block structure of an arcjet are subject to extreme heat fluxes (1-10×10^7 w/m^2 in the attachment area), and reach temperatures that can be over 1/2 of their melting point. Thus, despite a low stress level, thermal creep effects can occur, which distort the critical constrictor region, as has been observed, for example by Butler [46], and lead to performance drift and lack of repeatability, and may also affect thruster life. Related effects can occur in cathodes at high current [47]. From the modeling point of view, these areas remain unexplored, and, given their practical importance, efforts should be made to extract as much related information as possible from heat flow models of the solid part of thrusters.

4.5 Species Segregation and Mean Free Path Effects

In an arcjet using N_2H_4 or NH_3, these heavy molecules will dissociate as they enter the arc-heated parts of the flow. The hydrogenic fragments resulting from this dissociation will diffuse much faster than the nitrogen molecules or atoms, and the result can be a hydrogen enrichment of the cooler, outer parts of the flow.

A similar segregation of hydrogen towards the periphery is also to be expected in the plume after collisionality has become very weak, simply because of the higher thermal velocity of H and H_2 compared to N and N_2 (or NH) at the same temperature.

These two effects are observed together when looking spectroscopically at the arcjet plume, yet their implications are quite distinct (segregation upstream can improve specific impulse, segregation in the plume cannot). Refined diffusional and/or Monte Carlo computations will be required to mimic these effects.

17

5. Some Numerical Issues

With so many difficult physical problems pending, arcjet modelers have not so far paid much attention to questions of numerical efficiency. The standard approach for 2-D simulations has been to combine an explicit time-marching algorithm, such as McCormack's, for the bulk flow, plus over-relaxation or other elliptic solvers for the field equations. Miller [31] found it necessary to integrate the electron continuity and energy equations and the potential equation using a separate time step, which needs to be up to 100 times shorter than that used for the heavy-particle equations. The time steps used need to satisfy the Courant-Fredrich-Levy condition (the fastest signal should travel less than one mesh size per time step). In a very inhomogeneous situation, such as an arcjet, the fastest velocities and speeds of sound, which occur in the hotter parts of the nozzle flow, dictate this choice of time step, with the result that the slow inlet region is enormously over-calculated. Combining these inefficiencies with the abundance of exponentials and other computationally costly calculations required per step, the most advanced codes are at present pushing against the frontiers of what is practical in terms of computation costs.

It seems clear, therefore, that the time has come to begin refining the computational procedures, if we want to continue enriching the codes with additional effects, species and, especially, dimensions. This is definitely beyond this writer's expertise, but a few indications as to improvements to be sought will be ventured anyway:

(a) Simplify and pre-tabulate as many of the transport and rate coefficients as possible.

(b) Try to incorporate inhomogeneous time step procedures, if only the steady state is of interest.

(c) Use variations of the unstructured grid algorithms, now being developed for CFD applications.

(d) Investigate the use of quasi-equilibrium for the fastest evolving effects, such as electron temperature balance.

6. Summary

Numerical modeling of arcjet thrusters is reaching an acceptable level of performance prediction capacity, predicated, however, n judicious admixing of empirical information on a number of poorly understood physical issues. Prominent among these are the physics of anodic attachment (including stability and potential filamentation), and the interactions of free electrons with the molecular gas. Further progress will necessarily have to include clarification of these areas, plus gradual expansion of the ability to handle the very complex numerical task while staying financially solvent. The time appears at hand when theoretical modeling can emerge from the shadow of empiricism and become a co-equal driver with selective testing in the quest for improved design of future thrusters.

REFERENCES

[1] Pfender, E. "Electric Arcs and Arc Gas Heaters". In Gaseous Electronics, Vol. I, ed. by M.N. Hirsch and H.J. Oskam. Acad. Press, 1978.

[2] Jack, J.R. "Theoretical Performance of Propellants Suitable for Electrothermal Jet Engines". ARS J. vol. 31, p. 1685, 1961.

[3] John, R.R., Benett, S., Coss, L.A., Chen, M.M. and Connors, J.F., "Energy Addition and Loss Mechanisms in the Thermal Arcjet Engine". AIAA 63-022. AIAA Electric Propulsion Conference, Colorado Springs, CO, 1963.

[4] Weber, H.E. "Growth of an Arc Column in Flow and Pressure Fields". AGARD o Graph 84, Sept. 1964, pp. 845-887.

[5] Topham, D.R. "The Electric Arc in a Constant Pressure Axial Gas Flow", J. Physics D. Applied Physics, 1971, Vol. 14. Also, the "Characteristics of Axial Flow Electric Arcs Subject to Pressure Gradients". Loc. Cit., Vol. 5, 1972.

[6] Glocker, B., Schrade, H.O., and Sleziona, C., "Numerical Prediction of Arcjet Performance", AIAA 90-2612, 21st International Electric Propulsion Conference, Orlando, 1990.

[7] Glocker, B.. Schrade, H.O., and Auweter-Kurtz, M., "Performance Calculation of Arcjet Thrusters - The Three Channel Model". IEPC 93-187. 23rd International Conference on Electric Propulsion, Seattle, 1993.

[8] Martinez-Sanchez, M., and Sakamoto, A., "Simplified Analysis of Arcjet Thrusters", AIAA 93-1904. 29th Joint Propulsion Conference, Monterey, June 1993.

[9] Tahara, H., Uda, N., Onoe, K., Tsubakishita, Y. and Yoshikawa, T., "Optical Measurement and Numerical Analysis of Medium-Power Arcjet Nonequilibrium Flowfields". IEPC 93-133, 23rd Intnl. Conf. on Electric Propulsion, Seattle, 1993.

[10] Glocker, B., Rossgen, Th. and Laxander, A., "Medium Power Arcjet Analysis and Experiments", IETC 91-016, 22nd International Electric Propulsion Conference, Viareggio, Italy, 1991.

[11] Watson, V.R. and Pegot, E.B., "Numerical Calculations for the Characteristics of a Gas Flowing Axially through a Cosntricted Arc", NASA TN D-4042, June 1967.

[12] Andrennucci, M. et al, "Development of a Computer Programme for the Analysis of Arcjet Nozzles", IEPC 91-113, 22nd International Electric Propulsion Conference, Viareggio, Italy, 1991.

[13] Butler, G.W., Kashiwa, B.A. and King, D.Q, "Numerical Modeling of Arcjet Performance", AIAA 90-1472, 21st Fluid Dynamics, Plasma Dynamics and Lasers Conference, Seattle, June 1990.

[14] Butler, G.W. and King, D.Q., "Single and Two-Fluid Simulations of Arcjet Performance", AIAA 92-3104, 28th Joint Propulsion Conference, Nashville, 1992.

[15] M.A. Capelli, J.G. Liebeskind, R.K. Hanson, G.W. Butler and D.Q. King, "A Direct Comparison of Hydrogen Arcjet Thruster Properties to Model Predictions". IEPC 93-220, 23rd Intnl. Conf. on Electric Propulsion, Seattle, 1993.

[16] Rhodes, R. and Keefer, D., "Numerical Modeling of an Arcjet Thruster", AIAA 90-2614, 21st International Electric Propulsion Conference, Orlando, 1990.

[16] Rhodes, R. and Keefer, D., "Comparison of Model Calculations with Experimental Data from Hydrogen Arcjets". IEPC 91-111, 22nd International Electric Propulsion Conference, Viareggio, Italy, 1991.

[17] K. Fujita and Y. Arakawa, "Anode Heat Loss and Current Distributions in DC Arcjets", IEPC 93-185, 23rd Intnl. Conf. on Electric Propulsion, Seattle, 1993.

[18] Andrennucci, M., D'Agostino, L. and Ciucci, A., "Development of a Numerical Model of the Nozzle Flow in Low Power Arcjet Thrusters", IEPC 93-182, 23rd International Conf. on Electric Propulsion, Seattle, 1993.

[19] Okamoto, H. and Nishida, M., "Numerical Simulation of the Performance of a Radiation-Cooled 1KW DC Arcjet Thruster". IEPC 93-181, 23rd International Conf. on Electric Propulsion, Seattle, 1993.

[20] Miller, S.A. and Martinez-Sanchez, M., "Multifluid, Non-Equilibrium Simulation of Arcjet Thrusters". AIAA 93-2101, 29th Joint Propulsion Conference, Monterey 1993. Also to appear in the J. of Propulsion /Power.

19

Also, Miller, S.A. and Martinez-Sanchez, M., "Nonequilibrium Numerical Simulation of Radiation-Cooled Arcjet Thrusters". IEPC 93-218, 23rd International Conference on Electric Propulsion, Seattle, 1993.

[21]   Glocker, B., Auweter-Kurtz, M., Goeltz, T.M., Kurtz, H.L. and Schrade, H.O., "Medium Power Arcjet Thruster Experiments". AIAA 90-2531. 21st International Electric Propulsion Conference, Orlando, FL, 1990.

[22]   H. Krier, R. Burton and T. Megli, "Two-Temperature Modeling of N_2/H_2 Bipropellant Arcjets", this meeting.

[23]   Rhodes, R. and Keefer, D., "Non-Equilibrium Modeling of Hydrogen Arcjet Thrusters". IEPC 93-217, 23rd International Conf. on Electric Propulsion, Seattle, 1993.

[24]   Babu, V. and Subramaniam, V., "2-D Axisymmetric Flow in Arcjets with Strong Vibrational Non-Equilibrium". IEPC 93-129, 23rd Intnl. Conf. on Electric Propulsion, Seattle, 1993.

[25]   J.G. Liebeskind, R.K, Hanson, and M.A., Cappelli, , "Plume Characteristics of an Arcjet Thruster", AIAA 93-2830, 29th Joint Propulsion Conference, Montery, 1993.

[26]   J.G. Liebeskind, R.K. Hanson and M.A. Cappelli, "LIF Measurements of Species Velocity in an Arcjet Plume", IEPC 93-131, 23rd Intnl. Conf. on Electric Propulsion, Seattle, 1993.

[27]   I.D. Boyd, M.A. Capelli and D.R. Beattie, "Monte Carlo and Experimental Studies of Nozzle Flow in Low Power Hydrogen ARcjet", AIAA 93-25-29, Monterey, July 1993.

[28]   I.D. Boyd, D.R. Beattie and M. Capelli, "Chamber Effects on Plume Expansion for a Low Power Hydrogen Arcjet", IEPC 93-126, 23rd Intnl. Conf. on Electric Propulsion, Seattle, 1993.

[29]   Fasoulas, S., Auweter-Kurtz, M., Habiger, H.A., Laure, S.H. and Sleziona, P.C., "Investigation of a Nitrogen Flow within a Plasma Wind Tunnel", AIAA 93-2817, 28th Thermophysics Conference, Orlando, FL, 1993.

[30]   A.E. Guile, IEEE Review, Vol. 118, p. 1131. Also A.E. Guile and B. Jütner, IEEE Trans. on Plasma Sc., Vol. PS-8, No. 3, Sep. 1980, pp. 259-268.

[31]   S.A. Miller, "Multifluid Nonequilibrium Simulations of Arcjet Thrusters. Doctor of Science Thesis, MIT, Feb. 1994.

[32]   G.W. Sutton and A. Sherman, "Engineering Magnetohydrodynamics", Fig. 5.6, p. 148. McGraw-Hill Book Co., 1965.

[33]   H. H. Maecker, "Principles of Arc Motion and Displacement", Proc. IIII, Vol. 59, no. 4, April 1971, 439-449.

[34]   T. Yamada, K. Toki and K. Kuriki, "Behavior of Arc Column in Arcjet Constrictor". IEPC 93-184, 23rd Intrnl. Conf. on Electric Propulsion, Seattle, 1993.

[35]   W.J. Harris, E.A. O'Hair, L.L. Hatfield, M. Kristiansen and J.S. Mankins, "Anode Motion in High Power Arcjets". AIAA 92-3838, 28th Joint Propulsion Conference, Nashville, 1992.

[36]   D. Berns, J. Sankovic and C. Sarmiento, "Investigation of a Subsonic-Arc-Attachment Thruster Using Segmented Anodes". AIAA 93-1899, 29th Joint Propulsion Conference, Monterey, 1993.

[37]   J.P. Todd and R.E. Sheets, "Development of a Regeneratively Cooled 30 KW Arcjet Engine", AIAA Jl., Vol. 3, No. 1, pp. 122-126, 1965.

[38]   D.M. Zube and R.M. Myers, "Nonequilibrium in a Low Power Arcjet Nozzle", AIAA 91-2113, 27th Joint Propulsion Conference, Sacramento, 1991.

[39] D.M. Zube and M. Auweter-Kurtz, "Spectroscopic Arcjet Diagnostic Under Thermal Equilibrium and Nonequilibrium Conditions", AIAA 93-1792. 29th Joint Propulsion Conference, Monterey, 1993.

(40) C. Park "Hydrogen Line Ratios as Electron Temperature Indicators in Non-Equilibrium Plasma". J. of Quant. Spectroscopy and Transfer, Vol. 12, p. 323 (1972).

(41) W.A. Hoskins, D.Q. King and G.W. Butler "Measurement of Population and Temperature Profiles in an Arcjet Plume" AIAA 92-3240, 28th Joint Propulsion Conf., Nashville, 1992.

(42) D.A. Gonzales and P.L. Varghese "Master Equation Calculations of Vibrational Non-Equilibrium and Dissociation Kinetics:. IUTAM Symp., Marseille, France, Sept. 1992.

(43) W.L. Nighan, "Electron Energy Distributions and Collision Rates in Electrically Excited N_2, CO and CO_2" Phys. Rev. A., Vol. 2, No. 5, Nov. 1970, pp. 1989-2000.

(44) H. Massey and J.D. Craggs, Hanbuch der Physik, 371. pp. 314-415, 1959.

(45) M. Mitchner and Ch. H. Kruger, Jr., Partially Ionized Gases, Wiley-Interscience, 1973 (Fig. 27, page 107).

(46) G.W. Butler, private communication (1993).

(47) M. Auweter-Kurtz, B. Glocker, H.L. Kurtz, O. Loessener, H.O. Schrade, N. Turbanos, T. Wegmann and D. Willer, "Cathode Phenomena in Plasma Thrusters". Jl. of Propulsion and Power, Vol. 9, No. 56, Nov-Dec. 1993, pp. 882-888.

Quantity	Computational (Experimental)			
$\dot{m}(g/sec)$	0.1	0.1	0.3	0.3
I (A)	50	150	50	150
P_0 (N/m^2)	9.02×10^4 (9.00×10^4)	1.23×10^5 (1.30×10^5)	2.03×10^5 (2.35×10^5)	2.44×10^5 (2.74×10^5)
V (V)	165 (165)	155 (140)	225 (233)	199 (198)
Thrust F (N)	0.58 (0.60)	0.81 (0.83)	1.32 (1.17)	1.63 (1.62)
η	0.204 (0.218)	0.141 (0.164)	0.258 (0.196)	0.148 (0.147)
Q_{LOSS} (KW)	1.40 (1.30)	4.20 (4.00)	1.40 (1.00)	4.20 (3.30)

Table 1. Comparison of 1-D model [8] to data [10]for a 20 KW water-cooled H2 arcjet. A uniform anode drop of $\Delta V_a = 28V$. has been added to the calculated column voltage.
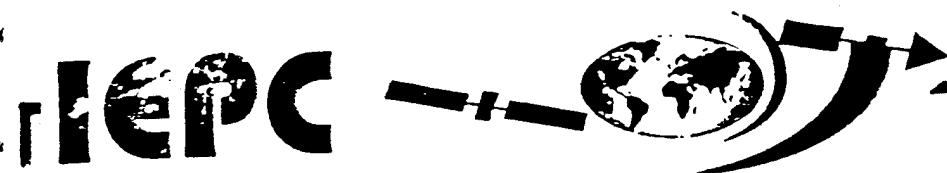
Nonequilibrium Numerical Simulation of Radiation-Cooled Arcjet Thrusters

S. Miller and M. Martinez-Sanchez
Space Power and Propulsion Laboratory
Massachusetts Institute of Technology
Cambridge, MA

NONEQUILIBRIUM NUMERICAL SIMULATION OF RADIATION-COOLED ARCJET THRUSTERS

S.A. Miller*and M. Martinez-Sanchez [†]
Space Power and Propulsion Laboratory
Dept. of Aeronautics and Astronautics, MIT, Cambridge, MA 02139

Abstract

A detailed numerical model has been developed to study the gasdynamic flow in an electrothermal arcjet thruster. This two-temperature, Navier-Stokes model consistently incorporates viscosity, heat conduction, ohmic dissipation, collisional energy transfer between electrons and heavy species, ambipolar diffusion, nonequilibrium dissociation and ionization, and radiation. The fluid equations are solved by MacCormack's method, while an iterative procedure is used to relax an electric potential equation, from which the current distribution in the thruster is obtained. Converged solutions are compared with experimental results from the German TT1 radiatively-cooled arcjet thruster with hydrogen propellant. Results are presented for a baseline case which reveal the two-dimensional, two-fluid nature of the interior flow, especially in terms of the distribution and anode attachment of the electric current and the growth and development of the arc region. Calculated discharge voltage is within a few percent of experimental measurements, and predicted specific impulse is within 5-10% agreement over a range of operating parameters. The effects of a coupled anode heat balance model on the predicted anode wall temperature, inlet gas temperature, and overall thruster performance are also discussed.

Nomenclature

$\hat{c}_v$ Specific heat at constant volume $[J/mole/°K]$
D_a Ambipolar diffusion coefficient $[m^2/s]$
d_{er} Ambipolar flux of ions and electrons $[1/m^2/s]$
e Electric charge $[C]$, internal energy $[J/kg]$
$\vec{E}$ Electric field $[V/m]$
E_i Ionization energy $[J]$
E_d Dissociation energy $[J]$
E_l Elastic collisional energy transfer $[W/m^3]$

E_{vib} Vibrational excitation energy $[J]$
h Planck's constant $[Js]$, enthalpy $[J/kg]$
I Total current $[A]$
$\vec{j}$ Electric current density $[A/m^2]$
k Boltzman's constant $[J/°K]$
K Equilibrium constant
m Particle mass $[kg]$
n Number density $[1/m^3]$
$\dot{n}$ Net production rate $[1/m^3/s]$
$\hat{N}$ Avogadro's number $[1/mole]$
p Scalar pressure $[Pa]$
$\vec{q}$ Heat flux vector $[W/m^2]$
R Real gas constant $[J/kg/°K]$
$\hat{R}$ Universal gas constant $[J/mole/°K]$
$\dot{R}$ Energy loss due to radiation $[W/m^3]$
T Temperature $[°K]$
$\vec{u}$ Mean flow velocity $[m/s]$
v_B Bohm velocity $[m/s]$
$\vec{V}$ Slip velocity $[m/s]$
x Mole fraction
α Ionization fraction
κ Coefficient of thermal conductivity $[W/m/°K]$
μ Coefficient of viscosity $[kg/ms]$
ν Collision frequency $[1/s]$
ϕ Electric potential $[V]$
Φ Viscous dissipation function $[W/m^3]$
ψ Electron mobility $[m^2/\Omega/C]$
ρ Mass density $[kg/m^3]$
σ Electrical conductivity $[mho/m]$
$\overline{\Omega}$ Average effective collision integral $[m^2]$

*Graduate Student, Member AIAA
†Professor, Member AIAA

1 Introduction

Low power arcjet thrusters have recently been flight qualified through ground testing and will soon be tested in space for stationkeeping of geosynchronous communication satellites. Most of the impetus for design strategies, however, has come from empirical studies and experimentation, and a need remains to better understand the underlying physics, detailed energy balances, and transport mechanisms of these devices. Unfortunately, the complexity of the models and equations needed to accurately represent the

flow in an arcjet thruster effectively limits the use of analytic techniques to simplified cases, through which one may obtain useful physical insights but inadequate predictions of thruster performance. Experimental techniques provide much useful empirical data, but many quantities of interest are not accessible in the important regions of the thrusters. For these reasons numerical methods of solving the governing equations have become an important tool for conducting arcjet research.

Previous numerical modeling of arcjet thrusters has focused on the development of 1-D, 2-D, and axisymmetric models with relatively simple physics and geometries. The level of detail has ranged from 1-D models[1] to coupled quasi-analytic models of the inner (arc) and outer (cold gas) flows[2, 3, 4], to simplified axisymmetric space-marching techniques[5], and finally to 2-D and axisymmetric viscous codes which begin to incorporate most of the detailed physical processes[6, 7, 8]. The latest research has obtained results which variously include ohmic heating, electron heat conduction, thermal and ionizational nonequilibrium, and empirical models of radiation losses. There are still a number of issues, such as viscous and diffusive effects, arc formation and attachment, the heat balance in the anode, and ultimately the accurate prediction of voltage and efficiency, which need to be addressed. This paper describes a generalized, more physically accurate model of the gasdynamic flow through an arcjet thruster, which includes the aforementioned effects and compares favorably to experimental results obtained with medium power hydrogen arcjets.

2   Model

2.1   Basic Assumptions

This model is based on an axisymmetric formulation, so that variations in flow quantities in the azimuthal direction are neglected. A component of the flow velocity in the θ-direction, however, is incorporated to account for the "swirl" injection of most experimental arcjets. The model has been developed in a general enough sense so that any monatomic or diatomic propellant may be simulated. For the purpose of this research hydrogen was selected as the propellant of choice, due to its low molecular weight (and therefore high performance) and its simple molecular structure, which allows for analytic evaluation of the necessary transport coefficients. Nonequilibrium dissociation and ionization are modeled, and four species of particles are tracked: diatomic molecules, monatomic neutrals and ions, and electrons. Dissociation is modeled by heavy species collisions and by electron impact, and the ionization process is based on electron impact ionization and three-body recombination, with only H^+ ions considered.

The following assumptions are made regarding the state of the flow in the thruster and the physical processes involved. The plasma produced by ionizing electron collisions is assumed to be macroscopically neutral, so that $n_e = n_i$. Strong coupling is assumed between the ions and neutrals, designated together as the heavy species. This implies that $\bar{u}_i \cong \bar{u}_n \cong \bar{u}$ (except for ambipolar diffusion), and $T_i \cong T_n \cong T_g$. Effects which are consistently incorporated include ambipolar diffusion, heat conduction, viscous shear and dissipation, ohmic heating, collisional energy transfer between electrons and heavy species, and energy lost through radiation. The self-induced magnetic field of the ionized gas is neglected due to the low current density in the thruster, and the individual species are assumed to obey the ideal gas law. Given the aforementioned assumptions, the model can be summarized by a set of nine partial differential equations which must be solved locally in order to generate a viable simulation of the flow in an arcjet thruster.

2.2   Governing Equations

The set of equations which govern the flow in the model arcjet thruster of this research is essentially a group of modified Navier-Stokes equations. These include an equation of state and equations for the ion, neutral atom, and global density; the axial, radial, and azimuthal global momentum; the electron and heavy species energy; and the electric potential. In order to maintain numerical robustness, these equations are written in as conservative a manner as possible, particularly with respect to the $\frac{1}{r}$ terms which appear due to the axisymmetry of the problem.

The electric potential equation is derived by combining Ohm's law, $\vec{j} = \sigma \vec{E} + \psi \nabla p_e$, with the equation $\nabla \cdot \vec{j} = 0$, where $\psi = \frac{e}{m_e \sum_r \nu_{er}}$ is the electron mobility. Assuming a potential of the form $\vec{E} = -\nabla \phi$, the resulting equation is given by

$$\frac{1}{r}\frac{\partial}{\partial r}\left(r\sigma\frac{\partial\phi}{\partial r}\right) + \frac{\partial}{\partial z}\left(\sigma\frac{\partial\phi}{\partial z}\right)$$

$$= \psi\left(\frac{\partial^2 p_e}{\partial r^2} + \frac{1}{r}\frac{\partial p_e}{\partial r} + \frac{\partial^2 p_e}{\partial z^2}\right) + \frac{\partial p_e}{\partial r}\frac{\partial\psi}{\partial r} + \frac{\partial p_e}{\partial z}\frac{\partial\psi}{\partial z}.$$
$$(1)$$

The current density may then be extracted by solving

$$j_r = \psi\frac{\partial p_e}{\partial r} - \sigma\frac{\partial\phi}{\partial r} \quad and \quad j_z = \psi\frac{\partial p_e}{\partial z} - \sigma\frac{\partial\phi}{\partial z}. \quad (2)$$

2

The global density equation is obtained by summing the individual species continuity equations:

$$\frac{\partial \rho r}{\partial t} + \frac{\partial \rho u_r r}{\partial r} + \frac{\partial \rho u_z r}{\partial z} = 0. \tag{3}$$

For the ion (or electron) density, the governing equation is derived from the statement of ion mass conservation, modified to account for the ambipolar flux of charged particles in terms of ion density gradients:

$$\frac{\partial \rho_e r}{\partial t} + \frac{\partial (\rho_e u_r + d_{er}) r}{\partial r} + \frac{\partial (\rho_e u_z + d_{ez}) r}{\partial z} = m_e \dot{n}_e r, \tag{4}$$

where $\vec{d}_e$ is the ambipolar flux, given by

$$\vec{d}_e = -D_a \nabla \rho_e; \qquad D_a = \sqrt{\frac{\pi k T_g}{4 m_n}} \frac{\left(1 + \frac{T_e}{T_g}\right)}{Q_{in}(n_e + n_n)}. \tag{5}$$

Here the source term $\dot{n}_e$ represents the net rate of production of ions per unit volume through inelastic collisional processes. The statement of atomic hydrogen mass conservation is obtained in a similar manner, and the effect of ambipolar diffusion is consistently included by assuming that both neutral species travel at the same velocity:

$$\frac{\partial \rho_H r}{\partial t} + \frac{\partial \rho_H u_r r}{\partial r} - \frac{\partial}{\partial r}\left(\frac{\rho_H}{(\rho_{H_2} + \rho_H)}\frac{m_H}{m_e} d_{er} r\right)$$

$$+ \frac{\partial \rho_H u_z r}{\partial z} - \frac{\partial}{\partial z}\left(\frac{\rho_H}{(\rho_{H_2} + \rho_H)}\frac{m_H}{m_e} d_{ez} r\right)$$

$$= m_H \left(\dot{n}_H + <\sigma v> n_e n_{H_2} - \dot{n}_e\right) r. \tag{6}$$

In this equation the source term represents the net rate of production of neutral atoms, given by the difference between the net rate of production due to dissociation and the net rate of ionization of those neutral atoms produced.

The three global momentum equations are

$$\frac{\partial \rho u_r r}{\partial t} + \frac{\partial (\rho u_r^2 + p - \tau_{rr}) r}{\partial r} + \frac{\partial (\rho u_r u_z - \tau_{rz}) r}{\partial z}$$

$$+ \tau_{\theta\theta} - \rho u_\theta^2 - p = 0, \tag{7}$$

$$\frac{\partial \rho u_\theta r}{\partial t} + \frac{\partial (\rho u_r u_\theta - \tau_{r\theta}) r}{\partial r} + \frac{\partial (\rho u_\theta u_z - \tau_{\theta z}) r}{\partial z}$$

$$+ \rho u_r u_\theta = 0, \quad and \tag{8}$$

$$\frac{\partial \rho u_z r}{\partial t} + \frac{\partial (\rho u_r u_z - \tau_{rz}) r}{\partial r} + \frac{\partial (\rho u_z^2 + p - \tau_{zz}) r}{\partial z} = 0, \tag{9}$$

where the corresponding τ_{ij} are the viscous stress tensor components in axisymmetric coordinates.

The heavy species energy equation is

$$\frac{\partial \rho e_g r}{\partial t} + \frac{\partial (\rho e_g u_r + q_{gr}) r}{\partial r} + \frac{\partial (\rho e_g u_z + q_{gz}) r}{\partial z}$$

$$+ \frac{\partial (\rho_{H_2} e_{H_2} V_{H_2 r} + \rho_H e_H V_{H r} + \rho_{H^+} e_{H^+} V_{H^+ r}) r}{\partial r}$$

$$+ p_{H_2}\frac{\partial V_{H_2 r} r}{\partial r} + p_H \frac{\partial V_{H r} r}{\partial r} + p_{H^+}\frac{\partial V_{H^+ r} r}{\partial r}$$

$$+ p_g \left(\frac{\partial u_r r}{\partial r} + \frac{\partial u_z r}{\partial z}\right) = \left(\Phi + E_l - \frac{1}{2}E_d \dot{n}_H\right) r, \tag{10}$$

where the internal energy and enthalpy are defined by

$$\rho e_g = \frac{3}{2}(\rho_H + \rho_{H^+}) R_H T_g + \frac{5}{2}\rho_{H_2} R_{H_2} T_g$$

$$+ \frac{\rho_{H_2} R_{H_2} \theta_v}{e^{\frac{\theta_v}{T_g}} - 1} - \frac{7}{4}\rho R_H T_f \tag{11}$$

and

$$\rho h_g = \rho e_g + \rho_{H_2} R_{H_2} T_g + (\rho_H + \rho_{H^+}) R_H T_g. \tag{12}$$

Additional flux terms have been included in the radial direction to account for the radial transport of energy by ambipolar diffusion. The heat flux vectors in Eqn. 10 can be expressed as

$$q_{gr} = -k_g \frac{\partial T_g}{\partial r} \quad and \quad q_{gz} = -k_g \frac{\partial T_g}{\partial z}, \tag{13}$$

while the viscous dissipation function is given by

$$\Phi = \mu_g \left[2\left(\frac{\partial u_r}{\partial r}\right)^2 + 2\left(\frac{\partial u_z}{\partial z}\right)^2 + 2\left(\frac{u_r}{r}\right)^2\right.$$

$$+ \left(\frac{\partial u_r}{\partial z} + \frac{\partial u_z}{\partial r}\right)^2 + \left(\frac{\partial u_\theta}{\partial r} - \frac{u_\theta}{r}\right)^2 + \left(\frac{\partial u_\theta}{\partial z}\right)^2$$

$$\left. - \frac{2}{3}\left(\frac{\partial u_r}{\partial r} + \frac{\partial u_z}{\partial z} + \frac{u_r}{r}\right)^2\right]. \tag{14}$$

Collisional energy transfer between electrons and heavy species is represented by the following expression:

$$E_l = 3\frac{\rho_e}{m_H}(\nu_{eH^+} + \nu_{eH} + \delta_s \nu_{eH_2})k(T_e - T_g). \tag{15}$$

The coefficient δ_s in Eqn. 15 is necessary to correct for the fact that electron-H_2 collisions are inelastic in nature.

For electrons, the governing energy equation is:

$$\frac{\partial \rho_e E_e r}{\partial t} + \frac{\partial (\rho_e u_{er} H_e + q_{er}) r}{\partial r} + \frac{\partial (\rho_e u_{ez} H_e + q_{ez}) r}{\partial z}$$

$$= \left(\frac{j^2}{\sigma} - E_l - E_d <\sigma v> n_e n_{H_2} - E_i \dot{n}_e - \dot{R}\right) r. \tag{16}$$

Here $\frac{i^2}{\sigma}$ represents heating due to ohmic dissipation, $\dot{R}$ is the continuum radiative loss, and the total energy and enthalpy are given by

$$E_e = \frac{3}{2}R_e T_e + \frac{1}{2}u_e^2 \qquad (17)$$

and

$$H_e = E_e + R_e T_e. \qquad (18)$$

The required electron velocities are extracted from the local current density.

The final equation required for closure of the set is the equation of state:

$$p = \sum_j p_j = \sum_j n_{gj}kT_g + n_e kT_e. \qquad (19)$$

2.3 Dissociation and Ionization

The nonequilibrium dissociation rate $\dot{n}_H$ is derived by following the procedure and nomenclature of Biasca[9] for collisions of heavy species. Accordingly, this rate is given by

$$\dot{n}_H = A\hat{N}T_g^n \exp\left(-\frac{B}{RT_g}\right)(\hat{m}_H \sigma_H + \hat{m}_{H_2}\sigma_{H_2})$$
$$\times \left[\sigma_{H_2} - \frac{\hat{R}T_g}{K_p(T_g)}\sigma_H^2\right], \qquad (20)$$

where $\hat{N}$ is Avogadro's number, K_p is the equilibrium constant in terms of partial pressures, the σ_js are the species molar concentrations, and the appropriate constants for hydrogen are listed in Table 1[10]. Dissociation by $e - H_2$ collisions is represented by the second term on the right-hand side of Eqn. 6, where the reaction rate coefficient $< \sigma v >$ as a function of T_e is taken from Janev et al.[11].

Table 1: Constants for the Hydrogen Dissociation Rate Equation

Constant	Value
A $(m^3/mole - s)$	5.5×10^{12}
B (J/mole)	435,600
n	-1
$\hat{m}_H$	5
$\hat{m}_{H_2}$	2

For ionization, the finite production rate is given by the generalized model of ionization and three-body recombination[12] as modified by Sheppard[13]:

$$\dot{n}_e = Rn_e\left(Sn_H - n_e^2\right) \qquad (21)$$

$$S = \left(\frac{2\pi m_e kT_e}{h^2}\right)^{\frac{3}{2}} e^{-\frac{s}{kT_e}} \qquad (22)$$

$$R = 6.985 \times 10^{-42} exp\left(\frac{(ln\frac{T_e}{1000} - 4.0833)^2}{0.8179}\right) \qquad (23)$$

2.4 Transport Properties

Because of the multi-component nature of the gas in an electrothermal arcjet, even with hydrogen as a propellant, the equations for the transport properties become quite complex. Since data are more readily available for hydrogen in the form of collision integrals, a formulation of the transport coefficients based on these integrals rather than on collision cross-sections is implemented. As an example of the form of the transport coefficients used in this model, the gas coefficient of viscosity is given by Eqn. 24. It is calculated based on a mean free path mixture formula, which is a function of the collision integrals and the species number densities and pure viscosities[12]:

$$\mu_g = \frac{n_{H_2}\mu_{H_2}}{n_{H_2} + n_H\sqrt{\frac{2}{3}\frac{\bar{\Omega}_{H_2-H}^{(2,2)}}{\bar{\Omega}_{H_2-H_2}^{(2,2)}}}}$$
$$+\frac{n_H\mu_H}{n_H + n_{H_2}\sqrt{\frac{4}{3}\frac{\bar{\Omega}_{H_2-H}^{(2,2)}}{\bar{\Omega}_{H-H}^{(2,2)}}} + 2n_{H+}\frac{\bar{\Omega}_{H-H+}^{(2,2)}}{\bar{\Omega}_{H-H}^{(2,2)}}}$$
$$+\frac{n_{H+}\mu_{H+}}{n_{H+} + 2n_H\frac{\bar{\Omega}_{H-H+}^{(2,2)}}{\bar{\Omega}_{H+-H+}^{(2,2)}}}, \qquad (24)$$

where the pure viscosities are given to lowest order by

$$\mu_j = 2.6693 \times 10^{-26}\frac{(M_j T_g)^{\frac{1}{2}}}{\bar{\Omega}_{jj}^{(2,2)}}. \qquad (25)$$

Electron and heavy species thermal conductivity coefficients are calculated based on similar mean free path arguments and mixture rules, and the electrical conductivity is taken from a first order approximation by Grier[14]. Collision integrals required in the calculation of transport coefficients are interpolated as a function of temperature from data by Grier[14], Belov[15], and Vanderslice et al.[16]. The accuracy of the above approximate formulas for the transport coefficients was verified by comparison to previous, more detailed work for hydrogen in thermal and ionizational equilibrium.

3 Numerical Method

3.1 Integration Scheme

The governing fluid equations are numerically integrated using MacCormack's explicit node-based method, which is 2nd order accurate in time and

space. An empirical stability formula developed by MacCormack and Baldwin[17] is utilized to calculate the integration time step, which is then multiplied by a fractional coefficient to account for the effect of source terms and nonlinearities. Although MacCormack's method contains some inherent dissipation, additional numerical smoothing is required in order to damp unwanted numerical oscillations in the fluid equations. Consequently, 2nd and 4th order smoothing terms are applied to each equation as necessary. The electric potential equation, being predominantly elliptic in nature, is solved by iteration using a successive overrelaxation (SOR) technique.

Since the physical grid is nonuniform in order to closely represent the geometry of the actual arcjet being modeled, the governing equations are transformed into natural coordinates and then solved on a uniform Cartesian computational mesh. The physical grid contains 140 axial by 30 radial grid points.

3.2 Boundary Conditions

The conditions at the inlet of the computational domain are postulated to be those of a flow which has just been injected into the thruster plenum by a large number of evenly spaced jets. The flow is therefore assumed to be subsonic and parallel to the thruster walls. A fraction of the total inlet velocity, typically 30-50%, is specified as being in the azimuthal direction in order to simulate an injected swirl. The mass flow rate and total enthalpy are specified based on the particular run parameters, and the ionization fraction is set to a small value, typically 1×10^{-6}. The density is obtained from a downwind finite difference approximation of the overall continuity equation, and the inlet electron temperature is set equal to that of the next inside point. No current is allowed to pass upstream of the inlet.

The boundary conditions at the outlet of the thruster depend on whether the exit flow is subsonic or supersonic. In both cases the electron temperature is set equal to that of the next inside point, and no current may pass beyond the exit plane. If the flow is supersonic at a point on the exit plane, then the remaining quantities are extrapolated from their values at the preceding two grid points of the mesh. If the flow is subsonic, then the exit pressure is set equal to a small value representing near-vacuum conditions and the density and axial velocity are given by Riemann invariants. The remaining quantities at a subsonic outlet are then calculated as in the supersonic case.

For those boundary points lying beyond the tip of the cathode on the line of symmetry ($r = 0$), the radial and azimuthal flow velocities are set equal to zero and a zero radial gradient is imposed on the remaining quantities.

Flow boundary conditions at the thruster walls include viscous no-slip conditions for the fluid velocities and an imposed zero gradient on the electron temperature. The heavy species temperature is held constant at 1000°K upstream of the constrictor, increasing linearly to 1100°K at the constrictor exit. This profile was chosen based on experimental and numerical calculations of the anode wall temperature distribution for a reasonable operating range of the German TT1 radiatively-cooled arcjet thruster[18]. On the cathode the wall temperature is allowed to increase to a maximum of 2000°K at the tip. For the boundary condition on electron density at each electrode, a balance is postulated between the flux of ions arriving at the sheath edge by ambipolar diffusion and the flux of ions arriving at the wall by virtue of their thermal energy at the Bohm velocity (v_B):

$$D_a \frac{dn_e}{dy} = 0.61 n_e v_B, \tag{26}$$

where

$$v_B = \sqrt{\frac{k(T_e + T_g)}{m_g}}. \tag{27}$$

This boundary condition neglects the voltage drops present in the non-neutral plasma sheath. Also omitted is the dependence of the thermionic emission of electrons at the cathode on the cathode wall temperature. Application of the perpendicular overall momentum equation at the walls provides the approximate condition

$$\frac{dp}{d\hat{n}}\big|_{wall} = 0, \tag{28}$$

where inertial and viscous terms have been neglected.

The boundary condition on the wall electric potential is that there is no current perpendicular to an insulating section, and that the potential on the anode is set equal to a fixed but arbitrary voltage. For numerical reasons, anode current attachment is restricted to that portion of the outer wall downstream of the constrictor exit. On the cathode tip, a uniform axial current density is prescribed which sums to the specified total current; the potential at the cathode is then chosen so as to maintain this current level. A cathode voltage drop equal to the ionization potential plus one half of the dissociation potential of the gas is added to the calculated voltage in order to account for the model's neglect of the cathode sheath region. In addition, an anode voltage drop is subtracted from the calculated voltage in order to account for the anode sheath region. A negative potential gradient is required in this sheath in order to

5

turn back excess electrons since the extracted current is much less than the random thermal flux of electrons to the anode wall ($j_{anode} \ll \frac{1}{4}en_e\bar{c}_e$). This voltage drop is given by

$$\Delta V_a = \frac{kT_e}{e}\left[ln\left(\frac{\sqrt{m_i/m_e}}{0.61\sqrt{2\pi}}\right)\right.$$

$$\left.-ln\left(1+\frac{j}{0.61en_e\sqrt{\frac{kT_e}{m_i}}}\right)\right]. \qquad (29)$$

4   Results

4.1   Baseline Case

Results have been achieved for comparison to the German TT1 radiation-cooled arcjet thruster[18] at a number of operating points. For the baseline case of $I = 100A$ and $\dot{m} = 0.1g/s$, some results have been presented in a previous paper[19]. Table 2 compares bulk results of the simulation to experimental measurements, while Figures 1 through 9 show line and contour plots of representative quantities. There is excellent agreement in the voltage between predicted and experimental results, and good agreement (within 7%) in the thrust and specific impulse. The accuracy in voltage prediction shows that the model is accurately modeling arc growth, electrical conductivity, and current attachment given the assumptions we have made regarding electrode sheath voltage drops. The overprediction of thrust may be a result of inaccurately specified boundary conditions for the electrode temperatures and the inlet gas temperature (see Sec. 5), or it may reflect remaining deficiencies in modeling the anodic arc attachment region.

Table 2: Comparison of Predicted and Experimental Results for Baseline Case

	Predicted	Experiment
Voltage (V)	115	112
Power (kW)	11.5	11.2
Thrust (N)	1.01	0.94
Specific Impulse (s)	1030	960
Efficiency	0.442	0.395

Figure 1 shows an axial line plot of the electric potential from the cathode tip to the anode attachment zone. The near-cathode voltage drop ΔV_c is composed of a 15.8V drop assigned to the cathode sheath ($V_i + \frac{1}{2}V_d$) and an 8V drop calculated in the first few grid points downstream of the tip. The near-anode voltage drop $\Delta V_a \approx 15V$ is composed of a 22V drop captured by the simulation and a -7V drop associated with the electron-repelling sheath.

This total anode voltage drop is associated with the net deposition of energy into the anode block by heavy species heat conduction and by the impingement of current-carrying electrons. Assuming that the energy transferred per unit area is of the form

$$\dot{E}_{anode} = -k_g\frac{dT_g}{d\hat{n}} + u_{e\hat{n}}\left[\frac{5}{2}p_e + \frac{1}{2}\rho_e u_e^2 + E_i n_e\right], \qquad (30)$$

using the results of the baseline flow simulation yields an equivalent voltage of 14.5V for this deposited power, which agrees well with the ΔV_a seen in the potential profile.

Current streamlines are plotted in Figure 2. In this case, the bulk of the current attaches within the first quarter of the nozzle, with a peak just downstream of the constrictor exit. The flow becomes fully ionized along the centerline immediately downstream of the cathode tip and remains so through the first part of the nozzle expansion, beyond which there is some recombination (Figure 3). The boundary of the partially ionized region grows to approximately 50% of the channel by the constrictor exit, and this region is essentially entrained in the flow throughout the nozzle. The primary heating mechanism is ohmic dissipation, which peaks locally along the constrictor centerline and just beyond the constrictor exit near the anode. This is evidenced by the local maxima in electron temperature in these regions (Figure 4).

Within the highly ionized region of the arc in the constrictor, collisional energy transfer between electrons and heavy species raises the gas temperature to $20,000 - 30,000°K$, or nearly the same temperature as the electrons. Outside of the arc the flow remains cold, at a temperature approximately equal to the anode wall temperature. This outer flow remains essentially uncoupled from the hot core flow, as pictured in Figure 5. The flow velocity is also uncoupled, although viscous forces eventually wash out the separation in the nozzle expansion (Figure 6). Since the pressure is nearly uniform in the radial direction, rapid acceleration of the core flow occurs throughout the low pressure region of the arc in the constrictor. Once the bulk of the pressure work has been utilized in the expansion process, however, viscous forces arising from steep velocity gradients in the central core decelerate the flow significantly in the nozzle expansion. Both the inner and outer flows accelerate smoothly through sonic velocity at and just beyond the constrictor exit, and a peak Mach number of 2.86 is reached.

Simulating the current attachment at the anode realistically and self-consistently has been a major difficulty in previous arcjet simulations. The effectiveness of this model in simulating this region is

due to the incorporation of separate energy equations for the heavy species and electrons and to the use of nonequilibrium dissociation and ionization finite rate equations. Ohmic dissipation is found to be an important source of energy both inside and outside the arc (Figure 7). This leads to electron temperatures as high as $20,000°K$ in the anode attachment zone of the outer flow, much higher than the $1000 - 2000°K$ temperatures which would be calculated by a model with only one energy equation. Figure 8 illustrates this result by comparing radial profiles of the electron and heavy species temperatures at an axial location 0.25mm downstream of the constrictor exit. This elevated electron temperature then produces enough electron impact dissociation and ionization to create the necessary charge carriers for electrical conduction between the outer arc boundary and the anode. Radial ambipolar diffusion also plays a role in moving ions and electrons outward from the arc into the surrounding cooler gas flow. This process is evidenced by radial profiles of the ambipolar diffusion and net ionization terms in the electron density equation, shown in Figure 9 near the anode wall in the current attachment region.

To gain an understanding of the loss mechanisms involved in this particular arcjet thruster design, we can examine the partition of energy in the flow at the exit plane. By conservation of energy, the total power in the exiting flow for the baseline case is equal to the electrical input power minus the power lost to the walls plus the power inherent in the inlet flow, for a total of 14.58kW. Table 3 catalogs the distribution of this power in the various energy states of the exiting flow. As the table shows, in this case

Table 3: Distribution of Energy in the Exit Flow for the Baseline Case Arcjet Simulation

Energy State	Power(W)	% of Total
Axial kinetic	5720	39.2
Radial kinetic	89	0.6
Azimuthal kinetic	< 1	0.0
Ionization	2546	17.5
Dissociation	4367	30.0
Electron thermal	88	0.6
Heavy sp. thermal	1769	12.1

only 39% of the exit plane energy is in the form of useful thrust. Fully 47% of the energy is tied up in dissociation and ionization, while 13% is classified as thermal energy. In particular, the energy bound in dissociation and ionization represents a significant frozen loss.

4.2   Performance Mapping

A number of other cases have been run to evaluate the model's effectiveness in predicting arcjet performance over a range of parameters. Figure 10 shows simulation predictions of specific impulse for the TT1 thruster at three mass flow rates and over a range of applied currents. The simulated specific impulse is seen to be approximately 5-10% higher than that measured by experiment. Table 4 compares predicted and experimentally measured discharge voltage for the cases presented in Figure 10. Voltage predictions from the arcjet simulation fall from within 1-3% of experiment for the intermediate mass flow rate to within 10-15% for the high mass flow rate. The negative slope of the V-I relationship is also captured. The differences in predictive voltage accuracy between mass flow rates probably result from the boundary condition which requires the current to attach downstream of the constrictor exit. In reality this attachment point is a function of the operating conditions and may also be affected by sheath layers or instabilities not addressed by this research.

Table 4: Comparison of Discharge Voltages for the Cases in Figure 10

Case		Voltage	
I(A)	$\dot{m}$(g/s)	Numerical	Experiment
70	0.05	89	86
100	0.05	85	78
60	0.10	118	117
100	0.10	115	112
130	0.10	113	111
60	0.15	140	127
95	0.15	138	120
130	0.15	137	118

The effect of increasing specific power on arcjet performance can be examined in detail by comparing simulation results from the three $\dot{m} = 0.1$g/s cases. Predicted voltages for these cases are very similar, as are current patterns in the nozzle. Physically, the distribution of current is controlled by the behavior of current passage through the outer gas layer, which is in turn governed by the heat diffusivity in that layer. Since the heat diffusivity is essentially the same for these three cases, the current patterns and voltages are nearly identical as well. The slightly negative V-I characteristic results primarily from higher electrical conductivity in the arc core due to increasing electron temperature with increasing current (Figure 11). In addition, the arc width increases as the current is increased (Figure 12), thus decreasing the width of the outer layer. This makes it easier for current to pass through the outer layer,

so that as the current is increased the arc attaches earlier in the nozzle and the voltage is reduced.

The effects of arc widening and increasing temperature with increasing current result indirectly from the greater ohmic dissipation produced by higher current levels. This increased dissipation then causes additional heating of the electrons, as shown in the centerline plots of electron temperature in Figure 11. Higher electron temperatures cause not only increased collisional energy transfer to the heavy species, thereby elevating gas temperatures (Figure 13), but also higher finite-rate dissociation and ionization rates and increased ambipolar diffusion, which cause the ionized region of the arc core to widen. Interestingly, the electron temperature in the flow outside the main arc is little affected by variations in the applied current, as shown in Figure 14. Since the temperature increases and the arc core expands radially as the current is increased, the central region of low mass flow necessarily deepens and widens. This can be seen in Figure 15, which shows mass flux radial profiles at the constrictor exit, and in Figure 16, which tracks the mass flow fractions inside the arc as a function of axial location. The inlet pressure also increases with the applied current, rising from 1.13atm at 60A to 1.37atm at 130A. These two related effects produce increased thrust as the current is increased. The power transferred to the anode wall increases with increasing current, from 0.85kW at 60A to 1.98kW at 130A, primarily due to the increased flux of current-carrying electrons at the anode surface. The effective anode voltage drop increases only slightly, however, from 14.1V at the lower current to 15.2V at the higher current.

The effect of varying the mass flow rate on arcjet performance can be isolated to some degree by comparing the three cases in Table 4 with different mass flow rates but similar specific powers. The first, fourth, and last cases listed in that table have specific powers of 120 MJ/kg and specific impulses of 1030 seconds, plus or minus a few percent. The main difference between these cases lies in their resulting current distributions, as shown in Figure 17. Since increasing the mass flow rate increases the density, which directly decreases the heat diffusivity ($\alpha = \frac{\kappa}{\rho c_p}$), the arc becomes more constricted. This greater constriction produces higher electron and gas temperatures inside the arc and lower temperatures outside of the arc (Figure 18). Since the width of the outer layer also increases with the mass flow rate, this leads to increased convection in the current attachment region and consequently to a broader attachment zone, as shown in Figure 17. This effect then translates into a higher predicted discharge voltage.

5 Anode Thermal Model

In order to gain a more accurate estimate of the temperature of the inlet gas and of the anode wall, an anode heat balance model was constructed. Figure 19 shows a diagram of the simulated thruster assembly for the TT1 arcjet. The tungsten anode and cathode, molybdenum casing, boron nitride insulator, and propellant gas passages are all included in this heat balance model.

The governing equation in the thruster assembly is the heat flow equation,

$$-\frac{\partial}{\partial z}\left(\kappa\frac{\partial T}{\partial z}\right) - \frac{1}{r}\frac{\partial}{\partial r}\left(r\kappa\frac{\partial T}{\partial r}\right) = \frac{j^2}{\sigma}, \qquad (31)$$

where κ is the local thermal conductivity. For low to medium power arcjets, Ohmic dissipation is negligible in the anode but not insignificant in the thin cathode rod. At the rear of the thruster assembly the temperature is fixed at 300°K, while on the outer surfaces the temperature is calculated so as to solve the radiation heat balance

$$\kappa\frac{dT}{d\hat{n}} = \epsilon\sigma_{SB}T^4, \qquad (32)$$

where ϵ is the emissivity of the material and $\sigma_{SB} = 5.67\times10^{-8}\frac{W}{°K^4 m^2}$ is the Stefan-Boltzmann constant. Along the inner anode boundary, the wall heat flux from the previously described flow simulation is input, while at the cathode tip an experimentally determined heat input of 100W is assumed.

The addition of heat to the flowing propellant is essentially a 1-D problem, so the equations

$$\rho u c_p\frac{\partial T}{\partial z} = k_g\frac{\partial^2 T}{\partial r^2} \quad and \quad \rho v c_p\frac{\partial T}{\partial r} = k_g\frac{\partial^2 T}{\partial z^2} \quad (33)$$

are employed in the gas passages, the former in the axial flow section and the latter in the radial flow section. Parabolic gas temperature and velocity distributions are assumed, and the equations are integrated by a 4th order Runge-Kutta scheme from the rear of the thruster assembly to the plenum entrance.

For the case of ($\dot{m} = 0.1$g/s, I=100A), Figure 20 shows the heat flux to the anode as a function of axial distance based on the results of the flow simulation described in the previous section. The bulk of the heat is transferred by current carrying electrons, which are deposited in the first 1/3 of the nozzle in the current attachment zone. The resulting temperature distribution in the thruster assembly is pictured in Figure 21. A maximum temperature of 1550°K is reached in the current attachment region of the anode, and the temperature varies from 875°K at the cathode root to 990°K at the plenum entrance to 1080°K at the anode tip. The propellant in the

8

gas passages is heated to 825°K by conduction from the electrodes. In terms of power, 1.45kW is deposited into the anode and 0.1kW into the cathode. Of this input amount, 49% is transferred to the propellant, 34% is conducted to the backplate, and 17% is radiated to space. While beneficial recovery of one half of the anode power loss is achieved with this design, the results suggest that performance could be increased even further by adding thermal insulation near the thruster backplate to maintain a higher temperature throughout the thruster assembly.

The resulting inlet gas and electrode wall temperatures from the heat balance model were then used as new boundary conditions for the arcjet flow simulation. Figure 22 compares predicted performance using both the old and new temperature boundary conditions at a mass flow rate of 0.1g/s. While the anode model shows closer agreement with experimental results at low currents, it does worse in terms of accuracy at higher currents. For the 60A case the inlet and wall temperatures calculated by the heat balance model are 200 − 300°K less than those specified in the original simulation, so the thrust and Isp are lower. For the 100A case, the lower inlet gas temperature predicted by the heat balance model is offset by increased heating of the flow by the anode wall in the constrictor exit and current attachment regions, resulting in a slightly higher specific impulse. For the 130A case, the inlet gas temperature is still lower than originally specified (910°K), but the anode wall temperatures are much higher (1150°K at the inlet and 1250°K at the exit, peaking at 1850°K). This causes a substantially higher performance prediction. The predicted voltages for these cases with a coupled anode thermal model are slightly lower than those calculated with the previously specified boundary temperatures. This is due to preferential concentration of the anodic arc attachment in the region of elevated wall temperature. In summary, use of the coupled heat balance model results in a slightly better prediction of voltage but no significant improvement in specific impulse prediction, leaving a gap of 5-10% between predicted and experimental I_{sp}. An anode heat balance model such as the one described above, however, does have the additional potential to allow further optimization of the thruster design.

6 Conclusions

A detailed, multifluid, viscous model has been developed to simulate the nonequilibrium gasdynamic flow in an electrothermal arcjet. The model is implemented on a nonuniform mesh fixed to experimental thruster dimensions, and the equations are solved using MacCormack's method and successive over-relaxation. Numerical results are achieved for hydrogen propellant, and calculated thrust, specific impulse, and discharge voltage compare well with experimental data for the German TT1 arcjet thruster. The internal two-dimensional structure of the flow is revealed, particularly with respect to arc development and anode attachment, and the two-temperature nature of the flow is evident. In particular, the integration of a separate electron energy equation has shown that stable attachment of the arc to the anode occurs by increased local ohmic heating coupled with nonequilibrium dissociation and ionization in the flow between the arc core and the anode wall.

An anode thermal model has been developed in order to provide more realistic estimates of the inlet gas and anode wall temperatures. The model predicts a temperature maximum in the current attachment region due to local heating from current-carrying electrons. Coupling of the heat balance model to the internal flow simulation results in closer agreement with experiment at low currents but not at higher currents for a mass flow rate of 0.1g/s. While the heat balance model predicts a lower inlet gas temperature than originally specified, it also shows that the anode wall temperature is much higher than originally specified in the current attachment region for the higher current cases, resulting in higher performance predictions. In summary, use of the coupled thermal model improves voltage predictions but overpredictions in voltage and thrust of up to 10% still remain. These overpredictions are most likely tied to remaining deficiencies in the modeling of the anodic arc attachment.

Acknowledgements

References

[1] R. Spurrett and R.A. Bond, "Modelling Arcjet Thruster Performance", IEPC 91-110, AIDAA/AIAA/DGLR/JSASS 22nd International Electric Propulsion Conference, Viareggio, Italy, October 1991.

[2] B. Glocker, H.O. Schrade, and P.C. Sleziona, "Numerical Prediction of Arcjet Performance", AIAA 90-2612, AIAA/DGLR/JSASS 21st International Electric Propulsion Conference, Orlando, July 1990.

[3] B. Glocker and M. Auweter-Kurtz, "Numerical and Experimental Constrictor Flow Analysis of a 10kW Thermal Arcjet", AIAA 92-3835, AIAA/SAE/ASME/ASEE 28th Joint Propulsion Conference, Nashville, July 1992.

[4] M. Martinez-Sanchez and A. Sakamoto, "Simplified Analysis of Arcjet Thrusters", AIAA 93-1904, AIAA/ASME/SAE/ASEE 29th Joint Propulsion Conference, Monterey, June 1993.

[5] M. Andrenucci et al., "Development of a Computer Programme for the Analysis of Arcjet Nozzles", IEPC 91-113, AIDAA/AIAA/DGLR/JSASS 22nd International Electric Propulsion Conference, Viareggio, Italy, October 1991.

[6] G.W. Butler and D.Q. King, "Single and Two Fluid Simulations of Arcjet Performance", AIAA 92-3104, AIAA/SAE/ASME/ASEE 28th Joint Propulsion Conference, Nashville, July 1992.

[7] R. Rhodes and D. Keefer, "Modeling Arcjet Space Thrusters", AIAA 91-1994, AIAA/SAE/ASME/ASEE 27th Joint Propulsion Conference, Sacramento, June 1991.

[8] R. Rhodes and D. Keefer, "Comparison of Model Calculations With Experimental Data From Hydrogen Arcjets", IEPC-91-111, AIDAA/AIAA/DGLR/JSASS 22nd International Electric Propulsion Conference, Viareggio, Italy, October 1991.

[9] R.J. Biasca, Chemical Kinetics of Scramjet Propulsion, S.M. Thesis, Massachusetts Institute of Technology, September 1988.

[10] R.C. Rogers and C.J. Schexnayder Jr., "Chemical Kinetic Analysis of Hydrogen-Air Ignition and Reaction Times", NASA Technical Paper 1856, 1981.

[11] R.K. Janev, W.D. Langer, K. Evans, and D.E. Post, Elementary Processes in Hydrogen-Helium Plasmas, Springer-Verlag, New York, 1987.

[12] M. Mitchner and C. Kruger, Partially Ionized Gases, John Wiley and Sons, New York, 1973.

[13] E.J. Sheppard, Nonequilibrium Ionization in Electromagnetic Accelerators, Ph.D. Thesis, Massachusetts Institute of Technology, 1993.

[14] N.T. Grier, "Calculation of Transport Properties of Ionizing Atomic Hydrogen", NASA TN D-3186, April 1966.

[15] V.A. Belov, "Viscosity of Partially Ionized Hydrogen", High Temperature, Vol.5, 1967, p.31-6.

[16] J.T. Vanderslice, S. Weissman, E.A. Mason, and R.J. Fallon, "High-Temperature Transport Properties of Dissociating Hydrogen", Physics of Fluids, Vol.5, No.2, February 1962, p.155-64.

[17] R.W. MacCormack and B.S. Baldwin, "A Numerical Method for Solving the Navier-Stokes Equations with Application to Shock-Boundary Layer Interactions", AIAA 75-1, AIAA 13th Aerospace Sciences Meeting, Pasadena, January 1975.

[18] B. Glocker and M. Auweter-Kurtz, "Radiation Cooled Medium Power Arcjet Experiments and Thermal Analysis", AIAA 92-3834, AIAA/SAE/ASME/ASEE 28th Joint Propulsion Conference, Nashville, July 1992.

[19] S.A. Miller and M. Martinez-Sanchez, "Multifluid Nonequilibrium Simulation of Electrothermal Arcjets", AIAA 93-2101, AIAA/SAE/ASME/ASEE 29th Joint Propulsion Conference, Monterey, June 1993.
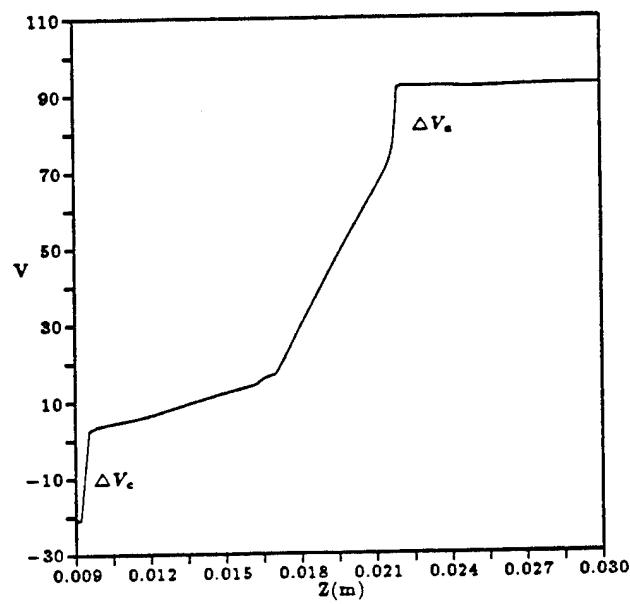
Figure 1: Electric Potential Axial Profile for the Baseline Case Arcjet Simulation
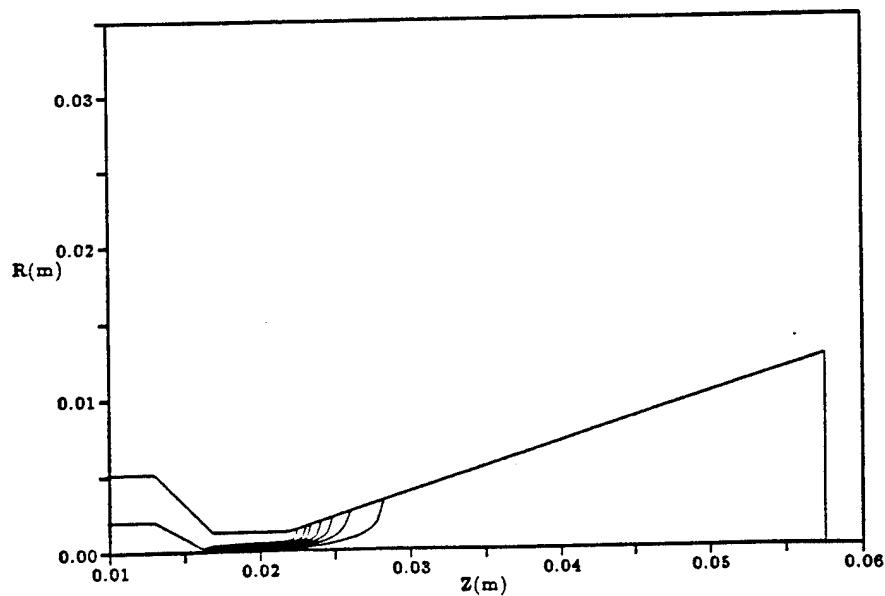
Figure 2: Enclosed Current Contours for the Baseline Case of $I = 100A$, $\dot{m} = 0.1g/s$
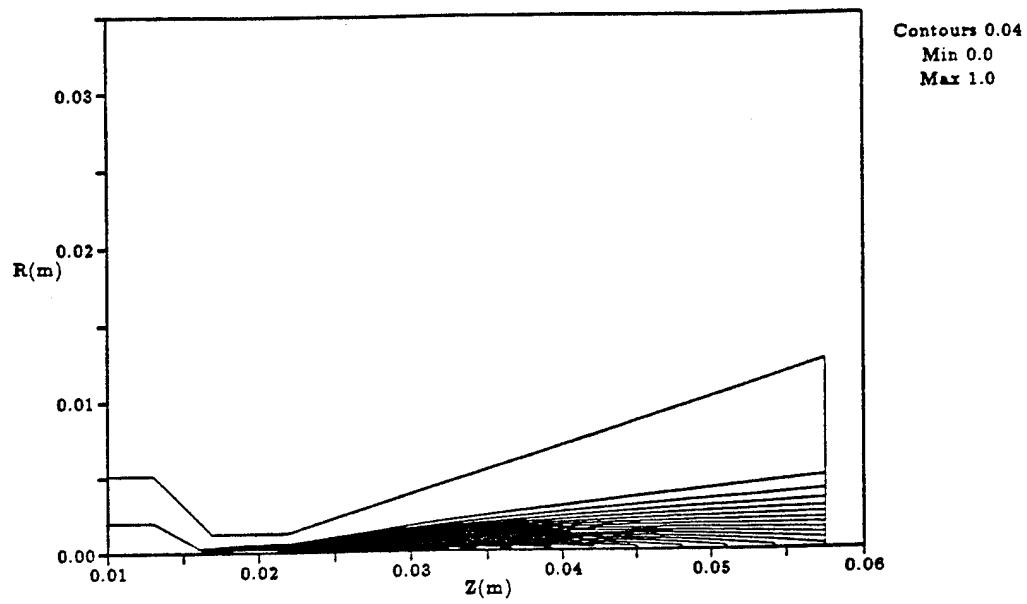
Figure 3: Ionization Fraction Contours for the Baseline Case of $I = 100A$, $\dot{m} = 0.1g/s$
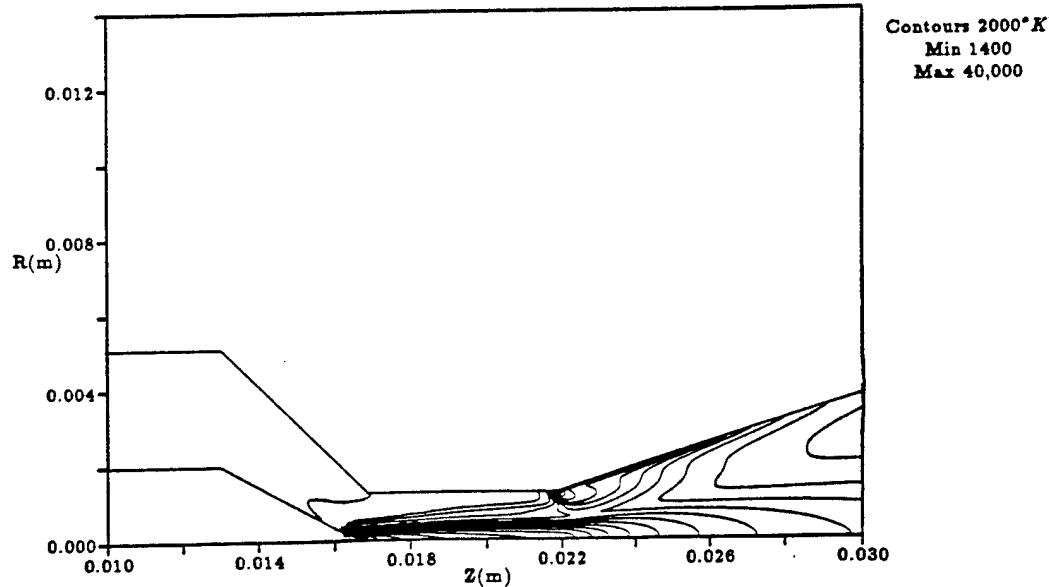

Figure 4: Electron Temperature Contours for the Baseline Case of $I = 100A$, $\dot{m} = 0.1g/s$
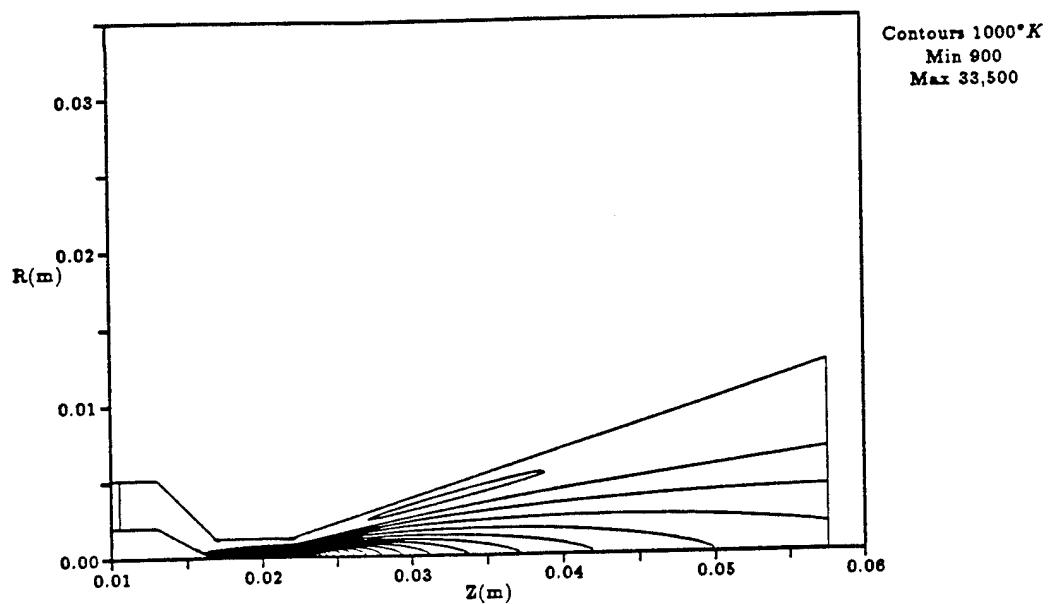
Figure 5: Gas Temperature Contours for the Baseline Case of $I = 100A$, $\dot{m} = 0.1g/s$
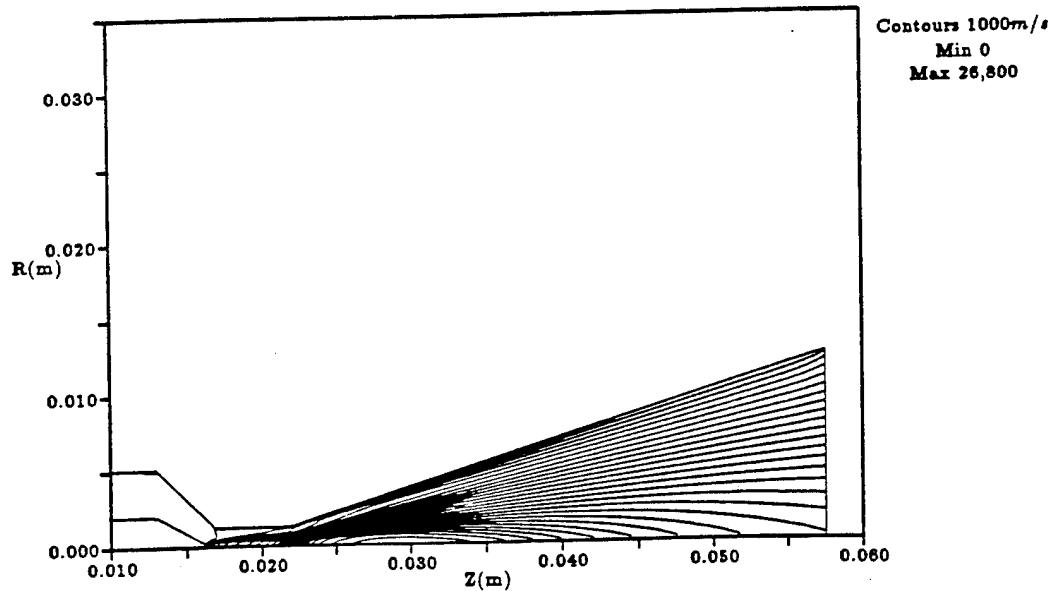
Figure 6: Axial Velocity Contours for the Baseline Case of $I = 100A$, $\dot{m} = 0.1g/s$

13

Figure 7: Radial Profiles of Some Terms in the Electron Energy Equation in the Current Attachment Region Just Beyond the Constrictor Exit

Figure 8: Radial Profiles of Electron and Heavy Species Temperatures 0.25mm Downstream of the Constrictor Exit
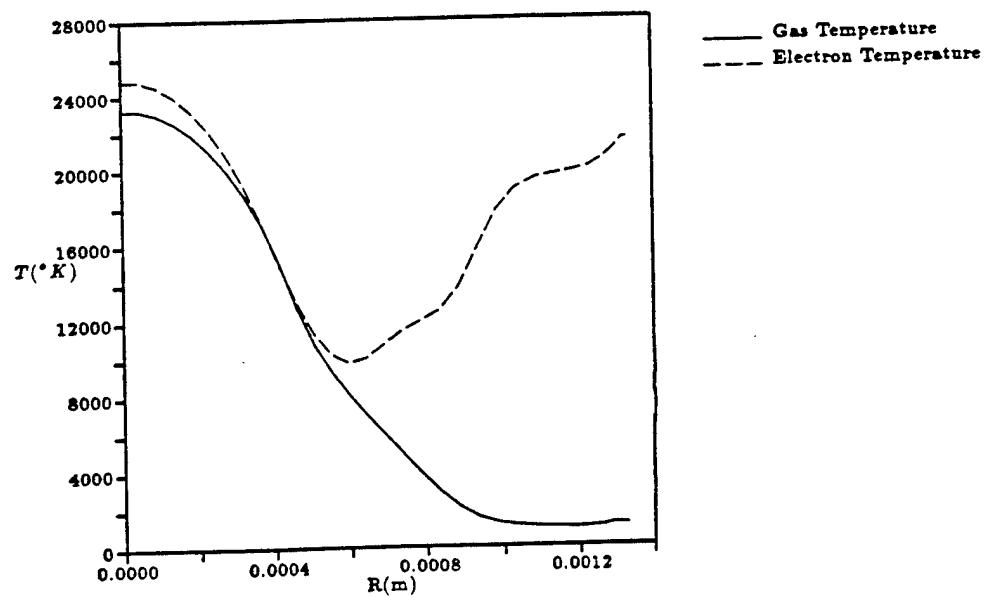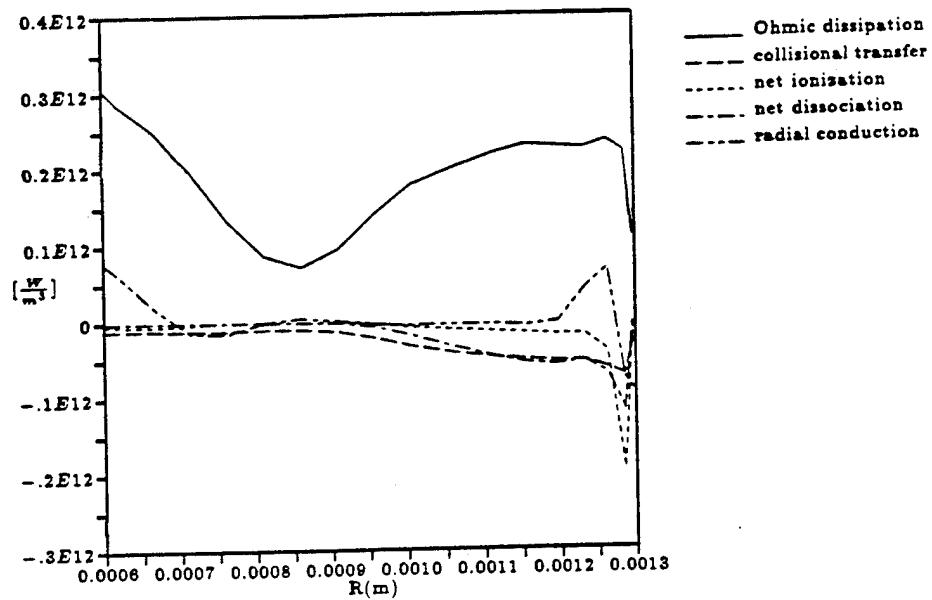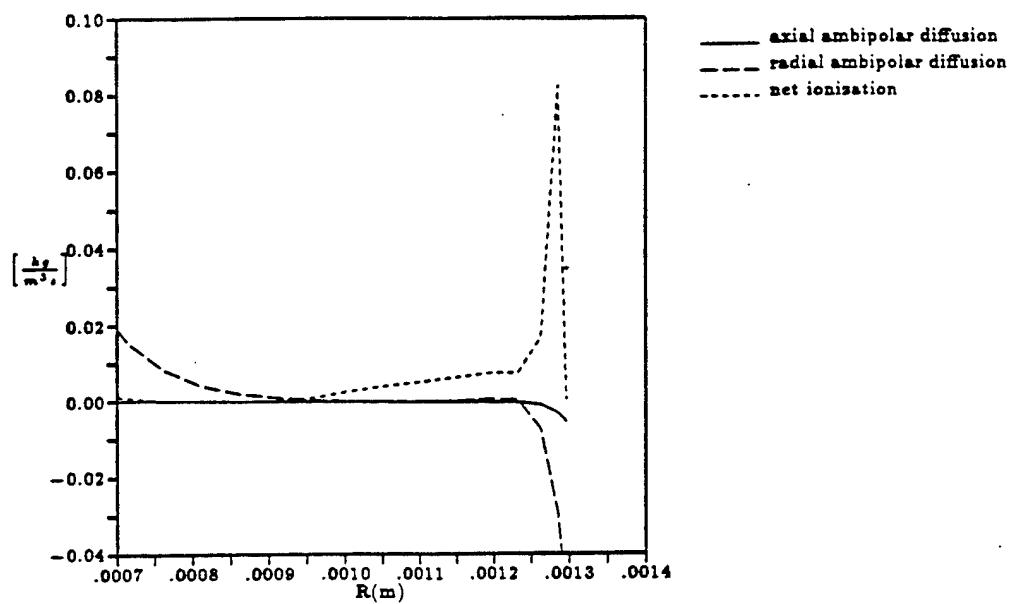
Figure 9: Radial Profiles of Some Terms in the Electron Density Equation in the Current Attachment Region Just Downstream of the Constrictor Exit
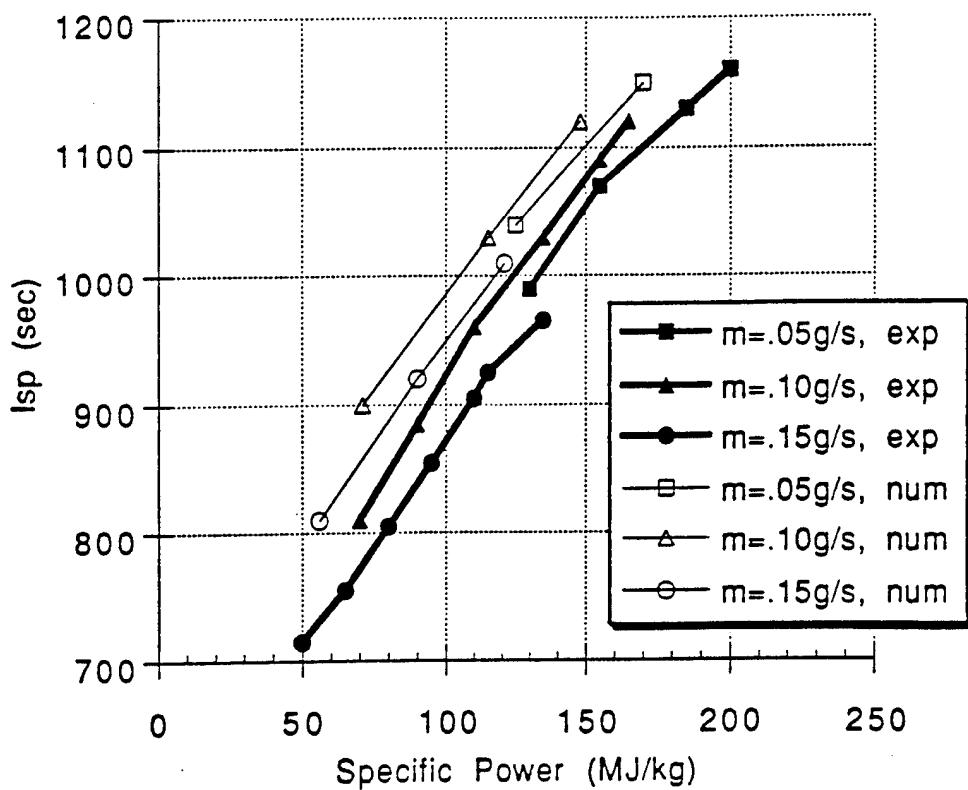
Figure 10: Predicted Isp Compared to Experimental Data, German TT1 Radiation-Cooled Hydrogen Arcjet
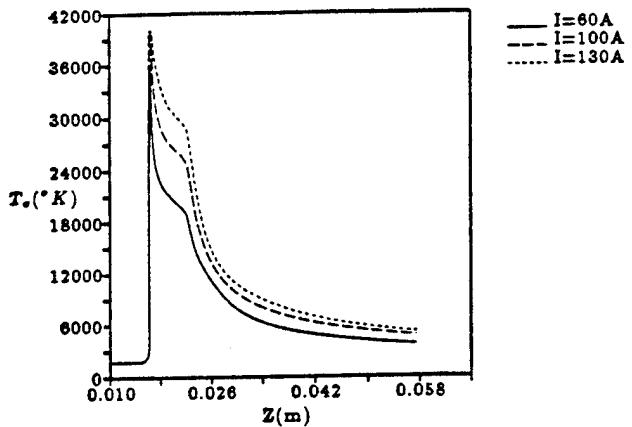
Figure 11: Centerline Axial Electron Temperature Profiles for $\dot{m} = 0.1$g/s at Three Applied Currents
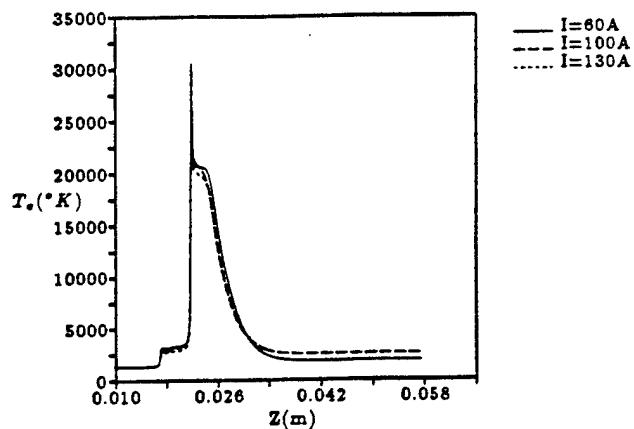
Figure 14: Anode Wall Axial Electron Temperature Profiles for $\dot{m} = 0.1$g/s at Three Applied Currents
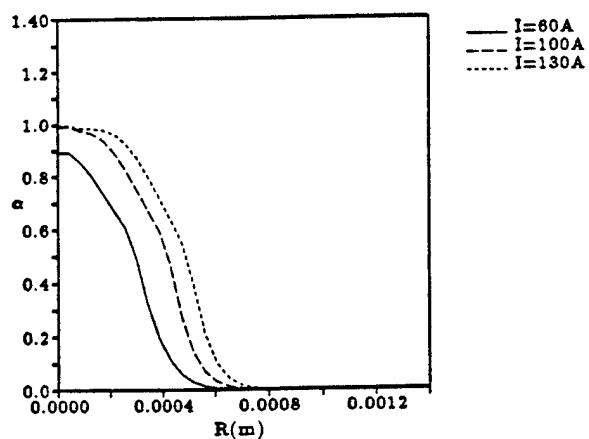
Figure 12: Ionization Fraction Radial Profiles at the Constrictor Exit for $\dot{m} = 0.1$g/s at Three Applied Currents
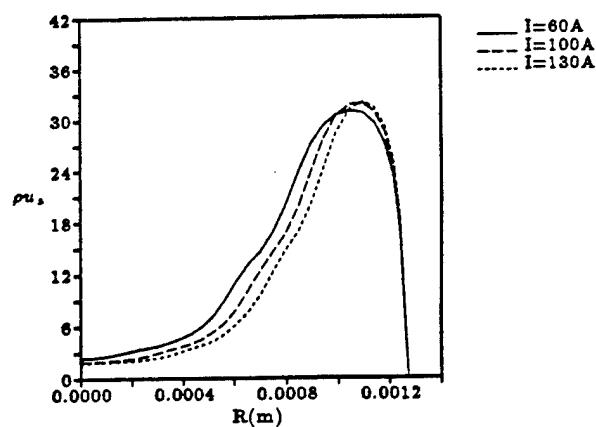
Figure 15: Mass Flux (ρu_z) Radial Profiles at the Constrictor Exit for $\dot{m} = 0.1$g/s at Three Applied Currents
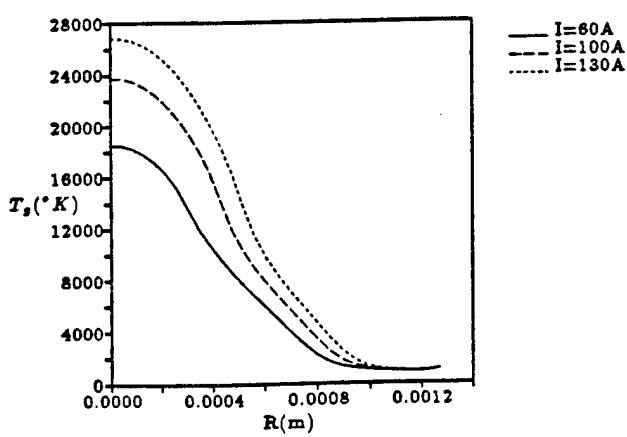
Figure 13: Radial Gas Temperature Profiles at the Constrictor Exit for $\dot{m} = 0.1$g/s at Three Applied Currents
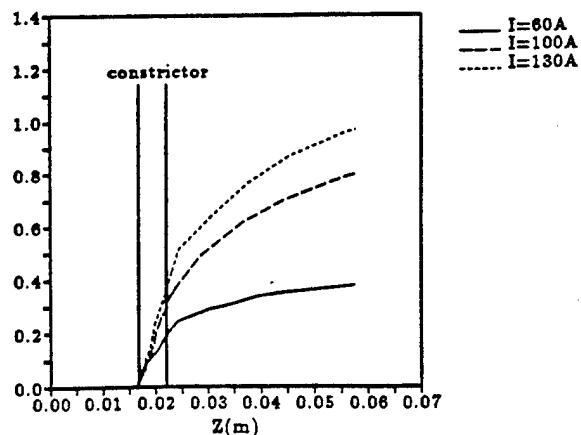
Figure 16: Mass Flow Fraction Inside the Arc $(\alpha > 0.01)$ as a Function of Axial Location for $\dot{m} = 0.1$g/s at Three Applied Currents

16
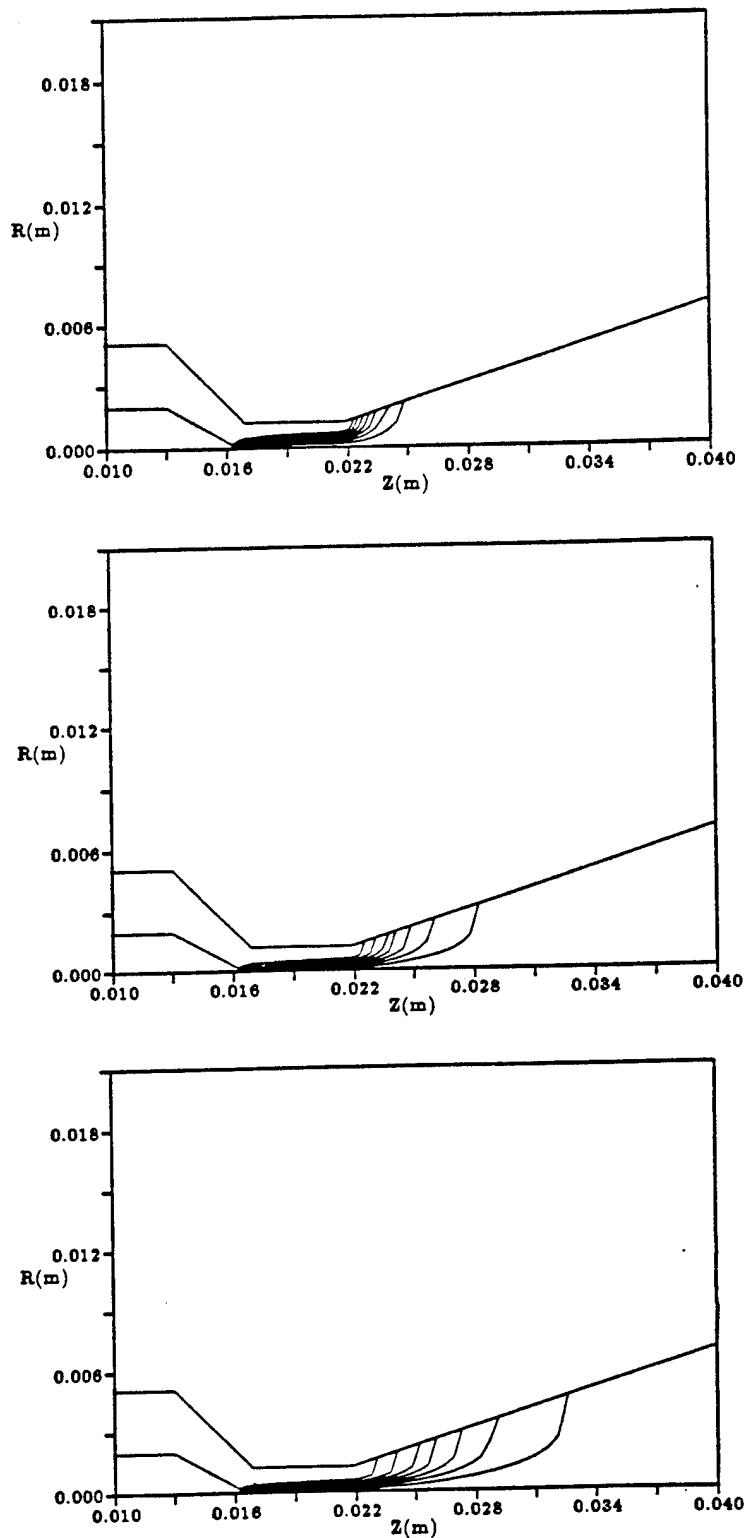
Figure 17: Enclosed Current Contours for $\frac{P}{\dot{m}} = 120\text{MJ/kg}$: I=60A, $\dot{m} = 0.05\text{g/s}$ (top); I=100A, $\dot{m} = 0.10\text{g/s}$ (middle); and I=130A, $\dot{m} = 0.15\text{g/s}$ (bottom)
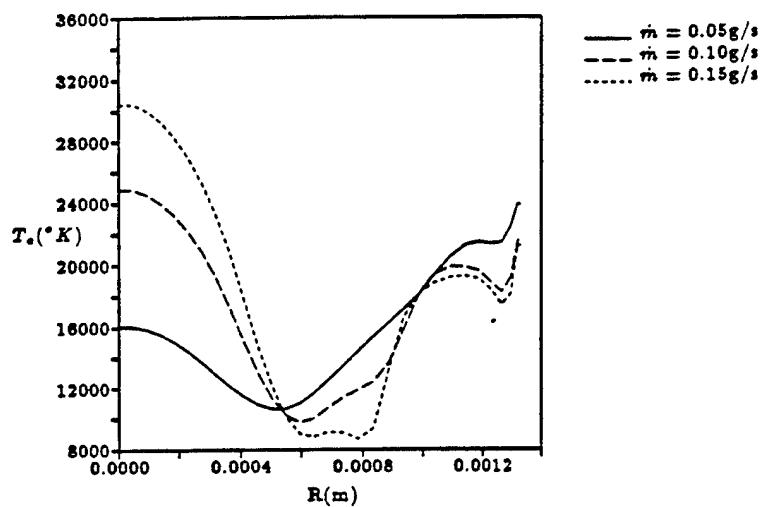
Figure 18: Radial Profiles of Electron Temperature 0.25mm Downstream of the Constrictor Exit for a Specific Power of 120MJ/kg


Boron Nitride   Molybdenum   Tungsten
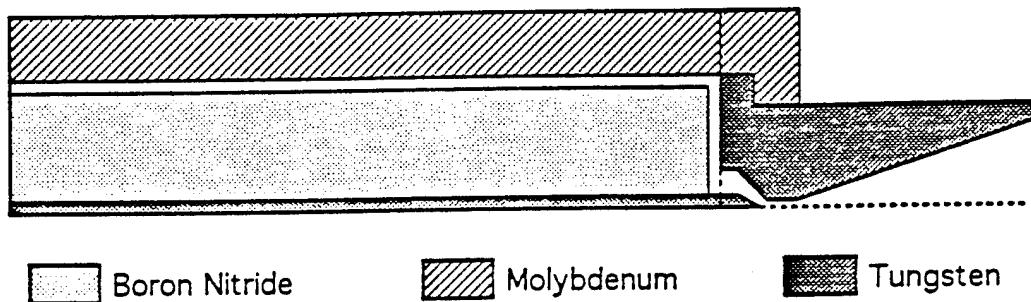
Figure 19: Arcjet Thruster Assembly Schematic for Anode Heat Balance Model
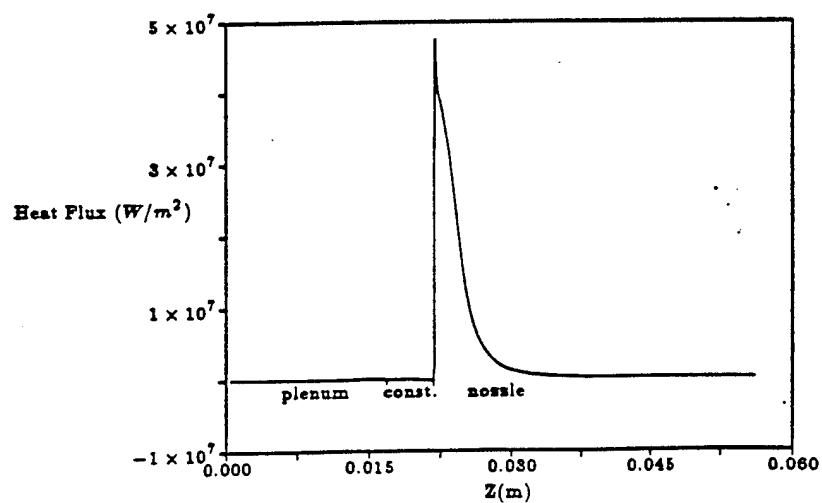
Figure 20: Heat Flux to Anode from Baseline Case Flow Simulation Results ($\dot{m} = 0.1$g/s, I=100A)

18

Contours 40°K
Min 300
Max 1550
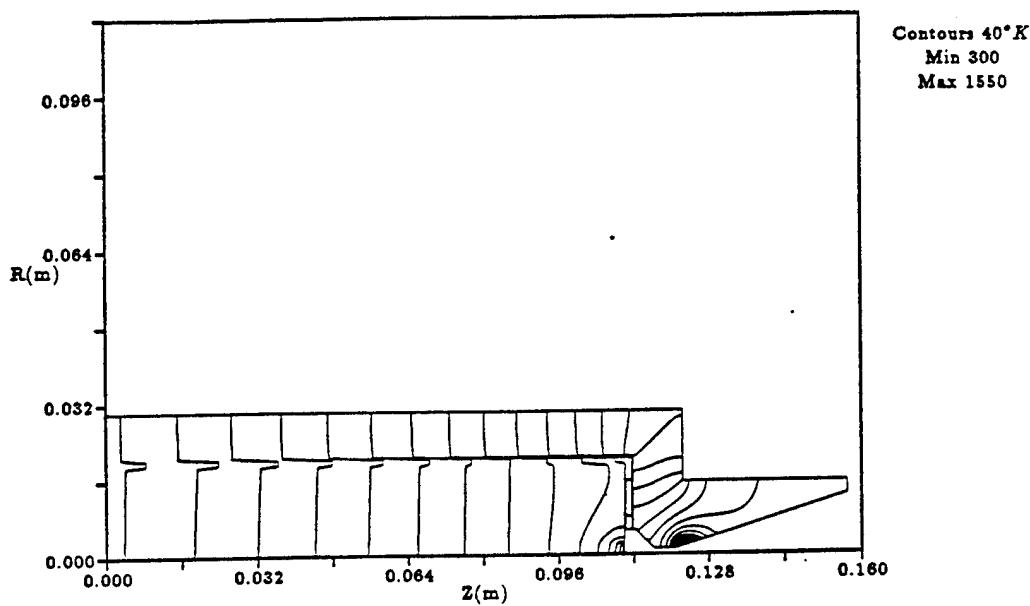
Figure 21: Thruster Assembly Temperature Distribution for Baseline Case Heat Flux
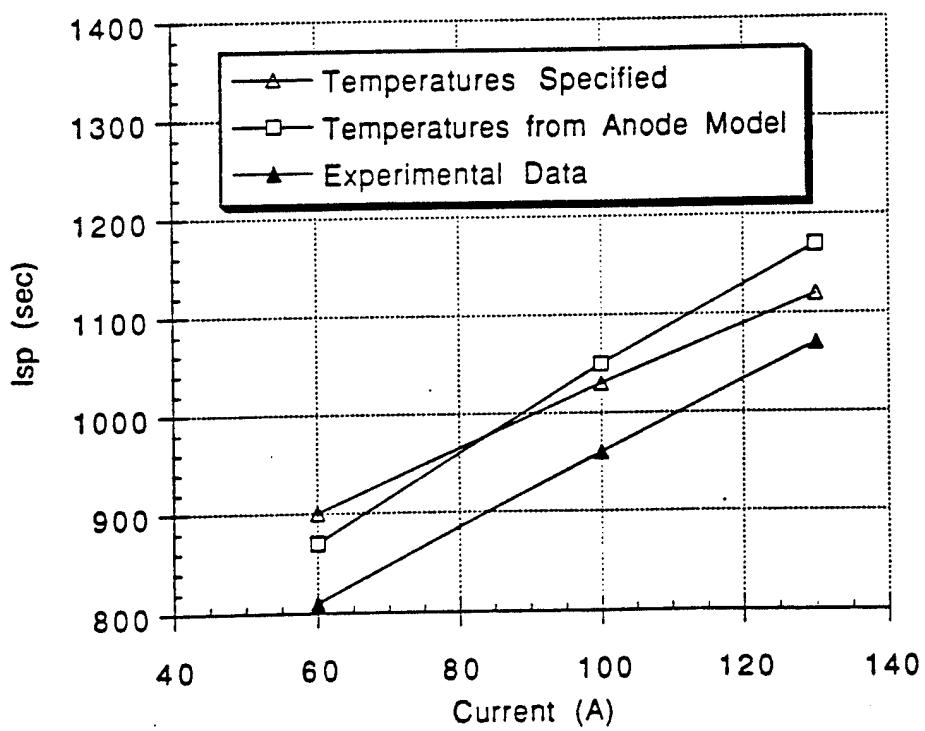
Figure 22: Effect of Anode Model Coupling on Predicted Performance ($\dot{m} = 0.1g/s$)
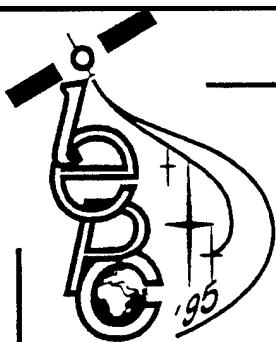
IEPC-95-240

Two-Dimensional Hybrid Particle-In-Cell (PIC) Modeling of Hall Thrusters

John Michael Fife and Manuel Martinez-Sanchez
Space Systems Laboratory
Massachusetts Institute of Technology
Cambridge, MA, USA

Two-Dimensional Hybrid Particle-In-Cell (PIC) Modeling of Hall Thrusters *

John Michael Fife[†] and Manuel Martinez-Sanchez[‡]
Massachusetts Institute of Technology
Cambridge, Massachusetts

A two dimensional numerical simulation was written for the acceleration channel and near plume of a Hall thruster, and the results were compared with experimental measurements. The model assumes quasineutrality, Maxwellian electrons, and Bohm diffusion across the magnetic field lines. Heavy particles are simulated directly with a Particle-In-Cell (PIC) method, while electrons are modeled as a fluid continuum. A time-accurate electron energy equation is used to determine electron temperature, and a generalized Ohm's Law is used to determine the electric field strengths. Results indicate a strong correlation with experimental performance data. In particular, the simulation is able to predict thrust, torque, power, and efficiency to within 7% of the experimental values. In addition, wall erosion rates in the Russian SPT can be predicted to within 40% using a simple analysis of the simulation results. Two-dimensional plasma distributions are similar to experiment, but do not match in all cases. This is most likely due to the general Bohm diffusion model applied globally to the Hall thruster plasma.

Introduction

In 1992, Lentz [1] used a one-dimensional numerical model to accurately predict the operating characteristics and plasma parameters in the acceleration channel of a Japanese Type II Hall Thruster. The assumptions of the Lentz model included quasineutrality, Bohm diffusion across the magnetic field, constant ratio of ionization energy loss to total electron energy loss, and fixed magnetic field.

Due to the success of the Lentz one-dimensional model, this research extends the model to two dimensions, using similar assumptions. The physical dimensions are considered an input to the numerical model, so any Hall thruster geometry may be used, as well as concept designs. A computational grid is mapped to physical space using nonuniform mapping techniques common in computational fluid mechanics. The magnetic field is pre-computed from the iron pole locations and solenoid strengths. Electrons are modeled as a Maxwellian Fluid, while the heavy species are treated with a modified Particle-In-Cell (modified PIC) methodology. Collisionality is limited to electron-neutral ionization and ion-neutral momentum exchange. The overall scheme may be called "hybrid-PIC" since both fluid and PIC methods are used self-consistently.

This paper describes the governing equations and numerical method used in modeling the Hall Thruster in two dimensions. Results are then explained, and comparisons are made with experimental data for Russian SPT-class thrusters.

Governing Equations

0.1 Magnetic Field

The magnetic field is considered equal to the vacuum field, and hence expressible as $\vec{B} = \nabla\sigma$. Since $\nabla \cdot \vec{B} = 0$, it is also possible to define a magnetic stream function whose gradient is everywhere orthogonal to $\vec{B}$. One such stream function is λ, given by

$$\frac{\partial\lambda}{\partial z} = r\frac{\partial\sigma}{\partial r} = rB_r \qquad (1)$$

$$\frac{\partial\lambda}{\partial r} = -r\frac{\partial\sigma}{\partial z} = -rB_z \qquad (2)$$

If $\hat{n}$ is the distance normal to the magnetic field lines, then,

$$\frac{\partial}{\partial\hat{n}} = \frac{\partial\lambda}{\partial\hat{n}}\frac{\partial}{\partial\lambda} = -rB\frac{\partial}{\partial\lambda} \qquad (3)$$

Electron Momentum Balance

Along lines of force, the electrons are assumed to lie in Boltzmann equilibrium with constant electron temperature

$$\phi - \frac{kT_e}{e}\ln(n_e) = \phi^*(\lambda) \qquad (4)$$

Across lines of force, a force balance on electrons may be written as

$$\nabla P_e = -en_e\vec{E} + m_e n_e \nu_{ei}(\vec{u}_i - \vec{u}_e) \qquad (5)$$

where ν_{ei} is the electron-ion collision frequency. Rewriting in terms of the electron mobility, μ_e, and taking only the component normal to the magnetic field lines,

$$u_{e,\hat{n}} = \mu_e\left(\frac{\partial\phi}{\partial\hat{n}} - \frac{kT_e}{en_e}\frac{\partial n_e}{\partial\hat{n}} - \frac{k}{e}\frac{dT_e}{d\hat{n}}\right) + u_{i,\hat{n}} \qquad (6)$$

Bohm Diffusion

Assuming Bohm diffusion,

$$\mu_e = \frac{1}{16B} \qquad (7)$$

Applying this Bohm mobility to Equations (4) and (6),

$$\frac{\partial\phi}{\partial\hat{n}} = -rB\frac{d\phi^*}{d\lambda} + \frac{kT_e}{en_e}\frac{\partial n_e}{\partial\hat{n}} - \frac{rBk\ln(n_e)}{e}\frac{dT_e}{d\lambda} \qquad (8)$$

$$u_{e,\hat{n}} = -\frac{r}{16}\frac{d\phi^*}{d\lambda} - \frac{kr}{16e}(\ln(n_e) - 1)\frac{dT_e}{d\lambda} + u_{i,\hat{n}} \qquad (9)$$

Current Conservation

To conserve current, $I_a = I_e + I_i$, independent of λ. Written in terms of integrals along magnetic field lines,

$$I_a = 2\pi e\int_0^l n_e u_{e,\hat{n}} r\, ds - 2\pi e\int_0^l n_i u_{i,\hat{n}} r\, ds \qquad (10)$$

Using Equation (8) and simplifying,

$$\frac{d\phi^*}{d\lambda} = \frac{-I_a - \frac{2\pi k}{16}\frac{dT_e}{d\lambda}\int_0^l n_e(\ln(n_e) - 1)r^2\, ds}{\frac{2\pi e}{16}\int_0^l n_e r^2\, ds} \qquad (11)$$

Electron Energy

An electron energy equation may be derived under the assumptions that electrons have a Maxwellian velocity distribution and that the pressure dyad reduces to a scalar pressure term, $n_e kT_e$:

$$\frac{\partial}{\partial t}\left(\frac{3}{2}n_e kT_e\right) + \nabla \cdot \left(\frac{5}{2}n_e\vec{u}_e kT_e + \vec{q}_e\right) = S \qquad (12)$$

Here, the directed kinetic energy of electrons is neglected, since, for Hall thrusters, this is found to be smaller than the random kinetic energy.

In Equation (12), S is the electron energy source due to ionization, radiation, and charge-field interactions. The net energy cost for producing a single ion, φ, can be expressed as the sum of the energy required for ionization, plus the energy lost to excitation of neutral atoms. An analytical expression for φ is derived by Dugan et. al. [2]. The result can be fitted closely as,

$$\varphi' = Ae^{-\frac{B}{z}} + C \qquad (13)$$

where φ' and z are normalized ion production cost and dimensionless electron kinetic temperature, $\varphi' = \frac{\varphi}{E_i}$ and $z = \frac{kT_e}{E_i}$. The constants A, B, and C are given in Table 1. The volumetric electron energy loss rate can then be given as,

$$S_1 = \dot{n}_e\varphi' E_i \qquad (14)$$

The electron energy source due to the electric field is shown [3] to be,

$$S_2 = \frac{16Bj^2}{en_e} \qquad (15)$$

2

	A	B	C
Argon	0.188	0.624	1.75
Xenon	0.254	0.677	2.00

Table 1: Constants to fit the Dugan ion production cost model.

Combining the sources explicitly,

$$S = -\dot{n}_e \varphi' E_i + \frac{16Bj^2}{en_e} \qquad (16)$$

Heavy Species

Heavy species are modeled as discrete particles with negligible temperature. Therefore, only conservation of mass and momentum are applicable. Recombination and charge exchange are found to be small and both are neglected. The ion-neutral collision cross section for argon and xenon are assumed to be 1.40×10^{-18} and 2.15×10^{-18}, respectively. Using these values with experimental Hall thruster plasma densities, the mean free path for both ions and neutrals is found to be large in most regions. Therefore, ion-neutral momentum exchange is neglected.

The magnetic part of the Lorentz force is ignored, since the Larmor radius for ions is large. Therefore, the force on an ion is simply,

$$\vec{F}_i = e\vec{E} \qquad (17)$$

Neutrals, being uncharged, only experience velocity changes if they encounter walls. Their mean free path is large compared to the scale of the device.

Ionization Rate

In this model, it is assumed that only electron-neutral collisions can produce ions. Also, it is assumed that only one degree of ionization may exist. Therefore, $\dot{n}_i = \dot{n}_e$.

The nonelastic ionization cross section is approximated according to Drawin [4] as a function of electron energy. Assuming a Maxwellian electron distribution, the resulting expression may be written as,

$$\dot{n}_e = n_e n_n \varsigma(T_e) \qquad (18)$$

where ς is plotted for argon and xenon versus electron temperature in Figure 1.
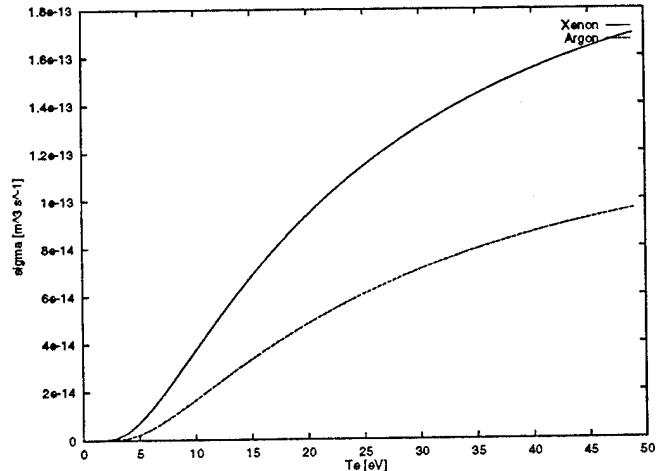
Figure 1: Ionization rate parameter, ς $[m^3 \cdot {}^{-}1]$, for argon and xenon.

Boundary Conditions

To determine the electron energy loss to the walls, it is assumed that the electron flux is equal to the ion flux normal to the wall, and that all ions recombine there with no secondary electron emission. Therefore, the electron energy flux to the wall is simply,

$$E_w = 2kT_e\Gamma_{i,w} \qquad (19)$$

All neutrals are assumed to deflect off the walls elastically, at random angles. Likewise, ions recombine at the wall to form neutrals with random direction and velocity magnitudes equal to the impinging ion's.

The cathode and anode are assumed to be at a constant potential difference. Also, the electron temperature at the cathode is fixed, based on experimental data, to $2eV$. The electron temperature at the anode is assumed to have zero slope. The inner and outer walls of the thruster are assumed to be electrically insulating.

Neutrals are assumed to enter the acceleration channel at the injector. The injector is modeled as an annular ring in the center of the back wall (anode) of the channel. The total area of the injector is set roughly to the injector area of the device being modeled. However, precise data is not available for the SPT,

3

so the injector area is set to approximately 30% of the anode area.

Neutrals are introduced with an axial velocity equal to the speed of sound ($\sqrt{\frac{5kT_e}{3m_n}}$) at the anode temperature (1000 $^\circ K$ for the SPT). The radial velocity component for each neutral is taken to be a random value between $-|\bar{v}_x|$ and $|\bar{v}_x|$, where $|\bar{v}_x| = \sqrt{\frac{2kT_n}{\pi m_n}}$ is the mean directional velocity for a Maxwellian fluid.

The thruster is assumed to have an ideal power supply which maintains constant discharge potential while allowing the discharge current to vary. However, if the power level exceeds a given point (1 kW for the SPT operating at 200 Volts), it goes into a power limiting mode which drops the discharge potential accordingly.

Numerical Method

On the heavy particle time scale, a time-accurate solution to the governing equations can be achieved by iterating successively, as shown in Figure 2.

A 51 × 13-node nonuniform spatial grid is used. Rotational symmetry is assumed. Therefore, only a meridional section of the Hall thruster is modeled. Grid spacing is determined by the timestep of the simulation. It is set to the smallest value which is much larger than the maximum distance traveled by a particle in one timestep. Figure 3 shows the spatial grid used for the computations presented in this paper.

Magnetic Field

The magnetic field is pre-computed by specifying the geometry of the iron poles (which are assumed to have infinite permeability), and solving Laplace's equation on the regions exterior to them. The method of red-black ordering was found to be the most flexible. Solutions take 8 hours on a DEC Alpha workstation, but programming is minimal and it works for a variety of axisymmetric geometries.

Integration of Electron Equations

It is possible to combine the electron energy equation with Ohm's Law and the electron
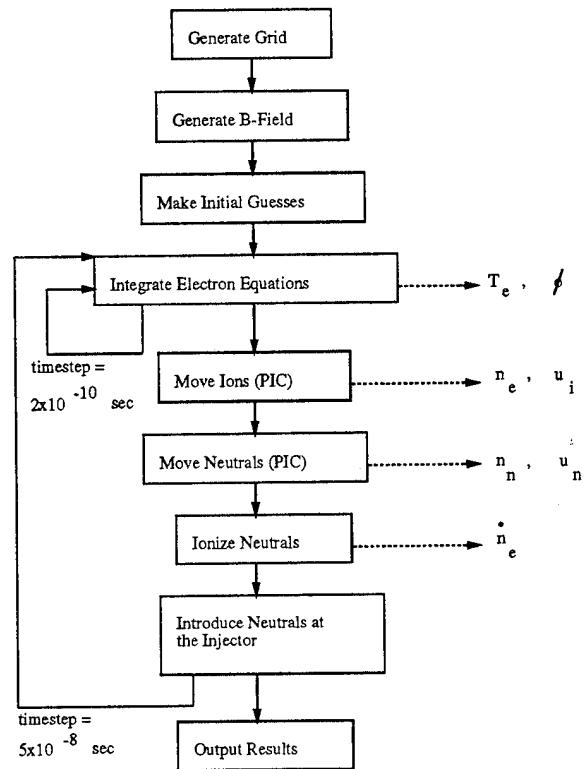

Figure 2: Overview of the numerical method.
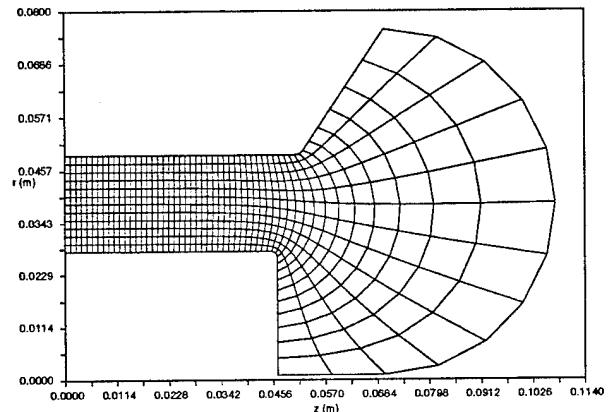
Figure 3: Spatial grid for the SPT-100 geometry.

current equation. The result is of the form,

$$\frac{\partial T_e}{\partial t} + \bar{I}\frac{\partial T_e}{\partial \lambda} + \bar{J}\left(\frac{\partial T_e}{\partial \lambda}\right)^2 + \bar{K}\frac{\partial T_e}{\partial \lambda}T_e$$

$$+\bar{L}T_e + \bar{M}T_e^2 + \bar{N} + \bar{O}T_e\frac{\partial^2 T_e}{\partial \lambda^2} = 0$$

(20)

where $\bar{I}, \bar{J}, ...\bar{N}$ represent factors obtained by itegrating along magnetic field lines from the inner to the outer wall. This equation is a function of slow time parameters and of the electron temperature. The slow time parameters are taken to be those related to heavy particle motion (n_e, n_n and v_i), and those fixed geometrically (B, r). Holding the slow parameters constant, this equation is solved time-accurately for electron temperature, which evolves faster, using MacCormack's method. The space potential can then be found on the whole domain by using Boltzmann equilibrium and Ohm's Law.

PIC Method for Heavy Species

In this simulation, heavy species are modeled time-accurately using a modified Particle-In-Cell (PIC) method. The standard PIC method [5] is a direct simulation technique which models a gas as discrete particles. Figure 4 shows the operation of one standard PIC cycle.

The method used here has several unique features which enhance performance for the specific problem of simulating a Hall thruster plasma with a nonuniform grid:

- Fluid equations and quasineutrality determine fields, not Poisson's equation. This allows spatial scales much greater than the Debye length.

- PIC superparticles may have variable mass.

- Computational coordinates for each particle are maintained with a unique particle following algorithm based upon Newton's method

Complete cases take 20 hours to execute on a DEC Alpha workstation.

Convergence

Since the method is time-accurate, there is no guarantee that the system will converge to a steady state solution. Two types of instabilities may prevent convergence:

- Plasma instabilities due to convection and diffusion of electrons and ions, combined with ionization kinetics

- Numerical "noise" due to the limitations of the PIC method in simulating a continuum of heavy particles

The parameters are averaged over a long time scale, and iteration is stopped when the averages reach a constant value. The time it takes for convergence is assumed to be, at the very minimum, the time for convection of slow neutrals along the length of the grid.

Results and Discussion

Bishaev and Kim used diagnostic probes to measure plasma parameters in the acceleration channel of a Hall thruster. The results in this paper have been obtained with a simulated geometry which closely matches what they reported [6]. The operating conditions are given in Table 2.

Operating Parameters for the SPT	
Propellant	Xenon
ϕ_d	200 Volts
$\dot{m}$	3 mg/s
Vacuum	2×10^{-4} Torr
$B_{r,max}$	.018 Tesla

Table 2: Operating conditions for the Bishaev/Kim SPT experiments.

The magnetic field parameters are shown on the computational domain in Figures 5 and 6. Although the radial magnetic field strength is close to the experimental value, the contours of magnetic flux are not matched exactly. This is due to differences in iron pole geometry, as well as to the infinite permeability and ideal solenoid assumptions used in the numerical model.
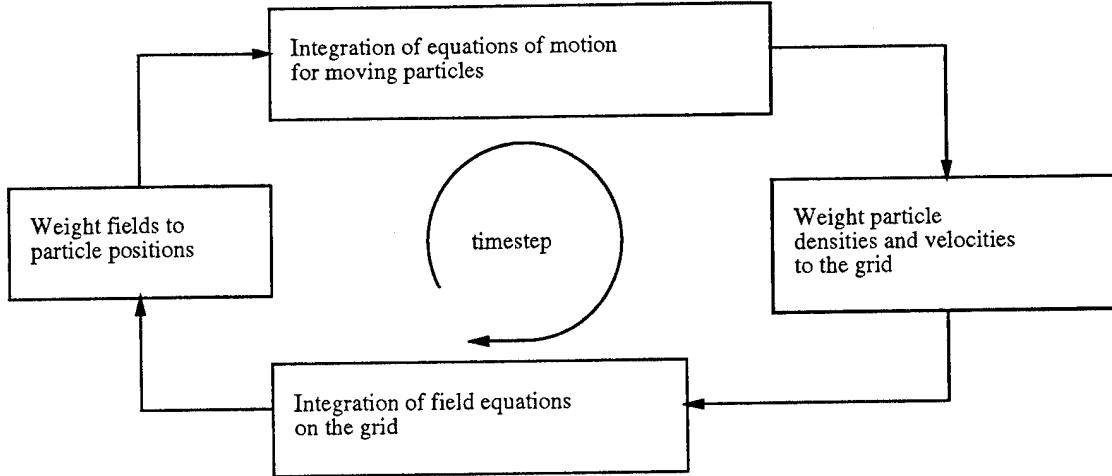
Figure 4: PIC computational cycle [5].
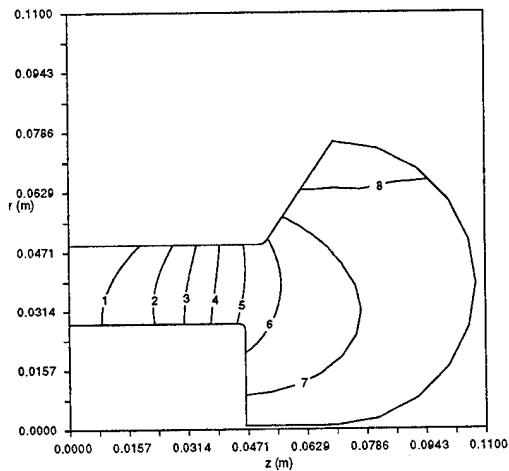
Figure 5: Magnetic stream contours, λ $[T \cdot m^2]$, computed for the Bishaev/Kim SPT geometry. The contour numbers correspond to the values of λ listed in the key.


Figure 6: Magnitude of the magnetic field, B $[T]$, computed for the Bishaev/Kim SPT geometry. The contour numbers correspond to the values of B listed in the key.

Performance

Although the Bohm diffusion coefficient is generally written as,

$$D_{Bohm} \approx \frac{kT_e}{16eB} \qquad (21)$$

it is known to vary by an order of magnitude depending upon the plasma parameters. Therefore, the simulation was run for three cases to isolate the best fit for the Hall thruster. A constant K_{Bohm} was introduced as a multiplier,

$$D_{Bohm} \approx K_{Bohm}\frac{kT_e}{16eB} \qquad (22)$$

and the simulation was run for $K_{Bohm} = 0.75$, 1.0, and 1.25. After convergence, the results were averaged in time. Results are shown in Table 3.

It is interesting to note that, for the model used, varying K_{Bohm} is equivalent to inversely

6

varying B. This is due to the form of the Bohm conductivity. K_{Bohm} and B always appear in the model together as $\frac{K_{Bohm}}{B}$.

The first case ($K_{Bohm} = 0.75$) shows the effect of "quenching" the device with more propellant than is possible to ionize. At low K_{Bohm}, the power input to the electrons is lower, and ionization rate is reduced. The higher neutral density acts as an energy sink, keeping the electron temperature low and reducing the ionization rate further. This is self-perpetuating, since the ion production cost increases at lower energies, as seen in Equation (13).

In the second case, the anode current matches the experimental value almost exactly. The efficiency of this model reproduces the advertised efficiency of the SPT-100, which is 50%. The specific impulse is also a close match with experimental data. This is not surprising, since the discharge potential was fixed to the same value measured, and the simulation reached full propellant utilization.

The third case, $K_{Bohm} = 1.25$, represents the effect of reduced electron impedance. The higher electron mobility increases their heating rate. This moves the ionization region toward the anode, increasing the ion wall losses.

The Bohm diffusion mechanism is not well understood. It is an empirical fit with some uncertainty. Therefore, it is surprising that the standard case fits the experimental performance data so well. Furthermore, it is curious that the correlation degrades so rapidly as K_{Bohm} deviates from unity, particularly on the low side.

Two-Dimensional Results

Figures 7 through 13 show the time-averaged two-dimensional results for the case $K_{Bohm} = 1.0$. Some discrepancies exist between the experimental data of Bishaev and Kim, and the results of the two-dimensional simulation. The potential at the exit of the channel is found experimentally to be 10 Volts, whereas the numerical model predicts it to be 118 Volts. This discrepancy may be due to the location of the cathode. The simulation cathode is assumed to be located about 2.3 cm downstream of the channel. For the experiments of Bishaev and Kim, it may have been located closer. Vacuum chamber back-pressure was thought to cause this, but it was ruled out by numerically modeling the neutral particle flux from the chamber. The effect was negligible, so chamber back-pressure was ignored. Another explanation may be some type of enhanced electron conductivity in or near the plume which is not being modeled.
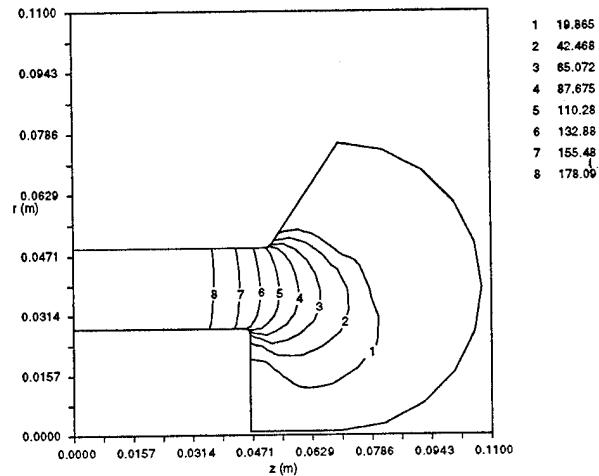

Figure 7: Contours of space potential (ϕ $[V/m]$). The contour numbers correspond to the values of ϕ listed in the key. $K_{Bohm} = 1.0$; $\dot{m} = 3$ mg/s; $\phi = 200$ Volts; $I_a = 3.1$ A.

The ion density in Figure 8 also matches poorly with the experimental results. The peak experimental value is about 7×10^{17} m^{-3} near the exit of the channel. The simulation predicts it to be twice that and to occur closer to the anode.

The assumption of constant electron temperature along lines of force seems to hold only partially. This may imply that the plasma is not entirely in equilibrium along the magnetic lines, and perhaps the Boltzmann relation is not completely applicable. Alternatively, perhaps they are in equilibrium, but an electron energy balance holds instead of Boltzmann's relation. This is a matter under investigation. Nevertheless, the peak electron temperature is predicted correctly.

Also, the temperature gradients are strong in the experimental measurements. This is not the case with the simulation. One reason for this discrepancy may be overprediction

7

	Experimental	Numerical $K_{Bohm} = 0.75$	$K_{Bohm} = 1.00$	$K_{Bohm} = 1.25$
I_a [A]	3.15	0.39	3.10	2.75
I_b [A]	2.10	0.52	2.20	1.90
I_{SP} [s]	1530	200	1475	1400
F [N]	.045	.006	.043	.041
$\eta_u = \dot{m}_i/\dot{m}$	0.95	0.24	1.00	0.86
$\eta_a = I_b/I_a$	0.67	1.33	0.71	0.69
$\eta_e = (e/2m_i\phi_a)(F/I_b)^2$	0.84	0.24	0.71	0.86
$\eta = \eta_u\eta_a\eta_e$	0.54	0.08	0.50	0.51
I_{wall} [A]	1.0	0.03	1.1	2.3
ξ_s [$\times 10^{-9}$ m/s]	7.0	1.2	4.0	3.1
$Torque/(F \cdot r_{mean})$	.02-.08	.037	.031	.035

Table 3: Performance results from the numerical simulation. $\dot{m} = 3$ mg/s; $\phi = 200$ Volts.
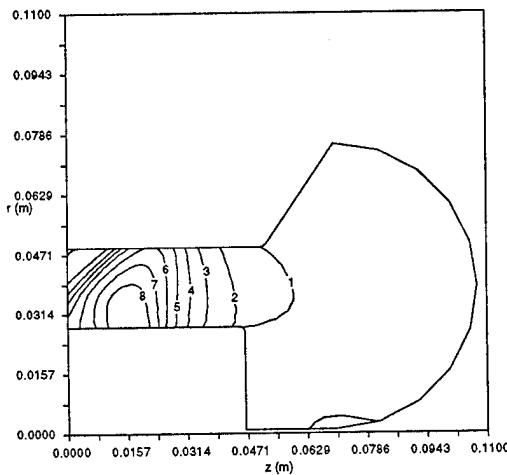

Figure 8: Contours of plasma density (n_i [m^{-3}]). The contour numbers correspond to the values of n_i listed in the key. $K_{Bohm} = 1.0$; $\dot{m} = 3$ mg/s; $\phi = 200$ Volts; $I_a = 3.1$ A.

Figure 9: Contours of electron temperature (T_e [$°K$]). The contour numbers correspond to the values of T_e listed in the key. $K_{Bohm} = 1.0$; $\dot{m} = 3$ mg/s; $\phi = 200$ Volts; $I_a = 3.1$ A.

of the thermal diffusion coefficient, which was derived from the Bohm diffusivity.

Experimental measurements of ion flux show most of the flux vectors leaving the region of high plasma density, as expected, and traveling along potential lines or to the walls. The simulation results (Figure 11) show a similar pattern of ion flux, with the vectors emanating from a high density region closer to the anode and closer to the inner wall.

The two-dimensional numerical results are consistent when taken as a set. Electron temperature increases from the cathode to the acceleration zone, since there is little inelastic collision loss in that region due to the low neutral density. Once inside the channel, the electrons enter a region of higher neutral density. Ionization peaks when the neutral density is increasing. Electron temperature then decreases from inelastic losses.

8
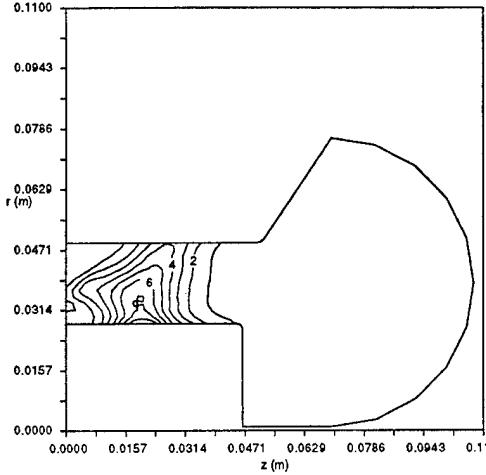
Figure 10: Contours of ionization rate $(\dot{n}_i \ [m^{-3}s^{-1}])$. The contour numbers correspond to the values of $\dot{n}_i$ listed in the key. $K_{Bohm} = 1.0$; $\dot{m} = 3$ mg/s; $\phi = 200$ Volts; $I_a = 3.1$ A.
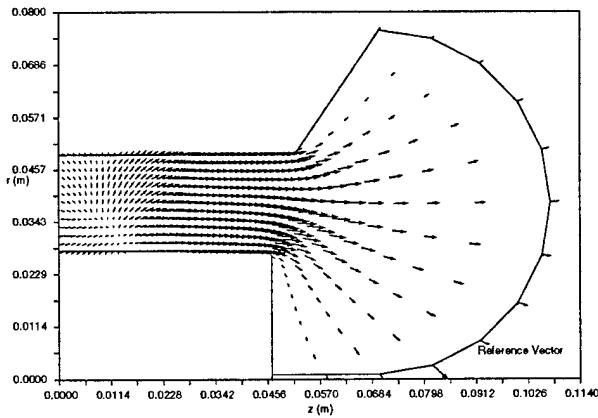

Figure 11: Vectors of ion number flux $(\vec{\Gamma}_i \ [m^{-2}s^{-1}])$. The reference vector represents a flux of $14.8 \times 10^{20} m^2/s$. The contour numbers correspond to the values of $\vec{\Gamma}_i$ listed in the key. $K_{Bohm} = 1.0$; $\dot{m} = 3$ mg/s; $\phi = 200$ Volts; $I_a = 3.1$ A.
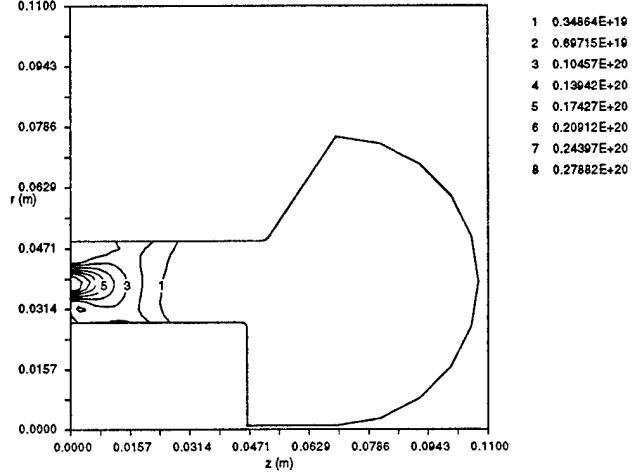

Figure 12: Contours of neutral number density $(n_n \ [m^{-3}])$. $K_{Bohm} = 1.0$; $\dot{m} = 3$ mg/s; $\phi = 200$ Volts; $I_a = 3.1$ A.
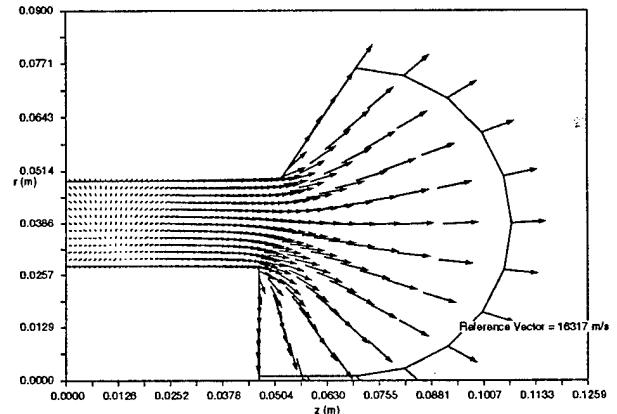
Figure 13: Vectors of ion velocity $(\vec{u}_i \ [m/s])$. The reference vector represents a velocity magnitude of 16317 m/s. $K_{Bohm} = 1.0$; $\dot{m} = 3$ mg/s; $\phi = 200$ Volts; $I_a = 3.1$ A.

Torque

The torque on the device may be written as the sum of the azimuthal moments on the ions in each grid cell as,

$$T = \sum 2\pi r^2 A_{cell} e n_i \vec{u}_i \times \vec{B} \qquad (23)$$

The torque is generally nonimensionalized by dividing by the thrust and the mean radius. The torque parameters are given in Table 3, and are consistent with experimental estimates [7, 8].

9

Ion Wall Impingement

From the numerical simulation, average wall impingement current is calculated to be 1.1 Amperes. According to Bishaev and Kim [6], ion loss to the walls is approximately 1.0 Ampere. Ion wall currents for the other cases are also listed in Table 3.

The SPT-100 insulator wall is known to sputter most near the channel exit [9]. Indeed, Figure 13 shows the mean ion velocities at the wall to be a maximum near the exit of the channel. At the inner wall, ion current density is $48 A/m^2$ normal to the wall. A comparison of wall sputtering rate can be made by using the relation,

$$\xi_s = j_{i,w} S_v \qquad (24)$$

where ξ_s is the wall reduction rate in m/s, $j_{i,w}$ is the normal component of the ion current density, and S_v is the volumetric sputtering coefficient. Abgaryan et. al. [10] measured the sputtering properties of borosil, a dielectric wall material used in SPTs. They found that $S_v \approx .08 \; (mm)^3/C$ for ion energies of 33 eV at an 80 degree angle of incidence. Therefore,

$$\xi_s \approx 4 \times 10^{-9} m/s \qquad (25)$$

which is very close to the experimental value of wall sputtering for SPTs. At the inner insulator wall, the initial sputtering rate is 7×10^{-9} m/s from experiments by Garner et. al. [9]. The SPT may easily have twice the ion flux at that point, however, in which case the calculated value would be very close. Nevertheless, the order of magnitude analysis agrees with experimental results.

Plasma Oscillations

The Hall thruster simulation does not reach a steady state solution. Plasma parameters fluctuate continually, even after long convergence times. The two-dimensional results presented above have been averaged over .5 ms. The anode current for this period is given in Figure 14. It can be seen that I_a fluctuates $\pm 15\%$. The electron temperature is plotted in Figure 15 for the same time period.

Two of the slow characteristic frequencies in Table 4 can be seen in the data. The lowest frequency, related to the travel of neutrals
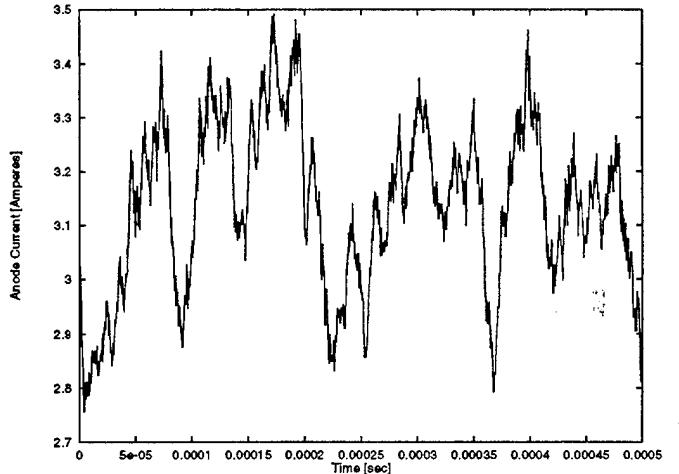
Figure 14: Long time history of anode current, I_a [Amperes].
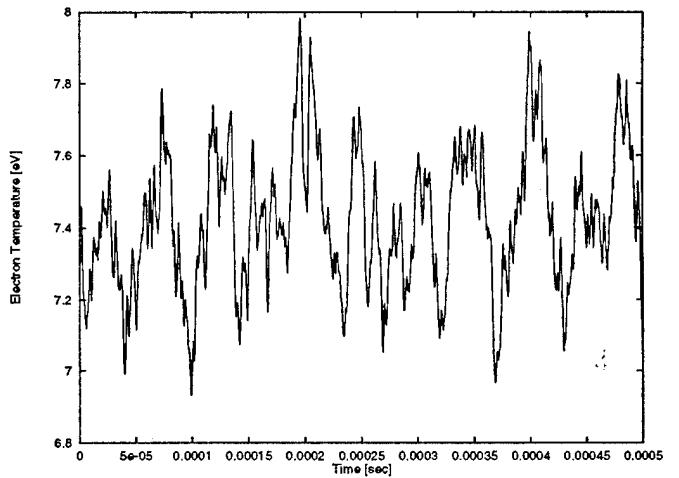
Figure 15: Long time history of electron temperature, T_e [eV], at z = 1.9 cm and r = 3.6 cm.

from the injector to the exit of the channel, appears in Figure 14 as roughly 6 kHz. Also, by examining Figure 15, a clear 28 kHz behavior is seen, possibly due to neutrals traversing the length of the ionization region.

To closely examine the high frequency oscillations, n_e and n_n have been plotted on a short time scale (.05 ms) in Figures 16 and 17 for a particular node near the peak of ionization rate.

The dominant high frequency information in Figure 16, may be seen to be superimposed

10

|	Velocity, m/s	Distance, cm	Frequency, kHz
Neutrals traverse the channel	300	4	8
Neutrals traverse the ionization region	300	1	30
Ions traverse the channel	3000	4	75
Ions traverse the ionization region	500	1	50
Neutrals traverse two grid cells	300	.24	125
Ions traverse two grid cells	600	.24	250

Table 4: Characteristic frequencies expected.
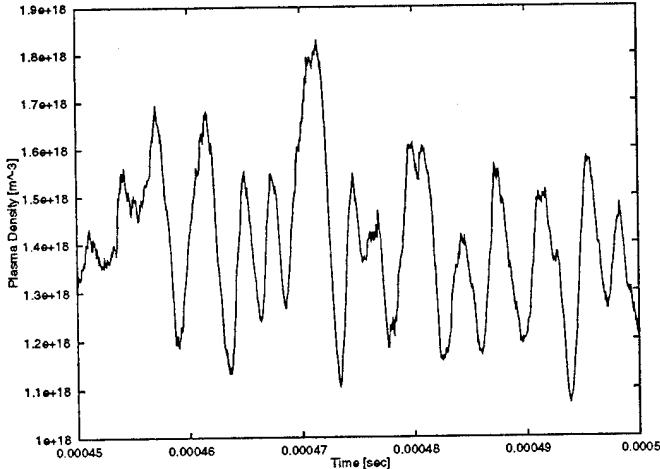
Figure 16: Short time history of plasma density, n_i $[m^{-3}]$, at z = 1.9 cm and r = 3.6 cm.
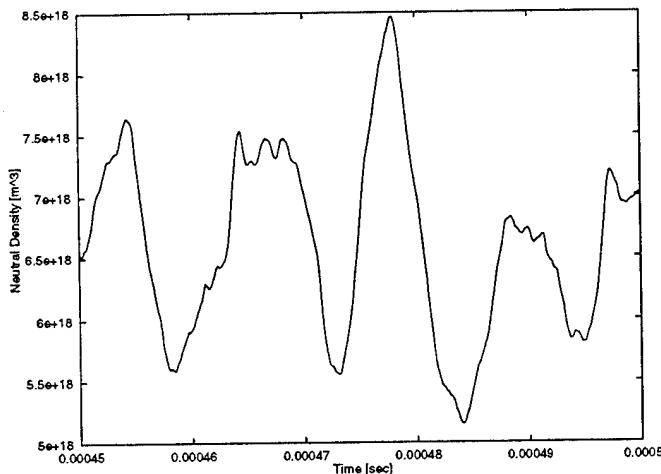

Figure 17: Short time history of neutral number density, n_n $[m^{-3}]$, at z = 1.9 cm and r = 3.6 cm.

on a slower signal which appears to be in the 80 kHz range. This corresponds roughly to the frequency of ions traversing the ionization region.

The high frequency oscillations visible in Figure 16 occur at a frequency of aproximately 300 kHz. The neutral density fluctuations in Figure 17 are at approximately 100 kHz. Both of these high frequency oscillations may be related to the time scale of ion and neutral passage across grid cells, as can be seen in Table 4.

Conclusions

The Hall thruster simulation accurately predicted the performance parameters for the Bishaev/Kim SPT. Efficiency and specific impulse were accurate to within 8%. Anode current and beam current were accurate to within 5%. The net torque on the device was also calculated, and was found to lie within the bounds of experimental measurement. This implies that the numerical model may be very useful in predicting the performance of alternative Hall thruster geometries.

To test the Bohm diffusion assumption, three cases with different Bohm diffusion constants were tried. Surprisingly, the most accurate fit was achieved with a Bohm diffusivity equal to its traditionally quoted value of $\frac{kT_e}{16B}$, even though this is regarded as a rough approximation only.

The two-dimensional numerical results followed similar trends as the experimental values. However, the simulation predicted higher ionization rate near the anode. Also, the electron temperature rise outside the channel was not seen in experimental results.

11

Total wall impingement current was close to the experimental value. Using the wall current density and an experimental sputtering yield, the wall erosion rate was calculated. Comparing this to experiments with the SPT-100, a close agreement was found.

Therefore, the numerical model was useful for predicting the performance parameters of the Bishaev/Kim SPT geometry. The two-dimensional results lacked close agreement with experiment, but were consistent with the numerical model. The usefulness of the simulation is in predicting the performance, wall erosion rate, and torque of prototype Hall thrusters, and as a tool for understanding the physics of the plasma acceleration process.

Further Work

Work in refining the diffusion model is underway. Experimental investigations of the Hall thruster plasma are needed, in order to generate detailed information about electron currents across and along magnetic field lines. This would allow tabulation of diffusion coefficients as a function of plasma parameters, and more accurate simulation of two-dimensional phenomena.

References

[1] Lentz, C. A., "Transient One Dimensional Numerical Simulation of Hall Thrusters", Massachusetts Institute of Technology, S.M. Thesis, 1993.

[2] Dugan, John V. and Sovie, Ronald J., "Volume Ion Production Costs in Tenuous Plasmas: A General Atom Theory and Detailed Results for Helium, Argon and Cesium," NASA TN D-4150.

[3] Fife, John M., Two-Dimensonal Hybrid Particle-In-Cell Modeling of Hall Thrusters, Master's Thesis, Massachusetts Institute of Technology, May 1995.

[4] Mitchner and Kruger, Partially Ionized Gasses, John Wiley & Sons, New York, 1973.

[5] Birdsall, C. K., and Langdon, A. B., Plasma Physics via Computer Simulation, IOP Publishing Ltd., Bristol, England, 1991.

[6] Bishaev, A. M., and Kim, V., "Local Plasma Properties in a Hall-Current Accelerator with an Extended Acceleration Zone," Soviet Physics, Technical Physics, 23(9):1055-1057, 1978.

[7] Kozubsky, K., "Disturbance Torques Generated by the Stationary Plasma Thruster", AIAA-93-2349, AIAA/SAE/ASME/ASEE 29th Joint Propulsion Conference and Exhibit, Monterrey, California, June 28-30, 1993.

[8] Manzella, David H., "Stationery Plasma Thruster Ion Velocity Distribution", AIAA-94-3141, 30th AIAA/ASME/SAE/ASEE Joint Propulsion Conference, Indianapolis, Indiana, June 27-29, 1994.

[9] Garner, C. E., et. al., "Cyclic Endurance Test of a SPT-100 Stationery Plasma Thruster," 3rd Russian-German Conference on Electric Propulsion Engines and Their Technical Applications, Stuttgart, Germany, July 1994.

[10] Abgaryan, V., et. al., "Calculation Analysis of the Erosion of the Discharge Chamber Walls and Their Contamination During Prolonged SPT Operation," AIAA/ASMA/SAE/ASEE 30th Jpoint Propulsion Conference and Exhibit, Indianapolis, Indiana, June 1994.
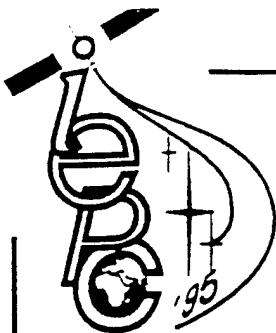
IEPC-95-236

A Study of Alkali-Seeded Hydrogen Arcjet Performance

Folusho Oyerokun and Manuel Martinez-Sanchez
Space Systems Laboratory
Massachussetts Institute of Technology
Cambridge, MA, USA

A Study Of Alkali- Seeded Hydrogen Arcjet Performance

Folusho Oyerokun and Manuel Martinez-Sanchez
Massachusetts Institute of Technology
Cambridge, MA (USA)

A model is developed to assess the feasibility of reducing the frozen losses in a hydrogen arcjet by adding very small amounts of easily ionizable cesium vapor. It is found that, within reasonable constraints on the constrictor geometry, and without allowing the electron temperature to exceed about 7000K, both the ionization and the hydrogen dissociation losses can be essentially eliminated, and a specific impulse of about 850 seconds can be obtained. The cesium mass fraction in the propellant is about 2%.

Introduction.

Frozen losses appear to be inextricably tied to the operation of Electric Propulsion devices: achieving a sufficient ionization of the gas already necessitates the expenditure of the ionization energy as a minimum. In reality, there is also a certain amount of excitation energy radiated away (in low pressure devices), and, of interest to arcjets, which tend to operate with molecular gases, of dissociation energy as well. Only a small fraction of these energy investments is recovered in the expansion nozzle.

An example from the modeling work of Ref[1] on a radiation-cooled hydrogen arcjet operating at .1 g/sec flow rate, 1.2 atm chamber pressure, 100 A current and 11.5 kw power, shows the magnitude of the problem: 17.5% of the exit plane energy flux is in the form of ionization energy, and 30% in the form of dissociation energy. Including thermal energy, this leaves only 39% for the flow kinetic energy. While details vary, this is typical of many other arcjets.

A more subtle form of inefficiency is associated with the extreme nonuniformity of the enthalpy distribution in an arcjet nozzle: the flow of total enthalpy H of an ideal gas out of the chamber is $\int H d\dot{m}$ while that of momentum after full expansion is $\int \sqrt{2H} d\dot{m}$. Thus, with no other losses, the best possible efficiency is

$$\eta = \frac{(\int \sqrt{2H} d\dot{m})^2}{2(\int d\dot{m})(\int H d\dot{m})}$$

which is always less than unity, the more so the less uniformly H is distributed over the flow.

Addition of a very small amount of an alkali (probably cesium) to the hydrogen gas in an arcjet can have a dramatic influence on the operating regime of the device, and contribute to the solution of both of the problems mentioned. Since cesium in a mole fraction of a few times 10^{-4} will be fully ionized at electron temperatures no higher than about 4000 K, the gas can have an adequate electrical conductivity without the hydrogen ever getting ionized. In addition, significant thermal nonequilibrium can develop, so that the gas can be even cooler than the electron gas, and hydrogen dissociation can also be largely avoided . This is limited, of course, by the need for a gas temperature high enough for an attractive specific impulse; however, as this work will show, specific impulses up to 850 sec. can be easily be obtained with minimal frozen losses. The enthalpy distribution is also much less nonuniform than in the classical constricted arc. This is because of the full ionization of the seed (cesium), which minimizes the electrothermal instability responsible for constriction.

The resulting operating condition bears some resemblance to that of a hydrogen resistojet, where frozen losses are also minimized by staying at a moderate gas temperature. The difference is that, while resistojet walls need to be hotter than the gas itself, the reverse is true in the seeded arcjet. Achieving a specific impulse of 850 sec in a resistojet would require at a minimum a heater wall temperature of about 2300 K, which, with current metallurgical limits, precludes long term operation.

We present in this paper a preliminary study of the performance potential of the seeded hydrogen arcjet. The model is quasi one-dimensional and inviscid, and no attention has been paid to near-electrode effects. The nozzle flow is simply assumed frozen isentropic. We do account, however, for the main effects in the constrictor, and are able to explore the practical limits of the operational domain.

Gas physics

The species accounted for by the model are H_2, H, Cs, Cs^+ and e. The electron temperature is kept low so as to exclude the presence of H^+ and H_2^+. Strong coupling is assumed between the ions and the neutrals, designated together as the heavy species. This implies equal temperatures and velocities (except for ambipolar diffusion). The electrons are assumed to be in Saha equilibrium with cesium atoms and ions

$$\frac{n_e n_{Cs^+}}{n_{Cs}} = 2 \frac{g_{Cs^+}}{g_{Cs}} \left(\frac{2\pi m_e k T_e}{h^2} \right)^{\frac{3}{2}} e^{-\frac{\varepsilon_i}{kT_e}} \tag{1}$$

2

where n_s and g_s refer to the number density and degeneracy of species s respectively, m_e is electron mass, h is the Planck constant, k is the Boltzmann constant, and ε_i is the ionization potential for cesium. The assumption of Saha equilibrium implies that electron collisional processes dominate over radiative processes. This is true whenever the alternative coronal balance model would predict higher values of (n_e^2 / n_{Cs}), which, using Cs rate data in Ref[2], would occur below approxiately $n_e = 2 \times 10^{19} m^{-3}$. Our electron densities are generally two orders of magnitude above this limit. For the electron temperatures of this problem, in turn, Saha's equation almost invariably predicts full ionization.

Chemical equilibrium is also assumed to prevail between hydrogen molecules and atoms, $\dfrac{n_H^2}{n_{H_2}} = K_n(T)$ where $K_n(T)$ is the equilibrium constant and can be found from thermodynamic tabulations [3]. The electron temperature is obtained from the electron energy equation

$$\sigma E^2 = 3 \frac{m_e}{m_H} \delta n_e \nu_e k (T_e - T) \tag{2}$$

where σ is the electrical conductivity, E is the electic field, $\delta(T_e)$ is the inelastic correction factor, ν_e is electron collision frequency with the heavy species

$$\nu_e = \nu_{eH_2} + \nu_{eH} + \nu_{ei}$$

The collision frequency between electrons and cesium atom is negligible.

The neglect of radiative losses in Eq (2) and elsewhere is motivated by the near full ionization of the seed, since Cs ions and hydrgen molecules would be only weakly excited at the electron temperatures (under .6 eV) found here.

Equation (2) can be rearranged as

$$\left(\frac{T_e}{T_H}\right)^2 - \frac{T_e}{T_H} - \frac{E^2/p^2}{8.00 \times 10^{34} \delta_{H_2} f_1 f_2} = 0 \tag{3}$$

where f_1 and f_2 depend on the ratio of the cross sections and are of order unity. The above equation is then solved iteratively to obtain Te.

Due to its low mole fraction, the effect of the seed element on thermal conductivity, enthalpy and density is negligible. The electrical conductivity is independent of pressure, because both, the electron density (nearly equal to the seed density), and the collision frequency, are proportional to pressure; the conductivity is, of course, proportional to the seed fraction.

Governing Equations

The model treats a quasi one-dimensional inviscid constrictor flow, coupled with a radial (Elenbaas-Heller) diffusion equation, modified to allow convective energy transport. The overall conservation laws are

$$\frac{d}{dx}\int_0^R 2\pi r \rho u \, dr = 0 \tag{4}$$

$$\frac{d}{dx}\left(\rho u^2 A\right) + A\frac{dp}{dx} = 0 \tag{5}$$

$$\rho u \frac{\partial h_t}{\partial x} = \frac{1}{r}\frac{\partial}{\partial r}\left(r\frac{\partial \varphi}{\partial r}\right) + \sigma E^2 \tag{6}$$

$$\frac{d}{dx}\int_0^R 2\pi r \sigma E \, dr = 0 \tag{7}$$

where $A = \pi R^2$ is the constrictor cross section, h_t is the total enthalpy, $\varphi = \int_0^T K_{eff}(T')dT'$ is the heat flux potential. Here, K_{eff} is the effective thermal conductivity, which includes diffusive transport of heats of reaction. The axial electric field is calculated from Ohm's law ,

$$E = \frac{I}{\int_0^R 2\pi r \sigma \, dr}$$

The governing equations can be simplified if the pressure, momentum flux, $q = \rho u^2$, and electric field are assumed to be radially uniform. Expressing all other functions in terms of T and P, after algebraic manipulation, the governing equations reduce to

$$\frac{\partial h_t}{\partial x} = \frac{1}{\sqrt{q\rho}}\left[\frac{1}{r}\frac{\partial}{\partial r}\left(r\frac{\partial \varphi}{\partial r}\right) + \sigma E^2\right] \tag{8}$$

$$\frac{dp}{dx} = \frac{\displaystyle\int_0^R \frac{r}{\beta\sqrt{\rho}}\left(\frac{\partial \rho}{\partial T}\right)_p \frac{\partial h_t}{\partial x}\, dr}{\displaystyle\frac{1}{q}\int_0^R r\sqrt{\rho}\, dr - \int_0^R \frac{r}{\sqrt{\rho}}\left[\frac{\alpha}{\beta}\left(\frac{\partial \rho}{\partial T}\right)_p + \left(\frac{\partial \rho}{\partial p}\right)_T\right]dr} \tag{9}$$

4

$$\frac{\partial T}{\partial x} = \frac{\frac{\partial h_t}{\partial x} + \alpha \frac{dp}{dx}}{\beta} \tag{10}$$

$$\frac{dE}{dx} = -\frac{E \int_0^R r\left[\left(\frac{\partial \sigma}{\partial T}\right)_P \frac{\partial T}{\partial x} + \left(\frac{\partial \sigma}{\partial p}\right)_T \frac{dp}{dx}\right]dr}{\int_0^R r\sigma dr} \tag{11}$$

where

$$\alpha = \frac{1}{2\rho} - \left(\frac{\partial h}{\partial p}\right)_T + \frac{q}{2\rho^2}\left(\frac{\partial \rho}{\partial p}\right)_T , \quad \beta = \left(\frac{\partial h}{\partial T}\right)_P + \frac{q}{2\rho^2}\left(\frac{\partial \rho}{\partial T}\right)_P$$

These coupled ordinary differential equations are then integrated downstream from given initial and boundary conditions, until the flow becomes choked. The choking point is taken to be the end of the constrictor, as well as the arc attachment point.

Method of Solution

The simplified governing equations are solved for a fixed constrictor geometry, seed fraction and current. At the inlet, the pressure, Mach number and a gaussian-like temperature profile with the peak at the arc core are prescribed. An insulating boundary condition is specified at the walls. Other variables at inlet are then computed using the above information.

At every axial station, $\frac{\partial h_t}{\partial x}(r)$ in equation (8) is computed as

$$\left(\frac{\partial h_t}{\partial x}\right)_i = \frac{1}{\sqrt{q\rho_i}}\left[\frac{r_{i+\frac{1}{2}}(\varphi_{i+1} - \varphi_i) - r_{i-\frac{1}{2}}(\varphi_i - \varphi_{i-1})}{r_i \Delta r^2} + \sigma_i E^2\right] \tag{12}$$

Subtituting this into equation (9) and integrating along the radial direction using Simpson's method, $\frac{dp}{dx}$ can be obtained. This, along with $\frac{\partial h_t}{\partial x}$, is used to determine $\frac{\partial T}{\partial x}$, which then is used to determine $\frac{dE}{dx}$. The step size is determined by local stability and accuracy. Once P, T and E have been determined at one grid point, enthalpy and other variables can be computed as well. The above steps are then repeated until sonic conditions are reached. Arc attachment is assumed to occur at the constrictor exit.

Thrust and specific impulse for a frozen nozzle expansion can be calculated as

$$F = C_{th} P_{t_{throat}} A \tag{13}$$

5

$$I_{sp} = \frac{F}{\dot{m}g} \qquad (14)$$

where the thrust coefficient, $C_{th} = 1.8$ ($\gamma = 1.3$ and $M_{exit} = 5$), and $P_{t_{throat}}$ is the stagnation pressure at the sonic point. The frozen losses are defined as

$$E_{frozen} = n_H \varepsilon_d c A \qquad (15)$$

where $\varepsilon_d = 4.478 eV (7.174 \times 10^{-19} J)$ is the the dissociation energy of hydrogen, and c is the exit gas velocity.

Discussion of Results

The model has been used for an exploration of performance in the neighborhood of 10 kw power. After some heuristic optimization, a nominal case was selected, with the following characteristics:

$P_0 = 3.3 atm;$ Molar Seed Fraction = 0.0003;   I=17 A

Constrictor Radius=1.4 mm;   Constrictor inlet Mach No.=0.22

The inlet temperature of the gas was assumed to be 400K at the walls, rising to 3500 K at the cathode tip (of radius 0.35 mm) , with an approximate average of 500 K. After the constrictor, the nozzle was assumed to expand the gas to a Mach number of 5, with a ratio of specific heats of 1.3.

The nominal case was found to give these results:

$\dot{m} = 0.369 g / s$ V=595 Volt;   Power=10.1 kw

$I_{sp} = 835 sec;$ Frozen losses=1%;   Constrictor L/D=8.7

$T_e = 6800 K$ (Maximum)

Computations were then made in a parametric fashion, varying only one of the major parameters at a time (seed fraction, chamber pressure, current and inlet Mach no.), while keeping all else constant. The results are shown in Figures (1) through (8).

Most of the trends shown by these numerical results can be understood with reference to a simple model of heat addition to a gas in a constant area duct. The conservation equations for this situation, written between the duct inlet and its <u>choked</u>

6

exit, are

$$\rho_* u_* = \rho_0 u_0 \approx \sqrt{\frac{\gamma}{R_g T_{t0}}} P_{t0} M_0 \qquad (16)$$

$$P_* + \rho_* u_*^2 = P_0 + \rho_0 u_0^2 \approx P_{t0} \qquad (17)$$

$$c_p T_* + \frac{1}{2} u_*^2 = c_p (T_{t0} + \Delta T_t) \qquad (18)$$

In addition we must have $u_*^2 = \gamma R_g T_*$ and $P_* / \rho_* = R_g T_*$. The approximations in the right side of Eqs. (16) to (18) are valid for small M_0. Solving the above system for ΔT_t, we find

$$\frac{\Delta T_t}{T_{t0}} = \frac{1}{2(\gamma + 1)M_0^2} - 1 \qquad (19)$$

which shows that the exit total temperature is proportional to the inlet temperature, divided by the square of the inlet Mach number . Since the thruster specific impulse scales as the square root of T_{t*}, we find that I_{sp} should vary as $1/M_0$, and be independent of the other parameters. This is confirmed by the results in Figs. (1) to (8).

The overall power balance for the heated flow is $VI = \dot{m} \Delta h_t$, which can be rewritten as

$$V = \frac{\rho u \Delta h_t}{I / A} \qquad (20)$$

With reference to Eq (19), we see that the voltage must scale as the quantity

$$\frac{P_{t0}}{I / A} \left(\frac{1}{2(\gamma + 1)M_0} - M_0 \right) \qquad (21)$$

which is also confirmed by the numerical results. In particular, as Fig (2) illustrates, V is independent of seed fraction.

We now note that the voltage equals the mean axial field, times the constrictor length L, and, using Ohm's law, $V = \frac{I / A}{\sigma} L$. Since the conductivity is proportional to seed fraction and independent of pressure, we conclude that the constrictor length must scale as the quantity

$$\frac{P_{t0}}{(I / A)^2} s \left(\frac{1}{2(\gamma + 1)M_0} - M_0 \right) \qquad (22)$$

where s is the seed fraction. There is also some dependence of σ on the electron temperature, which complicates things somewhat, but this scaling is approximately validated by the figures as well.

Finally, it can be verified that the middle term in the quadratic Eq(3) for the electron temperature is relatively small, showing that, to a first approximation, T_e is simply proportional to the ratio E/P of field to pressure. Noting that E is $(I / A) / \sigma$, we find an approximate scaling of the electron temperature with

$(I/A)T_{t0}/(sP_{t0}M_0^2)$. The dependencies on current and pressure are verified by Figs (4) and (5). Those on seed fraction and inlet Mach number are present in the results, but, due to the approximations made in this discussion, are weaker than found here.

An important observation to be made is that, since the exit gas temperature depends only on M_0, and the frozen losses are found to correspond mostly to dissociation (which is governed by this temperature), these losses will become large below some critical value of the inlet Mach number. Fig. (8) shows that this happens below $M_0 \approx 0.21$ for our conditions. It is to be noted also that, simultaneously, the channel length is becoming excessive (L/D>10, probably leading to excessive viscous losses) as M_0 is reduced, and so is the electron temperature ($T_e \geq 7000K$, probably initiating ionization of the molecular hydrogen). Increasing pressure can alleviate the electron temperature rise (Fig (4)), but it also aggravates the L/D problem. On the other hand, reducing seeed fraction (Figs (1) and (2)) has the opposite effects of alleviating the L/D problem while elevating the electron temperature further. This combination of effects limits the specific impulse (Fig (8)) to values not much higher than that for the baseline case.

Some sense of the two-dimensional degree of nonuniformity of the gas in the constrictor can be obtained from Figs. (9) and (10), which show contours of T_e and T_g for the nominal case. As noted in the Introduction, there is much less arc constriction than in a conventional arcjet. Absent from the calculation are the wall boundary layers which would in actuality provide a thin transition to the wall temperature.

Summary and Conclusions

The results of the simplified model presented here suggest that cesium seeding of a hydrogen arcjet is a feasible approach towards minimizing frozen losses and increasing the efficiency, while maintaining an attractive specific impulse. At the same time, the generally reduced temperature levels should lead to fewer lifetime problems, and the presence of the easily ionizable alkali should also reduce near-electrode losses (although these aspects have not been analyzed).

These beneficial features are to be traded off against the added operational complexities brought about by the presence of the cesium. These include the cesium dispensing system, for which precedents , including flight proven designs, already exist, and plume contamination concerns. The latter may be important in some applications, although it is to be noted that a mole fraction of 3×10^{-4} in hydrogen is equivalent to a 2% cesium mass fraction only, which may begin to approach the contamination levels due to electrode erosion in other types of thrusters.

In view of these results, it is recommended that more detailed theoretical design studies be pursued, and that plans be made for experimental work in this area.

References

[1] Miller, Scott A.. Multifluid Nonequilibrium Simulation of Arcjet Thrusters. Sc. D. Thesis, MIT, Feb. 1994. Also to apear in the AIAA J. of Prop., 1995

[2] M. Mitchner and C.H. Kruger, Jr. Partially Ionized Gases. John Wiley & Sons, 1973

[3] G.J. Van Wylen and R.E. Sonntag, Fundamentals of Classical Thermodynamics, SI Version. John Wiley & Sons, 1978

Acknowledgement
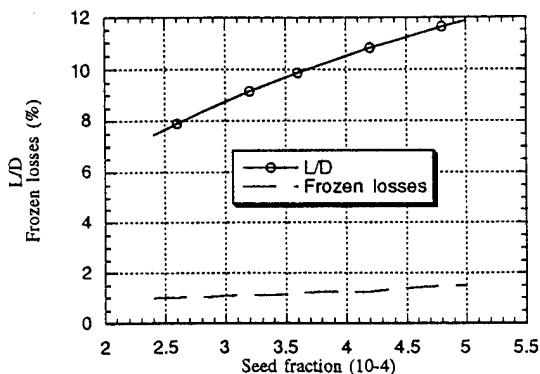
Fig. 1 L/D, Frozen losses vs. Seed fraction

Fig. 2 Electron temperature, specific impulse and arc voltage vs. seed fraction



Fig. 3 Frozen loses, L/D vs. total pressure

Fig. 4 Electron temperature, arc voltage and specific impulse vs. total pressure
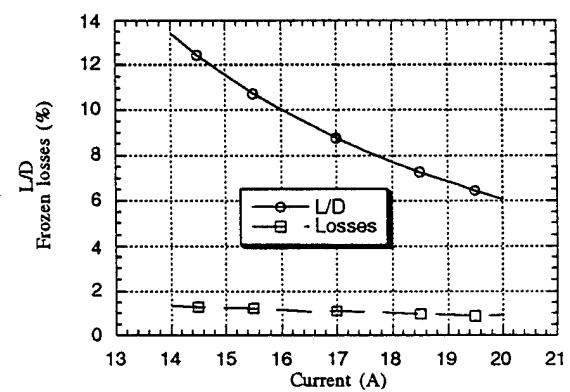
Fig. 5 L/D, frozen losses vs. current
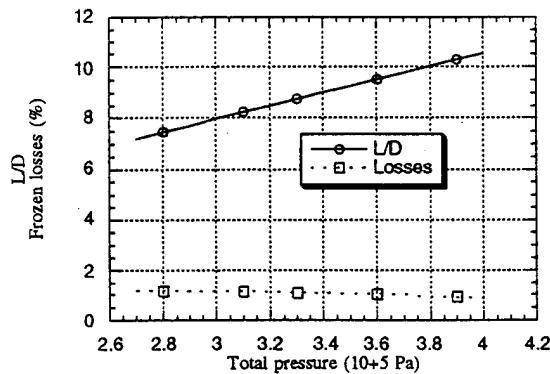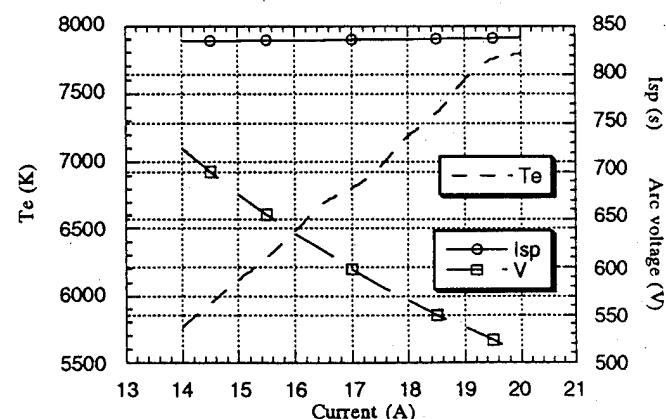
Fig. 6 Electron temperature, specific impulse and arc voltage vs. current
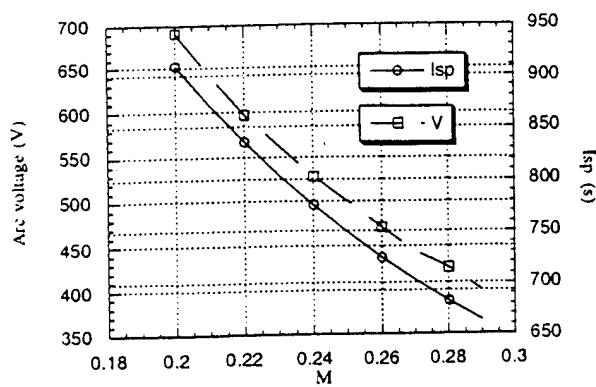
Fig. 7 Specific impulse, arc voltage vs. inlet Mach number
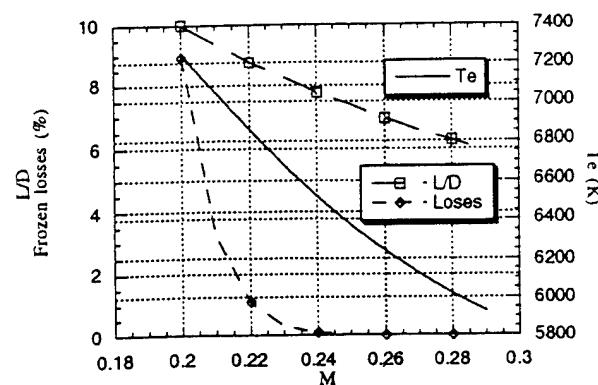
Fig. 8 Electron temperature, L/D and frozen losses vs. inlet Mach number

Level	Tgas
F	3306.25
E	3112.5
D	2918.75
C	2725
B	2531.25
A	2337.5
9	2143.75
8	1950
7	1756.25
6	1562.5
5	1368.75
4	1175
3	981.25
2	787.5
1	593.75
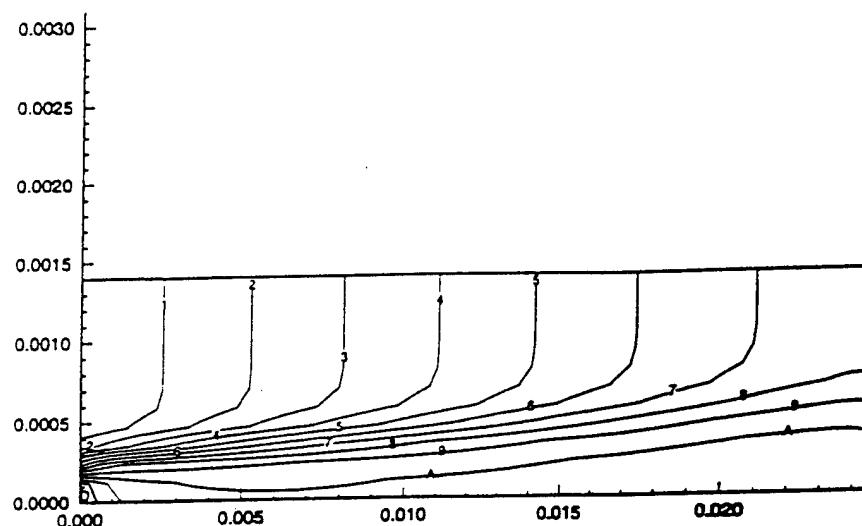
Fig. 9 Gas temperature contour plot
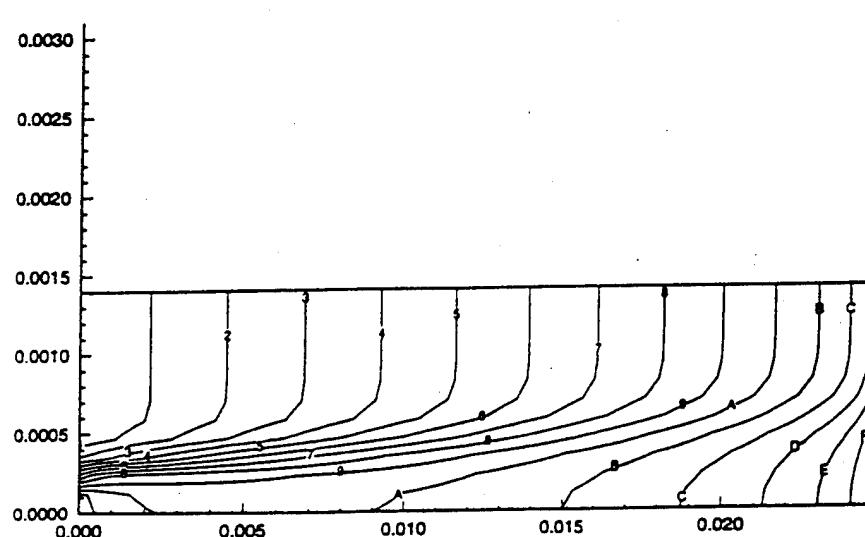
Level	Te
F	6428.29
E	6064.34
D	5700.4
C	5336.46
B	4972.52
A	4608.58
9	4244.63
8	3880.69
7	3516.75
6	3152.81
5	2788.86
4	2424.92
3	2060.98
2	1697.04
1	1333.1

Fig. 10 Electron temperature contour plot

AIAA-94-3342
IONIZATIONAL IGNITION IN ATOMIC SELF-FIELD MPD THRUSTER FLOWS

E. J. Sheppard
Aerospace Science Engineering Department
Tuskegee University
Tuskegee, Alabama

M. Martinez-Sanchez
Department of Aeronautics and Astronautics
Massachusetts Institute of Technology
Cambridge, Massachusetts

30th AIAA/ASME/SAE/ASEE Joint Propulsion Conference
June 27-29, 1994 / Indianapolis, IN

inlet wall. This makes the wall boundary condition a critical ignition factor. This problem has been considered in other works as well, many of which did not consider the details of the ionizing region. Such models may yield significant results, but are not capable of looking into failure modes, i.e., nonignition. These authors [7], [8] have previously addressed constant and varying temperature models with constant speed as well as acceleration, and a local energy balance model with accelerating flow. Burton [2] considered a finite thermal conductivity model, and included some radiation effects, with constant bulk speed, and supersonic injection. The supersonic inlet assumption essentially erases any possible effect that back-diffusion may have on inlet ionization, so that this should be considered as work of similar direction, but in different regimes.

This paper extends work which focuses on the role that an upstream flux of charged particles may have on the gas-plasma transition at the inlet of a magnetoplasmadynamic thruster. The addition of an overall energy balance consideration to an accelerating plasma model makes the results self-consistent.

2   Inlet Flow Model

This section will present the basic equations of motion as well as details of the models used here for ion slip and electrical conductivity. Section 3 will consider ignition in an accelerating flow.

We will consider injection of atomic argon into the thruster channel through a porous backplate to ensure 1-D bulk flow. Figure 1 shows the general configuration of the inlet ionizing region (a constant area channel of width w out of the page; the area may change outside of this region). Since the hypothesis of this work is that back-diffusion of electron-ion pairs sustains ignition, the characteristic scale length of the ionization region is expected to be the back diffusion length, l_D, defined below.
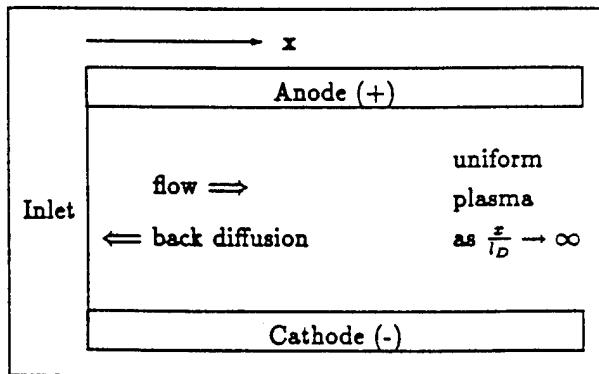

Figure 1: 1-D Thruster Inlet Region

2.1   Equations of Motion

The steady state, quasi-one dimensional equations of motion for this configuration are overall and electron continuity, overall momentum, electron energy, and a magnetic field equation. The equations used are a simplified version of the 1-D equations of Niewood [5].

The overall continuity equation is,

$$(n_e + n_a)u = n_g u = G = \frac{\dot{m}}{Am_i} \qquad (1)$$

where n_g is the total number density of of nuclei, n_a is the number density of atoms, and n_e is the number density of electrons. The mass flow rate is $\dot{m}$, the channel area is A, and the nucleus mass is m_i. Since this is a quasi-neutral plasma, and only singly ionized specie may exist, $n_e = n_i$, where n_i is the number density of the ions. The ion continuity equation is

$$\frac{dn_e u}{dx} = -\frac{dn_e V_i}{dx} - \frac{D_a n_e}{h^2} + \dot{n}_e \qquad (2)$$

In equation 2, the transverse ambipolar diffusion, $\frac{D_a n_e}{h^2}$, is included (with an assumed parabolic distribution of n_e in the transverse direction so that h is actually $\frac{1}{\sqrt{12}}$ of the actual channel height, $H \approx 0.02m$.) in order to allow a balance to be struck far downstream of the ionization layer. The rate equation for production of ion electron pairs, $\dot{n}_e$, is

$$\dot{n}_e = n_e n_a S_{ac} - n_e^2 n_i S_{ca}$$

where S_{ac} and S_{ca} are the overall ionization and overall three body recombination coefficients, respectively. Values for these are given in references [7] and [8], and for argon,

$$S_{ca} = 8.25 \times 10^{-43} \exp\left(\frac{(\ln(\frac{T_e}{1000}) - 3.95)^2}{0.6144}\right) \frac{m^6}{s}$$

The integrated total momentum equation, including pressure and magnetic (Lorenz) forces and neglecting friction, is

$$m_i n_g u^2 + p + \frac{B_z^2}{2\mu_o} = F \qquad (3)$$

and the electron energy equation, including axial heat conduction, Ohmic heating, and energy loss due to the endothermic ionization process, and neglecting both pressure work and transverse heat conduction, is

$$\frac{3}{2} k_B \frac{dn_g u \alpha T_e}{dx} = -\frac{d}{dx}\left(K_e \frac{dT_e}{dx}\right) + \frac{j^2}{\sigma} - E_{ai} \dot{n}_e \quad (4)$$

and the magnetic field is governed by the following equation

which is solved analytically into the channel and to the throat. The ionization zone is found to be entirely embedded in the magnetic diffusion layer, and consists of an inner layer, near the wall, where ambipolar diffusion is significant, and an outer layer, where diffusion plays no significant role. The first subsection following describes the model, and the second presents results.

3.1 Formulation

We start with $G = \frac{\dot{m}}{m_i A_t} = $ constant in the constant area ionization zone. The differential form of the momentum equation (3) is used:

$$m_i G \frac{du}{dx} = \frac{d}{dx}\left[p + \frac{B^2}{2\mu_o} \right] \quad (12)$$

where the pressure for a two temperature, electrically neutral plasma is

$$p = m_i n_s v_B^2 (\alpha + (1-\alpha)\theta) \quad (13)$$

Here, because of the acceleration, the alternative version for the ion slip flux is used, so that, from equation 9, we can define the flux, $\Gamma = -n_e V_i$, from

$$\frac{d\alpha}{dx} = \frac{\Gamma}{C_a \theta} + (1-\alpha)\left(\frac{u^2}{\theta v_B^2} - 1\right)\frac{1}{u}\frac{du}{dx} \quad (14)$$

This equation, along with the following three, constitute the equations of motion for the quasi-one-dimensional isothermal flow problem. Starting with equation 12, and using equations 13, 14, the momentum equation becomes [6]

$$\frac{du}{dx} = \frac{-\frac{v_B^2(1-\theta)\Gamma}{C_a u} + \frac{\theta B}{m_i G}\sigma(E - uB)}{1 - \alpha(1-\theta) - \frac{\theta v_B^2}{u^2}} \quad (15)$$

Equation 2 may be rewritten as:

$$\frac{d\Gamma}{dx} = G\frac{d\alpha}{dx} + \frac{C_a \alpha}{h^2} - S_{ai} n_s^2 \alpha(1-\alpha) \quad (16)$$

and the final equation is the magnetic field equation, equation 5.

Nondimensionalizing these equations will allow us to analyse them parametrically. Defining reference values $u_{ref} = \frac{B_o^2}{2\mu_o m_i G}$, and $l_{ref} = \Lambda_m = \frac{1}{\mu_o \sigma u_{ref}}$, then the new variables are $\bar{u} = \frac{u}{u_{ref}}$, $\gamma = \frac{\Gamma}{G}$, $b = \frac{B}{B_o}$, $\bar{E} = E/(u_{ref}b_o)$ and $\xi = \frac{x}{\Lambda_m}$. The resulting nondimensional equations of motion are:

$$\frac{d\bar{u}}{d\xi} = \frac{-\frac{\beta(1-\theta)\gamma}{\epsilon_D \bar{u}} + \frac{2\theta b}{f}}{1 - \alpha(1-\theta) - \frac{\theta\beta}{\bar{u}^2}} \quad (17)$$

$$\frac{d\alpha}{d\xi} = \frac{\gamma}{\epsilon_D \theta} + (1-\alpha)\left(\frac{\bar{u}^2}{\theta\beta} - 1\right)\frac{1}{\bar{u}}\frac{d\bar{u}}{d\xi} \quad (18)$$

$$\frac{d\gamma}{d\xi} = \frac{d\alpha}{d\xi} + \alpha\left(\epsilon_w - \frac{\lambda(1-\alpha)}{\bar{u}^2}\right) \quad (19)$$

$$\frac{db}{d\xi} = -\frac{\bar{E} - \bar{u}b}{1 + (\frac{1}{\alpha} - 1)q} \quad (20)$$

where for convenience we define

$$f = \frac{1 + (\frac{1}{\alpha} - 1)q}{\bar{E} - \bar{u}b} = -\left(\frac{db}{d\xi}\right)^{-1}$$

In addition to the parameters defined previously,

$$\beta = \frac{v_B^2}{u_{ref}^2}$$

$$\epsilon_D = \frac{(C_a)\mu_o \sigma_{ref} u_{ref}}{G} \approx \frac{(l_d)_{\parallel}}{\Lambda_m}$$

$$\lambda = \frac{S_{ai}G}{u_{ref}^2 \mu_o \sigma_{ref}} \approx \frac{\Lambda_m}{L_{ai}}$$

$$\epsilon_w = \frac{C_a \Lambda_m}{Gh^2}$$

The first far downstream ($\xi \to \infty$) boundary condition will be that $\bar{E} = \bar{u}b$, which implies an infinite length and hence an infinite magnetic Reynolds number. This motivates us to choose the magnetic field itself as the independent variable. Dividing the three other equations of motion (17, 18, 19) by equation 20, we arrive at the following set of equations:

$$\frac{d\bar{u}}{db} = \frac{f\beta(1-\theta)\frac{\gamma}{\epsilon_D \bar{u}} - 2\theta b}{1 - \alpha(1-\theta) - \frac{\theta\beta}{\bar{u}^2}} \quad (21)$$

$$\frac{d\alpha}{db} = -f\frac{\gamma}{\epsilon_D \theta} + (1-\alpha)\left(\frac{\bar{u}^2}{\theta\beta} - 1\right)\frac{1}{\bar{u}}\frac{d\bar{u}}{db} \quad (22)$$

$$\frac{d\gamma}{db} = \frac{d\alpha}{db} - f\alpha\left(\epsilon_w - \frac{\lambda(1-\alpha)}{\bar{u}^2}\right) \quad (23)$$

The second downstream (∞) boundary condition is the same balance between transverse ambipolar diffusion and ionization used in the constant speed case, which is now:

$$1 - \alpha_\infty = \frac{C_a u_\infty^2}{S_{ion}G^2 h^2} = \frac{\epsilon_w \bar{u}_\infty^2}{\lambda} \quad (24)$$

Additional boundary conditions are the conditions at the injector wall, and the internal boundary conditions at the sonic passage point. The injector wall condition is critical: the ions (moving at a velocity equal to the average velocity plus the ion slip velocity) must reach the sheath at the inlet wall at the Bohm velocity *moving upstream against the bulk flow*:

$$n_e(u + V_i) = -n_e v_B$$

4

approaches that of the magnetic scale ($\xi \approx 1$), At higher λ, the ionizing scale is decidedly smaller than the magnetic scale, approaching $\xi \approx \epsilon_D$. As found with the constant speed case, again higher λ yields a higher α_o.
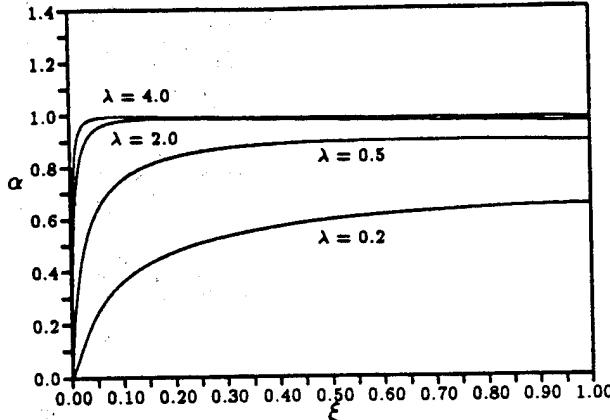

Figure 3: Ionization fraction α vs ξ for the "standard" parameters, except for varying λ.

Using equation 13 in the integrated momentum equation (equation 3), and with constant $G = n_g u$ in the ionization zone, and using the nondimensional variables and parameters defined above,

$$\bar{u} + \frac{\beta(\alpha + (1-\alpha)\theta)}{\bar{u}} + b^2 = \frac{F}{m_i G u_{ref}} \qquad (29)$$

For small ("subsonic") speeds, $\bar{u}^2 \ll \beta(\alpha + (1-\alpha)\theta)$, the acceleration comes mostly from the pressure gradient (which is strongly dependent on the gradient of α in this model), so that

$$\frac{\beta(\alpha + (1-\alpha)\theta)}{\bar{u}} \approx \frac{F}{m_i G u_{ref}} \qquad (30)$$

which depends strongly on the value of λ. For large $\bar{u}$ ("supersonic"), the acceleration comes chiefly from the changing magnetic field:

$$\bar{u} + b^2 \approx \frac{F}{m_i G u_{ref}} \qquad (31)$$

which does not depend very strongly on λ so long as the entire ionization region is Coulomb dominated.

3.3 Overall Energy Balance

In reality, the electron temperature, and therefore the parameters of the problem (namely λ, will be functions of the expansion ratio. This means that, for fixed channel throat dimensions and flow rate, there may be only one possible λ for each expansion ratio. This is required by the energy balance in the ionization zone. Adding an energy balance to this model

therefore makes it self-consistent and will indicate a more definite ignition criterion.

Assuming infinite thermal conductivity, which implies a constant electron temperature, and is consistent with the constant temperature assumption made previously, the integrated energy equation, as reported by Lawless and Subramanian [3] is

$$m_i G \left[h + \frac{u^2}{2} \right] + \frac{EB}{\mu_o} = C$$

which is valid for the constant area region assumed for the ionization-acceleration zone. C is a constant of the flow, and the enthalpy, h, is defined as

$$h = \alpha \left(\frac{5}{2} \frac{k_B T_e}{m_i} + \frac{e V_i}{m_i} \right)$$

for frozen heavy species temperature, T_g. The energy balance, for constant temperature, and using the nondimensional variables and parameters, is now:

$$2\bar{E}(1 - b_\infty) = (\alpha_\infty - \alpha_o) \left(\frac{5}{2}\beta(1-\theta) + \delta \right) + \frac{1}{2}(\bar{u}_\infty^2 - \bar{u}_o^2)$$

where

$$\delta \equiv \frac{e V_i}{m_i u_{ref}^2}$$

and $\delta = 0.59$ for the argon atom, and the u_{ref} defined here. This depends on conditions, of course. In fact, $\delta \to 1$ is a rough onset criteria; i.e., the flow kinetic energy approaches the ionization potential energy of the atom.

If $\alpha_\infty \gg \alpha_o$, and $\bar{u}_\infty \gg \bar{u}_o$, which has been generally found in the results of the accelerating ignition model, then

$$2\bar{E}(1 - b_\infty) = \alpha_\infty \left(\frac{5}{2}\beta(1-\theta) + \delta \right) + \frac{\bar{u}_\infty^2}{2}$$

Since, from the far-downstream condition,

$$\alpha_\infty = 1 - \frac{\epsilon_w \bar{u}_\infty^2}{\lambda}$$

and $\bar{u}_\infty = \bar{E}/b_\infty$

$$2\bar{E}(1 - b_\infty) = \left(1 - \frac{\epsilon_w \bar{E}^2}{\lambda b_\infty^2} \right) \left(\frac{5}{2}\beta(1-\theta) + \delta \right) + \frac{1}{2}\frac{\bar{E}^2}{b_\infty^2}$$

or, rearranging,

$$2\bar{E}(1 - b_\infty) - \frac{1}{2}\frac{\bar{E}^2}{b_\infty^2} = \left(1 - \frac{\epsilon_w \bar{E}^2}{\lambda b_\infty^2} \right) \left(\frac{5}{2}\beta(1-\theta) + \delta \right)$$

Which is now a function of the temperature-dependent parameters, and the $(\bar{E}, b_\infty)$ solution pair. This condition sets the electron temperature, and an

IEPC

IEPC-93-071
Ionization Rate Models and Inlet Ignition in Self-Field MPD Thrusters

E. Sheppard and M. Martinez-Sanchez
Space Power and Propulsion Laboratory
Massachusetts Institute of Technology
Cambridge, MA

AIAA • AIDAA • DGLR • JSASS

23rd International Electric Propulsion Conference

IONIZATION RATE MODELS AND INLET IGNITION IN SELF-FIELD MPD THRUSTERS

E. J. Sheppard*and M. Martinez-Sanchez†
Space Power and Propulsion Lab
Department of Aeronautics and Astronautics
Massachusetts Institute of Technology
Cambridge, MA 02139, U.S.A.‡

Abstract

An overall ionization rate model has been developed which takes into account the detailed effects of processes involving excited states, and which may be used in a variety of flow models. The resulting overall collisional rate coefficients for 3-body recombination are reported here for the argon atom and first ion, and for the hydrogen atom. The phenomenon of inlet ionizational ignition (steady state initiation of ionization) in self-field MPD thrusters has also been further analyzed and explained. The hypothesis that back diffusion could explain the mm-scale ionizing regions found in experiments has been tested in constant speed models of atomic injection (first without and then with variable temperature) along with an accelerating, subsonic atomic injection, constant temperature model, and can explain ignition over a range of conditions identified here.

Nomenclature

A channel area ($A = Hw$).
B magnetic field.
$\bar{c}$ a thermal speed.
C_a modified ambipolar coefficient $= D_a n_g$
D_a ambipolar diffusion coefficient.
e electron charge.
E electric field.
E_{ai} ionization potential energy.
G flow rate per unit area $= n_g u$.
H channel height.
h channel height/$\sqrt{12}$.
k_B Boltzmann constant.
l a scale length.
K_e electron thermal conductivity.

L thruster characteristic length.
Le Lewis number.
$\dot{m}$ mass flow rate $= m_i n_g u A$.
m particle mass.
n particle number density.
p pressure.
q critical value of α in conductivity equation.
R_m magnetic Reynolds number, $R_m = \mu \sigma u L$.
S_{jk} collisional rate coefficient, $j \to k$ transition.
T particle temperature (K).
u plasma bulk velocity.
V slip speed.
x streamwise coordinate.
α ionization fraction, $\alpha = \frac{n_e}{n_g}$.
β $= v_B^2 / u_m$.
Γ ion slip flux: $\Gamma = -n_e V_i$
θ the temperature ratio: $\frac{T_e}{T_e + T_g}$.
Λ_m magnetic interaction length.
σ scalar conductivity.
τ nondimensional electron temperature.
ϕ potential (voltage).

Subscripts/superscripts:

D diffusion.
e electrons.
g heavy gas species.
i ions.
o inlet.
s sonic passage.
t throat.
∞ far downstream asymptotic value
$*$ equilibrium value.

---

1 Introduction

The first section of this paper presents the results from a method of calculating overall recombination and ionization coefficients for both atomic and ionic species. Results are given for argon atoms and ions and for the hydrogen atom.

The rest of this paper focuses on the role that an upstream flux of charged particles may have on the gas-plasma transition at the inlet of a magnetoplasma-dynamic thruster. Steady-state "ignition" is defined here as the condition when this ionizing zone is fixed at the inlet wall, making the wall boundary condition a critical ignition factor.

This problem has been considered in other works as well, although the details of the ionizing zone are generally ignored. Such models do yield significant results, but are not capable of looking into failure modes, i.e., nonignition. These authors [7], [9] have previously addressed constant temperature models with constant speed as well as acceleration, and a local energy balance model with accelerating flow. Burton [2] considered a finite thermal conductivity model, and included some radiation effects, with constant bulk speed, and supersonic injection. The supersonic inlet assumption essentially erases any possible effect that back-diffusion may have on inlet ionization, so that this should be considered as work of similar direction, but in different regimes.

Three cases will be addressed here: atomic injection at constant speed with constant temperature and then varying temperature, and atomic injection with constant temperature and accelerating flow. All units herein are mks, and temperatures are in degrees Kelvin.

2   The Ionization Rate Model

This section extends the work reported by these authors previously on the subject of calculating overall ionization and recombination coefficients for atomic and ionic species. The formulation has been presented [8] and here results are given for the argon atom and ion and the hydrogen atom.

In most of the channel, the excited states, which are relatively close energetically, may be expected to relax fast enough for reactive balance to be assumed. This dynamic equilibrium of the excited states holds, regardless of what the plasma is doing if the excited state time scales are short enough. Given the excited state population distribution, and assuming that the ground state population is essentially the neutral density, then overall rate coefficients may be calculated. Presented here are overall recombination coefficients. The overall collisional ionization coefficient may be calculated by imposing overall microreversibility [8].

2.1   Argon Atom (AI)

The argon atom model consists of 21 levels, including the ground state, 19 lumped excited states, and the continuum (the ion). The results using the Drawin cross-section model [4] have been curve-fitted to arrive

at an overall recombination coefficient (useful up to $T_e = 50000K$):

$$S_{ca} = 8.25 \times 10^{-43} \exp\left(\frac{(\ln(\frac{T_e}{1000}) - 3.95)^2}{0.6144}\right) \frac{m^6}{s} \quad (1)$$

This compares favorably with the results reported by Owano, et al [6], which adjusted calculated overall rate coefficients (based on experimentally derived cross-sections) with spectroscopically measured rates in argon, and arrived at the following overall three-body electron-ion recombination coefficient:

$$S_{ca}^{Owano} = 3.3 \times 10^{-44}\left(\frac{135300}{T_e} + 2\right)\exp\left(\frac{47800}{T_e}\right)\frac{m^6}{s} \quad (2)$$

S_{ca}	$T_e(K)$		
	10000	20000	40000
this work	6.84×10^{-41}	3.63×10^{-42}	9.22×10^{-43}
Owano	6.10×10^{-41}	3.15×10^{-42}	5.87×10^{-43}

Table 1: Collisional rate coefficients for three-body recombination in the argon atom (AI): comparison of the results of this work and those of Owano. Units of S_{ca} are m^6/s.

2.2   Argon Ion (AII)

A 33-level second ionization model for argon was also developed. Note that the gap between the highest excited state used and the ion is 2.77 eV. This is a weakness at low T_e (as the low temperature behavior depends on the missing upper levels) and will have to be accounted for.

$$S_{cc} = 7.17 \times 10^{-40} \exp\left(-\frac{(\ln(\frac{T_e}{1000}) - 1.3485)^2}{0.9293}\right)\frac{m^6}{s} \quad (3)$$

2.3   Hydrogen Atom (H)

The hydrogen atom has been modeled with 19 levels. The resulting collisional recombination rate coefficient is (good up to $T_e = 60000K$):

$$S_{ca} = 6.985 \times 10^{-42} \exp\left(\frac{(\ln(\frac{T_e}{1000}) - 4.0883)^2}{0.8179}\right)\frac{m^6}{s} \quad (4)$$

3 Inlet Flow Model

The rest of this paper will investigate steady-state ionization at the inlet, or ignition, of a self-field magnetoplasmadynamic thruster. This section will present the basic equations of motion as well as details of the models used here for ion slip and electrical conductivity. Section 4 will consider three cases of constant speed ignition, and section 5 will consider ignition in an accelerating flow.

We will consider injection of atomic argon into the thruster channel through a porous backplate to ensure 1-D bulk flow. Figure 1 shows the general configuration of the inlet region. Since the hypothesis of this work is that back-diffusion of electron-ion pairs sustains ignition, the characteristic scale length of the ionization region is expected to be the back diffusion length, l_D, defined below.
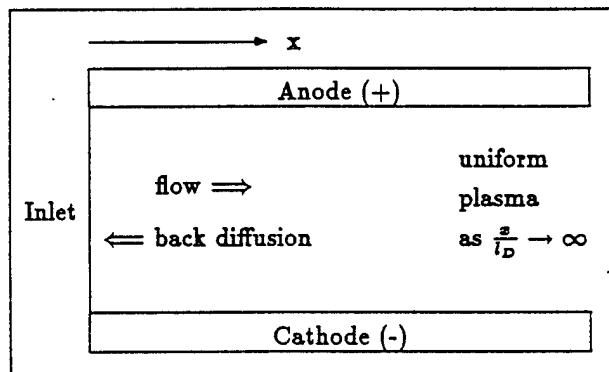

Figure 1: 1-D Thruster Inlet Region

3.1 Equations of Motion

The steady state, quasi-one dimensional equations of motion for this configuration are overall and electron continuity, overall momentum, electron energy, and a magnetic field equation. The equations used are a simplified version of the 1-D equations of Niewood [5].

The overall continuity equation is,

$$(n_e + n_a)u = n_g u = G = \frac{\dot{m}}{Am_i} \quad (5)$$

where n_g is the total number density of of nuclei, n_a is the number density of atoms, and n_e is the number density of electrons. The mass flow rate is $\dot{m}$, the channel area is A, and the nucleus mass is m_i. Since this is a quasi-neutral plasma, and only singly ionized specie may exist, $n_e = n_i$, where n_i is the number density of the ions. The ion continuity equation is

$$\frac{dn_e u}{dx} = -\frac{dn_e V_i}{dx} - \frac{D_a n_e}{h^2} + \dot{n}_e \quad (6)$$

In equation 6, the transverse ambipolar diffusion, $\frac{D_a n_e}{h^2}$, is included (with an assumed parabolic distribu-

tion of n_e in the transverse direction so that h is actually $\frac{1}{\sqrt{12}}$ of the actual channel height, $H \approx 0.02m$.) in order to allow a balance to be struck far downstream of the ionization layer.

The integrated total momentum equation, including pressure and magnetic (Lorenz) forces and neglecting friction, is

$$m_i n_g u^2 + p + \frac{B_z^2}{2\mu_o} = F \quad (7)$$

and the electron energy equation, including axial heat conduction, Ohmic heating, and energy loss due to the endothermic ionization process, and neglecting both pressure work and transverse heat conduction, is

$$\frac{3}{2} k_B \frac{dn_g u \alpha T_e}{dx} = -\frac{d}{dx}\left(K_e \frac{dT_e}{dx}\right) + \frac{j^2}{\sigma} - E_{ai} \dot{n}_e \quad (8)$$

and the magnetic field is governed by the following equation

$$\frac{dB}{dx} = -\mu_o j = -\mu_o \sigma[E - uB] \quad (9)$$

where n_e is the electron (and ion) number density and n_n is the neutral particle number density, u is the bulk speed, p is the pressure, B is the magnetic field, T_e is the electron temperature, E and j are the electric field and current density, and G and F are constants of the flow. $V_j = u_j - u$ is the species j slip speed, and u_j is the speed of species j. The ionization fraction is defined as $\alpha \equiv n_e/n_g$.

3.2 Ion-Neutral Slip

Since ions are being directly accelerated while neutrals are accelerated by collisions with ions, there are actually two effects (acceleration and density gradients) leading to ion-neutral slip. In [9] we derived an alternative to Fick's Law from the neutral momentum equation. Using the definition of the ambipolar diffusion coefficient:

$$D_a = \frac{k_B(T_e + T_g)}{m_i \bar{c}_{in} Q_{in} n_g}\left(\frac{m^2}{s}\right) \quad (10)$$

as well as the definition of the Bohm velocity:

$$v_B = \sqrt{\frac{k_B(T_e + T_g)}{m_i}} \quad (11)$$

and the temperature ratio

$$\theta \equiv \frac{T_g}{T_e + T_g} \quad (12)$$

(θ should be small near the inlet, and we use $\theta = 0.1$ here) we arrive at the following expression (from the neutral momentum equation) for the ion slip flux:

3

$$n_e V_i = D_a n_g \theta \left((1-\alpha) \left(\frac{u^2}{\theta v_B^2} - 1 \right) \frac{1}{u} \frac{du}{dx} - \frac{d\alpha}{dx} \right)$$

$$(13)$$

If there is no acceleration and no total pressure gradient ($\theta \frac{dn_a}{dx} = -\frac{dn_e}{dx}$), Fick's law results:

$$(n_e V_i)_F = -D_a \frac{dn_e}{dx} = -D_a n_g \frac{d\alpha}{dx} \qquad (14)$$

The ambipolar diffusion coefficient can be replaced by $C_a = D_a n_g$, a function of temperature only. Using the form for D_a in equation 10, C_a is, for argon

$$C_a = 1.274 * 10^{19} \left(1 + \frac{T_e}{T_g} \right) \sqrt{T_g} (m^{-1} s^{-1})$$

3.3 Electrical Conductivity

The electrical conductivity which appears in equations 8 and 9 is significant for both the Ohmic heating and the rate of change of the magnetic field, and is, in general, a function of both electron temperature and ionization fraction. This behavior is seen at low α, and may be expressed as [1]:

$$\sigma = \frac{e^2 n_e}{m_e (\nu_{ei} + \nu_{en})}$$

where the electron-ion collisional rate goes as the electron temperature to the $-3/2$ power:

$$\nu_{ei} \propto T_e^{-3/2} \ln \left(1.24 \times 10^7 \sqrt{\frac{T_e^3}{n_e}} \right)$$

using mks units, and temperatures in K, and the electron-neutral collisional rate goes as the square root of the electron temperature [1]:

$$\nu_{en} \propto T_e^{1/2}$$

Assuming that $\ln \left(1.24 \times 10^7 \sqrt{\frac{T_e^3}{n_e}} \right) \approx 10$, and using numerical values for argon from Bittencourt [1], then the electrical conductivity, nondimensionalized by a reference value, is

$$\frac{\sigma}{\sigma_{ref}} = \frac{\alpha \tau^{3/2}}{\alpha + (1-\alpha)q\tau^{1/2}} = \frac{\tau^{3/2}}{1 + (\frac{1}{\alpha} - 1)q\tau^{1/2}} \quad (15)$$

where $\tau = T_e/T_{ref}$ and T_{ref} is the electron temperature as $x/l_D \to \infty$, and

$$q = 7.2 \times 10^{-12} T_{ref}^2$$

$$\sigma_{ref} = 7.76 \times 10^{-4} T_{ref}^{\frac{3}{2}} \quad Si$$

q is roughly the minimum ionization fraction for Coulomb collision dominance at the reference temperature. $q \approx 0.001$ results from typical channel conditions. The reference conductivity is approximately 1000 to 4000 Si.

4 Constant Speed Ignition

In this case, we extend the work in [9], adding the effects of temperature variation to a constant speed ionizational ignition analysis in a constant area channel. The total number of nuclei (which is a constant for constant speed) in the plasma is governed by equation 5, with G constant.

Using Fick's law in this case, equation 14, then the definition of the ion slip, Γ is:

$$\frac{d\alpha}{dx} = -\frac{n_e V_i}{C_a} \equiv \frac{\Gamma}{C_a} \qquad (16)$$

Taking advantage of the constant G, the convection term in equation 6 becomes $G\frac{d\alpha}{dx} = G\Gamma/C_a$, by equation 16, so that the ion continuity equation is now

$$\frac{d\Gamma}{dx} = \frac{G\Gamma}{C_a} - \left(\dot{n}_e - \frac{D_a n_e}{h^2} \right) \qquad (17)$$

Equation 8, the energy equation, is modified by the assumption that $j \approx \sigma E$, and defining the heat flux as

$$q \equiv K_e \frac{dT_e}{dx} \qquad (18)$$

so that the resulting energy equation is

$$\frac{3}{2} Gk_B \frac{d\alpha T_e}{dx} = -\frac{dq}{dx} + \sigma E^2 - E_{ai}\dot{n}_e \qquad (19)$$

The nondimensional forms of equations 16, 17, 18, and 19 are, respectively:

$$\frac{d\alpha}{d\xi} = \gamma \qquad (20)$$

$$\frac{d\gamma}{d\xi} = \gamma - \alpha \Lambda_1 [\bar{S}(1-\alpha) - \alpha^2 \Lambda_2 - \Lambda_3] \qquad (21)$$

$$\frac{d\tau}{d\xi} = Q \qquad (22)$$

$$\frac{dQ}{d\xi} = \frac{1}{Le} [\alpha Q + \tau\gamma - \bar{\sigma}\Pi + \Theta_{ai}\alpha\Lambda_1 [\bar{S}(1-\alpha) - \alpha^2 \Lambda_2]]$$

$$(23)$$

where the length is nondimensionalized as $\xi = x/l_D$, where $l_D = C_a/G$ is the back-diffusion length, the nondimensional slip is $\gamma = \Gamma/G$, and the electrical conductivity is $\bar{\sigma} = \sigma/\sigma_{ref}$. The nondimensional parameters are:

4

$$\beta = \frac{v_B^2}{u_{ref}^2} \qquad \Lambda_1 = \frac{C_a S_{ai}}{u^2}$$

$$\Lambda_2 = n_g \left(\frac{n_a}{n_e^2}\right)^* \qquad \Lambda_3 = \frac{C_a}{S_{ai}(hn_g)^2}$$

$$\Pi = \frac{C_a \sigma_{ref} E^2}{\frac{3}{2} k_B T_{ref} G^2} \qquad \Theta_{ai} = \frac{E_{ai}}{\frac{3}{2} k_B T_{ref}}$$

The Damkohler coefficient for ionization ($\Lambda_1 = l_D/l_{ai}$), The nondimensional ionization coefficient is $\bar{S}(\tau) = S_{ai}/S_{ai}^{ref}$, and S_{ai}^{ref} is evaluated at T_{ref}, the electron temperature at $\xi = \infty$. The Lewis number, which is the ratio of the diffusion length scale to the thermal conductivity length scale and is typically $O(10^{-2})$, is

$$Le = \frac{3}{2}\frac{k_B n_g D_a}{K_e} = \frac{l_D}{l_{cond}}$$

4.1 Atomic Injection, Constant T_e

The case of constant speed and temperature, and atomic injection was treated previously by these authors [9], and is repeated briefly here since its results introduce some points relevant to the other cases. Setting $Q \equiv 0$, leaves only two equations, for α and γ (equations 20 and 21). Using the ionization fraction as the independent variable (dividing equation 21 by equation 20, the result is

$$\frac{d\gamma}{d\alpha} = 1 - \frac{\Lambda_1 \alpha[(1-\alpha) - \alpha^2 \Lambda_2 - \Lambda_3]}{\gamma} \qquad (24)$$

The first boundary condition chosen is critical: that the ions (moving at a velocity equal to the average velocity plus the ion slip velocity) reach the sheath at the inlet wall at the Bohm velocity *moving upstream against the bulk flow*:

$$n_e(u + V_i) = -n_e v_B$$

Using the nondimensional variables, this becomes

$$\gamma_o = \alpha_o \left(1 + \frac{v_B}{u}\right) \qquad (25)$$

The second boundary condition is that the derivative be smooth as $\gamma \to 0$, so that the numerator of the fraction in equation 24 is zero at $\xi = \infty$:

$$1 - \alpha_\infty - \alpha_\infty^2 \Lambda_2 - \Lambda_3 = 0 \qquad (26)$$

so that the ionization fraction at ∞ is

$$\alpha_\infty = \frac{1}{2\Lambda_2}\left[\sqrt{1 + \Lambda_2(1-\Lambda_3)} - 1\right] \qquad (27)$$

The ignition criterion is found by a local analysis of equation 24 near $\alpha = \gamma = 0$. Successful ignition is
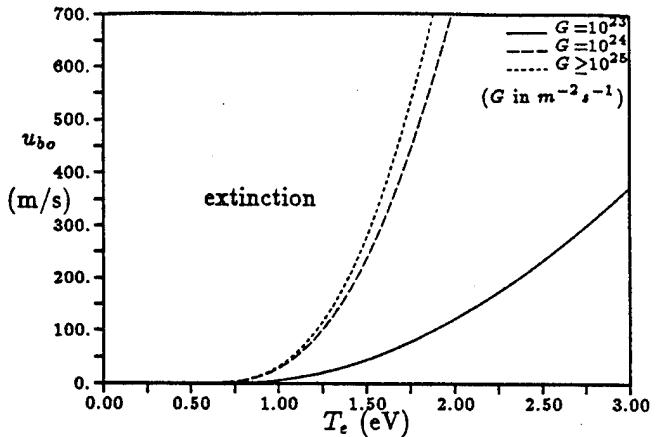

Figure 2: Blowoff speed for argon, in $\frac{m}{s}$, constant speed and temperature, atomic injection.

defined as as a solution where the wall condition may be satisfied at $\gamma_o > 0$ for a finite ionization zone [7], requiring

$$\Lambda_1(1 - \Lambda_3) > \frac{1}{4} \qquad (28)$$

which sets a lower limit on the Damkohler coefficient, or an upper limit on the injection speed. This upper limit speed can be considered a "blowoff" speed:

$$u < 2\sqrt{\frac{C_a S_{ai}}{1 + \frac{4C^2}{(Gh)^2}}} = u_{bo} \qquad (29)$$

This blowoff speed is plotted vs T_e in figure 2 for various G and $H = 0.02m$. In this case, we use the argon ionization coefficient described earlier in this paper which differs from figure 1 of reference [9], which has a blowoff speed using the Hinnov-Hirschberg ionization coefficient.

Therefore, successful ignition in this simple model sets an upper bound on the injection speed, as is found in simple 1-D diffusion flames. Note also that G appears in the product $\Lambda_1 \Lambda_3$ in equation 28, so that, under certain conditions, where the ∞ boundary condition is accepted, there is also a constraint of mass flow rate, $\dot{m} = m_i GA$. It should be noted that in the cases displayed above, the blowoff speed is less than the acoustic speed of the heavy particles.

4.2 Atomic Injection, Varying T_e

In this section we now allow T_e to vary (finite thermal conductivity) to investigate the effects on the ignition criterion. Using α as the independent variable again, the equations for constant speed, finite thermal conductivity, and atomic injection are equations 21, 22, and 23, respectively, all divided by equation 20:

$$\frac{d\gamma}{d\alpha} = 1 - \frac{\Lambda_1\alpha[\bar{S}(1-\alpha) - \alpha^2\Lambda_2 - \Lambda_3]}{\gamma} \qquad (30)$$

$$\frac{d\tau}{d\alpha} = \frac{Q}{\gamma} \qquad (31)$$

$$\frac{dQ}{d\alpha} = \frac{1}{Le}\left[\tau + \frac{\alpha Q - \bar{\sigma}\Pi + \Theta_{ai}\alpha\Lambda_1[\bar{S}(1-\alpha) - \alpha^2\Lambda_2]}{\gamma}\right] \qquad (32)$$

The boundary conditions are again the wall condition, equation 25, plus that all derivatives are smooth at the asymptotic limit: $\gamma_\infty \to 0$. One such condition will be the same as equation 26. In addition, $Q_\infty = 0$, and

$$\bar{\sigma}\Pi - \Theta_{ai}\alpha\Lambda_1[1 - \alpha_\infty - \alpha_\infty^2\Lambda_2] = 0 \qquad (33)$$

Finally, it is assumed that the electrons do not heat the inlet wall, so that the initial electron heat flux is zero: $Q_o = 0$.

Note that $\bar{S} = \bar{\sigma} \equiv 1$ at $\xi = \infty$, since that is where the reference values are taken. The combination of equations 26 and 33 is usually used to solve for α_∞ and $T_{e\infty} = T_{ref}$ as a function of (n_g, h, T_g, E). In this case, the specified values are (G, T_{ref}, u, h) (u is arbitrary since no momentum balance is used), so that $(\alpha_\infty, E) = f(n_g(u, G), h, T_g, T_{ref})$, and

$$\Pi = \Theta_{ai}\Lambda_1\Lambda_3\alpha_\infty \qquad E = \sqrt{\frac{E_{ai}C_a\alpha_\infty}{\sigma_{ref}h^2}}$$

Local analysis near $\alpha = \gamma = 0$ results in the a similar ignition criterion as in the constant T_e case, except it is evaluated at the inlet temperature:

$$u < 2\sqrt{\frac{C_a S_{ai}(0)}{1 + \frac{4C^2}{(Gh)^2}}} = u_{bo} \qquad (34)$$

Figure 3 shows the temperature and ionization profiles for the trajectory corresponding to $Le = 0.037$, $\Lambda_1 = 0.285$, $\Pi = 0.56$. The corresponding dimensional quantities are denoted on the graph.

It appears that the temperature variation does not have a dramatic qualitative effect on ignition. However, it will have a quantitative effect, particularly at temperatures below $10000K$, where the ionization rate coefficients are very sensitive to temperature changes. Another way that the temperature effect may be greater would be when the Hall effect plays a role in the thermal conductivity, raising the inlet temperature even higher, while shrinking the zone where temperature variations are significant. Burton [2] considered this effect. Note also that T_e at the wall is always greater than T_e at ∞, so that the blowoff speed
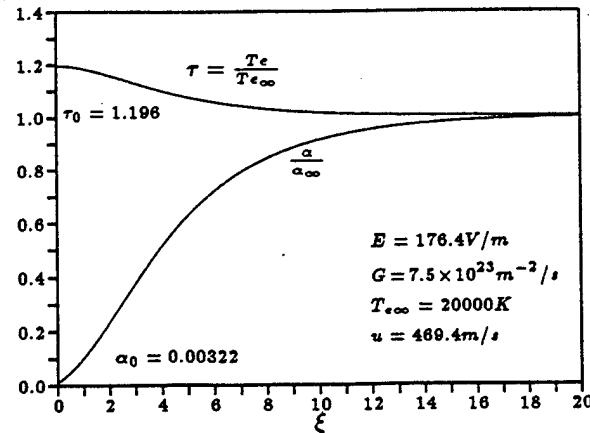

Figure 3: Constant speed ignition with atomic injection and varying temperature: α and T_e.

in this case will always be higher than that for the constant temperature case.

5 Ignition in Accelerating Flows

We now drop the assumption of constant speed, with $Q \equiv 0$. This allows us to analyze the interaction between the behavior of the magnetic field and the ionization process. The problem is treated as two inner-outer problems. First, there is a magnetic inner (diffusive) region from the wall out to a zero current boundary condition, and then an ideal outer region which is solved analytically into the channel and to the throat. The ionization zone is found to be entirely embedded in the magnetic diffusion layer, and consists of an inner layer, near the wall, where ambipolar diffusion is significant, and an outer layer, where diffusion plays no significant role. The first subsection following describes the model, and the second presents results.

5.1 Formulation

We start with $G = \frac{\dot{m}}{m_i A_i} = $ constant in the ionization zone. The differential form of the momentum equation (7) is used:

$$m_i G\frac{du}{dx} = \frac{d}{dx}\left[p + \frac{B^2}{2\mu_o}\right] \qquad (35)$$

where the pressure for a two temperature, electrically neutral plasma is

$$p = m_i n_g v_B^2(\alpha + (1-\alpha)\theta) \qquad (36)$$

Here, because of the acceleration, the alternative version for the ion slip flux is used, so that, from equation 13, we can define the flux, $\Gamma = -n_e V_i$, from

$$\frac{d\alpha}{dx} = \frac{\Gamma}{C_a\theta} + (1-\alpha)\left(\frac{u^2}{\theta v_B^2} - 1\right)\frac{1}{u}\frac{du}{dx} \qquad (37)$$

6

This equation, along with the following three, constitute the equations of motion for the quasi-one-dimensional isothermal flow problem. Starting with equation 35, and using equations 36, 37, the momentum equation becomes [9]

$$\frac{du}{dx} = \frac{-\frac{v_E^2(1-\theta)\Gamma}{C_a u} + \frac{\theta B}{m_i G}\sigma(E - uB)}{1 - \alpha(1-\theta) - \frac{\theta v_E^2}{u^2}} \quad (38)$$

Equation 6 may be rewritten as:

$$\frac{d\Gamma}{dx} = G\frac{d\alpha}{dx} + \frac{C_a \alpha}{h^2} - S_{ai} n_g^2 \alpha(1-\alpha) \quad (39)$$

and the final equation is the magnetic field equation, equation 9.

Nondimensionalizing these equations will allow us to analyze them parametrically. Defining reference values $u_{ref} = \frac{B_o^2}{2\mu_o m_i G}$, and $l_{ref} = \Lambda_m = \frac{1}{\mu_o \sigma u_{ref}}$, then the new variables are $\bar{u} = \frac{u}{u_{ref}}$, $\gamma = \frac{\Gamma}{G}$, $b = \frac{B}{B_o}$, $\bar{E} = E/(u_{ref} b_o)$ and $\xi = \frac{x}{\Lambda_m}$. The resulting nondimensional equations of motion are:

$$\frac{d\bar{u}}{d\xi} = \frac{-\frac{\beta(1-\theta)\gamma}{\epsilon_D \bar{u}} + \frac{2\theta b}{f}}{1 - \alpha(1-\theta) - \frac{\theta\beta}{\bar{u}^2}} \quad (40)$$

$$\frac{d\alpha}{d\xi} = \frac{\gamma}{\epsilon_D \theta} + (1-\alpha)(\frac{\bar{u}^2}{\theta\beta} - 1)\frac{1}{\bar{u}}\frac{d\bar{u}}{d\xi} \quad (41)$$

$$\frac{d\gamma}{d\xi} = \frac{d\alpha}{d\xi} + \alpha\left(\epsilon_w - \frac{\lambda(1-\alpha)}{\bar{u}^2}\right) \quad (42)$$

$$\frac{db}{d\xi} = -\frac{\bar{E} - \bar{u}b}{1 + (\frac{1}{\alpha} - 1)q} \quad (43)$$

where for convenience we define

$$f = \frac{1 + (\frac{1}{\alpha} - 1)q}{\bar{E} - \bar{u}b} = -\left(\frac{db}{d\xi}\right)^{-1}$$

In addition to the parameters defined previously,

$$\epsilon_D = \frac{(C_a)\mu_o \sigma_{ref} u_{ref}}{G} \approx \frac{(l_d)_\parallel}{\Lambda_m}$$

$$\lambda = \frac{S_{ai} G}{u_{ref}^2 \mu_o \sigma_{ref}} \approx \frac{\Lambda_m}{L_{ai}}$$

$$\epsilon_w = \frac{C_a \Lambda_m}{G h^2}$$

The first far downstream ($\xi \to \infty$) boundary condition will be that $\bar{E} = \bar{u}b$, which implies an infinite length and hence an infinite magnetic Reynolds number. This motivates us to choose the magnetic field itself as the independent variable. Dividing the three

other equations of motion (40, 41, 42) by equation 43, we arrive at the following set of equations:

$$\frac{d\bar{u}}{db} = \frac{f\beta(1-\theta)\frac{\gamma}{\epsilon_D \bar{u}} - 2\theta b}{1 - \alpha(1-\theta) - \frac{\theta\beta}{\bar{u}^2}} \quad (44)$$

$$\frac{d\alpha}{db} = -f\frac{\gamma}{\epsilon_D \theta} + (1-\alpha)\left(\frac{\bar{u}^2}{\theta\beta} - 1\right)\frac{1}{\bar{u}}\frac{d\bar{u}}{db} \quad (45)$$

$$\frac{d\gamma}{db} = \frac{d\alpha}{db} - f\alpha\left(\epsilon_w - \frac{\lambda(1-\alpha)}{\bar{u}^2}\right) \quad (46)$$

The second downstream (∞) boundary condition is the same balance between transverse ambipolar diffusion and ionization used in the constant speed case, which is now:

$$1 - \alpha_\infty = \frac{C_a u_\infty^2}{S_{ion} G^2 h^2} = \frac{\epsilon_w \bar{u}_\infty^2}{\lambda} \quad (47)$$

Additional boundary conditions are the conditions at the injector wall, and the internal boundary conditions at the sonic passage point. The injector wall condition (25) still holds, except in the nondimensional form it is now

$$\gamma_o = \alpha_o\left(1 + \frac{\sqrt{\beta}}{\bar{u}_o}\right) \quad (48)$$

where the speed at the inlet wall, $\bar{u}_o$, is now a result of the calculation, rather than a freely chosen value, as was the case in the constant speed problem.

If subsonic injection is assumed, then smooth passage through a "sonic point" [3] is required in the steady state. The sonic point is characterized as a singularity that occurs when the denominator of $\frac{d\bar{u}}{db}$ (equation 44) is identically zero at some $b = b_s$. In order to be physically possible, the numerator must be zero at the same b_s. This poses a difficulty in the full set of equations, since trajectories diverge rapidly near this singularity.

Therefore an "outer" set of equations is used "far" from the wall - and the sonic point is found to be embedded in this outer layer. Since $\epsilon_D \ll 1$, diffusion is dropped ($\frac{d\gamma}{db} \approx 0$) and the combination γ/ϵ_D is eliminated from equations 44 and 45, arriving at the nondiffusive layer equations:

$$\frac{d\bar{u}}{db} = \frac{\beta(1-\theta)\frac{f\alpha}{\bar{u}}\left(\frac{\lambda(1-\alpha)}{\bar{u}^2} - \epsilon_w\right) - 2b}{1 - \frac{\theta\beta}{\bar{u}^2}\left(1 + \frac{\alpha(1-\theta)}{\theta}\right)} \quad (49)$$

$$\frac{d\alpha}{db} = -f\alpha\left(\frac{\lambda(1-\alpha)}{\bar{u}^2} - \epsilon_w\right) \quad (50)$$

and the ion slip flux is, from post-processing:

7

$$\frac{\gamma}{\epsilon_D} = -\frac{\theta}{f}\left[\frac{d\alpha}{db} - (1-\alpha)\left(\frac{\bar{u}^2}{\theta\beta} - 1\right)\frac{1}{\bar{u}}\frac{d\bar{u}}{db}\right] \quad (51)$$

The variables at sonic point (where the denominator of equation 49 is zero) may all be found explicitly by setting both the numerator and denominator of equation 49 equal to zero, and using the integrated momentum equation (eqn. 7, evaluating the constant, F once $\bar{E}$ and b_∞ are chosen) to solve for b_s, α_s, and u_s. These non-diffusive equations are used to march back toward the wall from the sonic point (and also from the sonic point out to ∞ for the magnetic diffusive layer) until the slip γ becomes positive, and then patched with the diffusive solution, equations 44 to 46, are to get to the wall itself. The diffusive set is required to meet the boundary condition on the slip.

At this point, we have solved the problem from the wall ($b = 1$) to the end of the magnetic diffusion layer (where $\bar{E} = \bar{u}_\infty b_\infty$). This process yields a family of $b_\infty(\bar{E})$ for each $\bar{E}$, each of which satisfies the boundary conditions. Thus, there is one remaining degree of freedom. The problem is closed via an idealized channel downstream (the "outer" magnetic problem), where the flow is assumed to be constant temperature, frozen (at $\alpha = \alpha_\infty$), and zero current ($\bar{E} = \bar{u}b$). The magnetic field is then a function of the area of the channel, and we look for the throat. [3] Now (switching to dimensional variables), $\phi = EH$ is a constant, so that the speed and density ($m_i n_g = \dot{m}/(uA)$) are

$$u = \frac{\phi}{BH} \qquad m_i n_g = \frac{B}{\phi}\frac{\dot{m}}{w}$$

and the pressure, from equation 36 is

$$p = \frac{B}{\phi}\frac{\dot{m}}{w}v_B^2(\theta + \alpha_\infty(1-\theta))$$

so that the momentum equation, becomes

$$d\frac{u^2}{2} + \frac{1}{m_i n_g}\left(dp + d\frac{B^2}{2\mu_o}\right) = 0 \quad (52)$$

Using the expressions for u, $m_i n_g$, and p above, and the nondimensional variables and parameters already defined, plus the nondimensional potential,

$$\bar{\phi} = \frac{\phi}{E_{ref}H_t}$$

then equation 52 may be recast and integrated to obtain the following expression:

$$\frac{H_o}{H} = b\sqrt{\frac{1}{b_\infty^2} + \frac{2\beta(\theta + \alpha_\infty(1-\theta))\ln(\frac{b_\infty}{b})}{\bar{\phi}^2} + \frac{4(b_\infty - b)}{\bar{\phi}}}$$

$$(53)$$

We then find the throat, given b_∞ and $\bar{E}$, by evaluating this expression for decreasing b until H_o/H is minimized. In practice, the contraction ratio, H_o/H_t is taken as a given, and equation 53 gives another relationship between $\bar{E}$ and b_∞.

This closes the problem for a given set of the parameters. The numerical integrations are solved using a Runge-Kutta space-marching scheme, starting at the sonic point (non-diffusive equations), and marching out both towards b_∞ and b_o. The diffusive (equations 44, 45, and 46) and non-diffusive (equations 49 and 50) solutions are patched just after the outer, non-diffusive set value for γ is small and positive (> 0.001), and then the diffusive inner set is integrated to the wall.

5.2 Results

Following are results from the inner-outer approach to the accelerating ignition problem as described above. The plots vs ξ have been truncated so as to show the ionization layer more clearly. A "standard" set of parameters is defined in this work corresponding to roughly $T_e \approx 20000K$, $H = 0.02m$, $G \approx 7.5 \times 10^{24}\ m^{-2}/s$: $\lambda = 2$, $\epsilon_D = 0.005$, $\Lambda_3 = 0.1$, $\beta = 0.05$, $\theta = 0.10$, and $q = 0.001$. Since the ionization rate coefficient varies the most dramatically with temperature of the parameters, as can be seen in figure 4, λ will be varied while the other parameters are fixed.
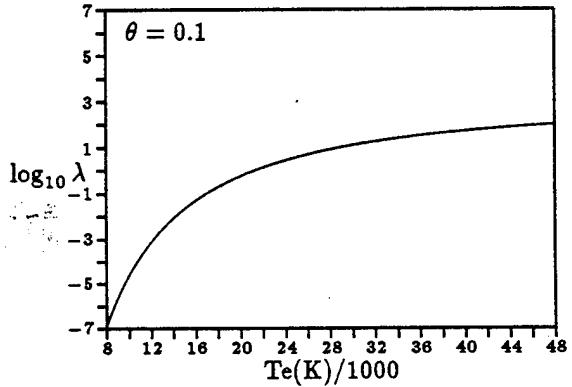

Figure 4: The parameter λ vs. T_e.

Figure 5 shows γ vs α, for the standard set of parameters, and a contraction ratio of one ($\bar{E} = 0.6019$, $b_\infty = 0.6583$). The diffusive and non-diffusive solutions are patched at $\gamma = 0.0036$, $\alpha = 0.5592$, and the sonic point is at $b = 0.9854$, $\alpha_s = 0.9029$. The isoclines are for the diffusive inner set at $b = 1$, using equation 7 to solve for $u(\alpha)$. Note that, although the inner equations diverge as $\gamma \rightarrow 0$ (as can be seen from the isoclines), the outer set passes through smoothly, and the two sets patch quite well at a small positive γ, as can also be seen from the isoclines.

Figure 6 shows the ionization fraction, α, vs the nondimensional length, $\xi = x/\Lambda_m$, for the "standard"